Modeling the Pathogenesis of Drug-Induced Liver Injury with Organoids and Microfluidic Devices

by

Charles Jian Zhang

A dissertation submitted in partial fulfillment
of the requirements for the degree of
Doctor of Philosophy
(Medicinal Chemistry)
in The University of Michigan
2023

Doctoral Committee:

Assistant Professor Jonathan Z. Sexton, Chair
Associate Professor Amanda Garner
Assistant Professor Matthew O'Meara
Professor Jason R. Spence

Charles Jian Zhang

zhangcj@med.umich.edu

ORCID iD: 0000-0003-0300-849X

Dedication

This dissertation is in dedication to my parents Annie and William for their love and support. It is also dedicated in memory of Andrew Melville (“Mr. M”), my high school biology teacher, who made me curious about the world and inspired the many qualities of who I am today.

Acknowledgements

I would like to first thank the history of great scientists that laid the groundwork for me to conduct the research in this dissertation. Others provided the foundational discoveries and techniques for me to simply combine into my research. I want to also particularly thank the previous scientists that focused efforts on breaking barriers or empowering others on top of the daunting task of a career in research. It is these efforts made by the scientific community that provided me and many others with the path to success.

I would also like to thank members of the University of Michigan College of Pharmacy Medicinal Chemistry department for supplying all of us students with an unmatched research environment. Particularly, Drs. George Garcia and Heather Carlson for leading our department through difficult times, Dr. Amanda Garner for your student outreach and for serving as a committee member, and Antoinette Hopper and Sarah Lloyd for managing our day-to-day affairs.

Dr. Robert Fontana, thank you for providing your decades of expertise in liver diseases to help craft the scientific direction presented in this thesis. Thank you also for always pushing for my personal career development on top of our research.

Dr. Jason Spence thank you for welcoming me into your lab to learn your techniques, throwing symposium opportunities my way, and getting me in touch with the right people. To that point, I would also like to thank your lab members Charlie Childs and Meghan Capeling for training me, gassing me up, and being my friends. Drs. Tristan Frum and Daysha Ferrer-Torres

thank you for showing me the type of next-level researchers we produce at University of Michigan, willing to collaborate with a trainee like me, and giving advice during conflicts and hard times. Most importantly, I would like to thank Sha Huang for spending countless hours training me and always going out of her way to help me and other trainees succeed.

Dr. Matthew O'Meara, you are one of the sweetest people I have ever met in my life let alone in science. You have always been there willing to support me and anyone that approaches you. You and Dr. Teresa O'Meara showed me how life changing being available and kind can be to others, and it is a quality I hope to bring forward in my career. I wish you two and Robin a beautiful future.

In my lab I would like to first thank Dr. Jonathan Sexton for being my mentor, introducing me to modern techniques in science, coming up with impactful ideas to study, and showing me how to make what most would consider impossible possible. I cannot imagine myself even knowing about the type of research we do let alone having achieved this dissertation without your consistent support. I can see many great things yet to come from the Sexton lab (NTBFW) and owe the rest of my career to your guidance.

From my lab, I would like to thank Tracey Schultz for her help managing us trainees and laying the foundation for us to do good science. Dr. Jesse Wotring and soon-to-be Dr. Sean McCarty, we met on day 1 here at College of Pharmacy orientation and have been together providing support to each other until the end. Thank you two for being my first friends here. Khadija Shafiq thank you for always brightening up the mood in lab and raising the volume, but more importantly always available and eager to lend a hand ("*Instrumentum Disciplinae*!"). Sophia Meyer, thank you for being a wonderful trainee, being all-around impressive, knowledgeable, and professional when needed and for restoring my faith that good scientists

exist the many *many* times I've lost it. Benjamin Halligan, thank you for being an endless knowledge bank and putting up with my neediness over the years. I will miss our walks to the hospital cafeteria. Thank you, Dr. Megan Procario, for lending your strong expertise and smile to enhance and brighten our lab but also for very quickly being a great friend. Max Garcia, thank you for being fun and kind and showing me how multitalented and ingenious the next generation of scientists can be.

Next, I would like to thank the members of my family. First to get it out of the way thank you Uni for being a caring, loving, consoling, funny, sweet, and noisy little Schnauzer. I never could have imagined how life changing you would be for me. I would like to thank my sister Angelina for brightening our family. I hope someday you'll know how you completed our family. I would say I'm doing this to be a good example for you, but I already see from your personality that you don't need anyone to inspire or guide you. You will achieve everything on your own. Thank you, mom, for always putting me first in your life, especially when it was just the two of us. I got to live the best life I could because of your hard work and perseverance. You inspire me to be strong and to always stand up for myself. Thank you, dad, for being the hardest working one to support mom, Angie, and me. We would not live the lives we have now if not for you. I love all of you.

Dr. Jinghan Liu, my fiancé, thanks for going through this journey along with me. When I think back to this, I will only remember the pleasant time we shared and memories we made here. I can say this was a good time of my life because you were with me. I love your beauty, your intelligence, your understanding, your kindness, your humor, your composure, your companionship, and your love for me. I love you and I hope I can be the husband you deserve.

Table of Contents

List of Figures

List of Tables

List of Appendices

Abstract

Drug-induced liver injury (DILI) is a critical concern in modern medicine, encompassing a broad spectrum of liver-related abnormalities caused by various pharmaceutical compounds. DILI is classified as either intrinsic, occurring in a dose-dependent and predictable manner, or idiosyncratic, occurring seemingly spontaneously. Ranging from mild liver enzyme elevations to acute liver failure, DILI is an unpredictable and multifaceted problem that poses significant risks and challenges in both drug discovery and patient experiences.

DILI is currently a leading cause of both clinical trial failures and withdrawals post-FDA approval. This is due to a lack of human models that robustly predict hepatotoxicity. Although the current standard, primary human hepatocytes assays are costly, subject to batch variations, and quickly lose hepatocyte function. Drug responses in animal models are not predictive for humans. This results in clinical trial failures where patients suffer severe hepatotoxicity. Even post-approval, market withdrawals and black box warnings for drug safety are often caused by idiosyncratic DILI, where a hepatotoxicity event may only occur in 1:10,000 or less patients given the prescription drug and therefore not adequately sampled through the course of an entire clinical trial.

There have been a multitude of advancements in human-derived liver models in recent years mostly in terms of 3D spheroid/organoid culture. These have been developed either from culturing a mixture of cell types in a confined space to force cell contact or differentiated from induced-pluripotent stem cells (iPSCs). For this dissertation, I adapted a previous protocol of

generating iPSC-derived human liver organoids (HLOs) to a high-throughput screening platform and microfluidic chips. The iPSC-liver model was chosen as it potentiates development of a genetically diverse patient-derived biobank or to study rare idiosyncratic DILI. Human liver organoids (HLOs) contain not only the parenchymal hepatocyte-like cells but also non-parenchymal stellate-like, Kupffer-like, and cholangiocyte-like cells.

HLOs dispersed into 384-well plates retained liver function as measured by marker expression, albumin production, and CYP450 activity and showed viability for high-throughput pre-clinical screening for drug safety. Morphological profiling of treated inform on DILI mechanism. Dispersed HLOs transferred onto microfluidic chips with media flow show remarkable improvement for modelling liver with notable increases in albumin expression and CYP activity. These liver chips reliably model DILI based on cytotoxicity and morphological perturbations (lipid accumulation and mitochondrial impairment) at physiologic drug concentrations and captured a recent case of synergistic DILI not discovered until clinical trials. Single-cell transcriptomics of liver chips predicted an additional case of synergistic DILI that was confirmed in a high-throughput assay. A 16-well microfluidic liver chip was also developed to balance throughput and physiological relevance. This platform shared all the improvements seen with the original microfluidic chip but with an added benefit of culture longevity. 16-well liver chips were shown to maintain cell viability for up to 28-days and serve as a long-term liver model.

Finally, we isolated PBMCs from DILI patient whole blood to reprogram into iPSCs. Reprogrammed iPSCs were differentiated into HLOs. 4 patient-derived HLOs were used to screen a panel of 64 hepatotoxins. While neither HLO line responded to all 64 compounds, screening through all 4 lines captured hepatotoxicity of the drug panel with high accuracy,

emphasizing the need for genetic diversity and redundant screening. Future research will attempt to capture the original patient's DILI events through added model complexity and inclusion of other cell types.

Chapter 1 : Introduction

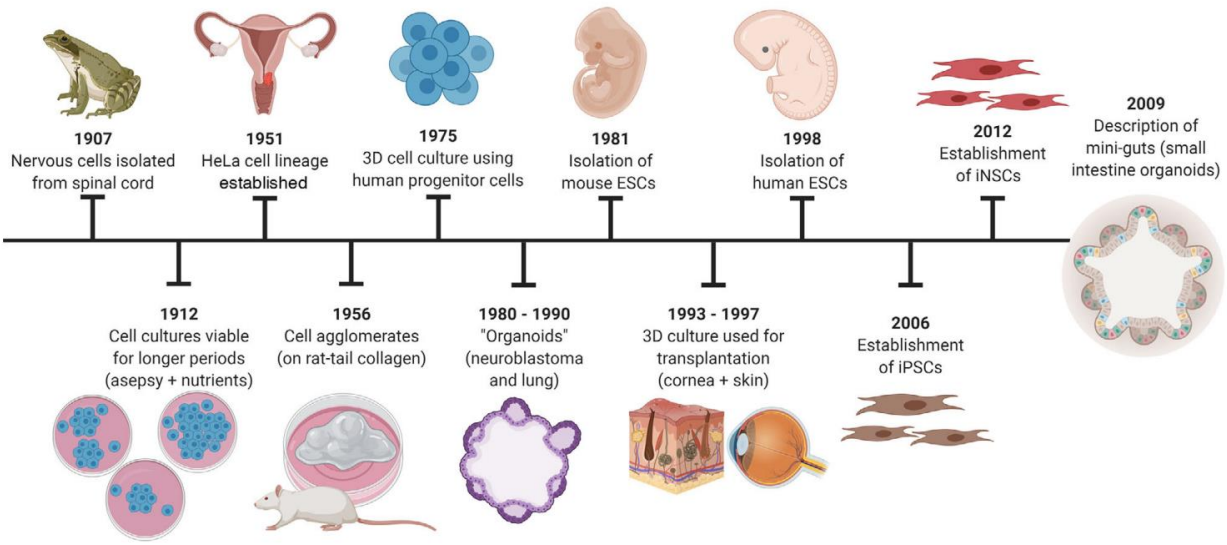

Figure 1.1 Timeline of the history of cell culture, from the original isolation of nervous cells from frog spinal cords to complex small intestinal organoids.[1] (Figure used with permission)

The ability to culture, passage, and test mammalian cells in a controlled lab setting revolutionized life sciences and drug discovery. Stemming from the first discovered immortalized cell line, HeLa cells from cervical cancer patient Henrietta Lacks in 1951,[2] researchers have sought *in vitro* mimics of human organ systems to be shared and grown with consistency across institutions. Since then, a diverse library of cell lines has been developed encompassing every niche of eukaryotic biology, with greater than 4,000 immortalized lines properly characterized and commercially available.[3]

1.1.1 The History of Cell Culture: From 2D to 3D

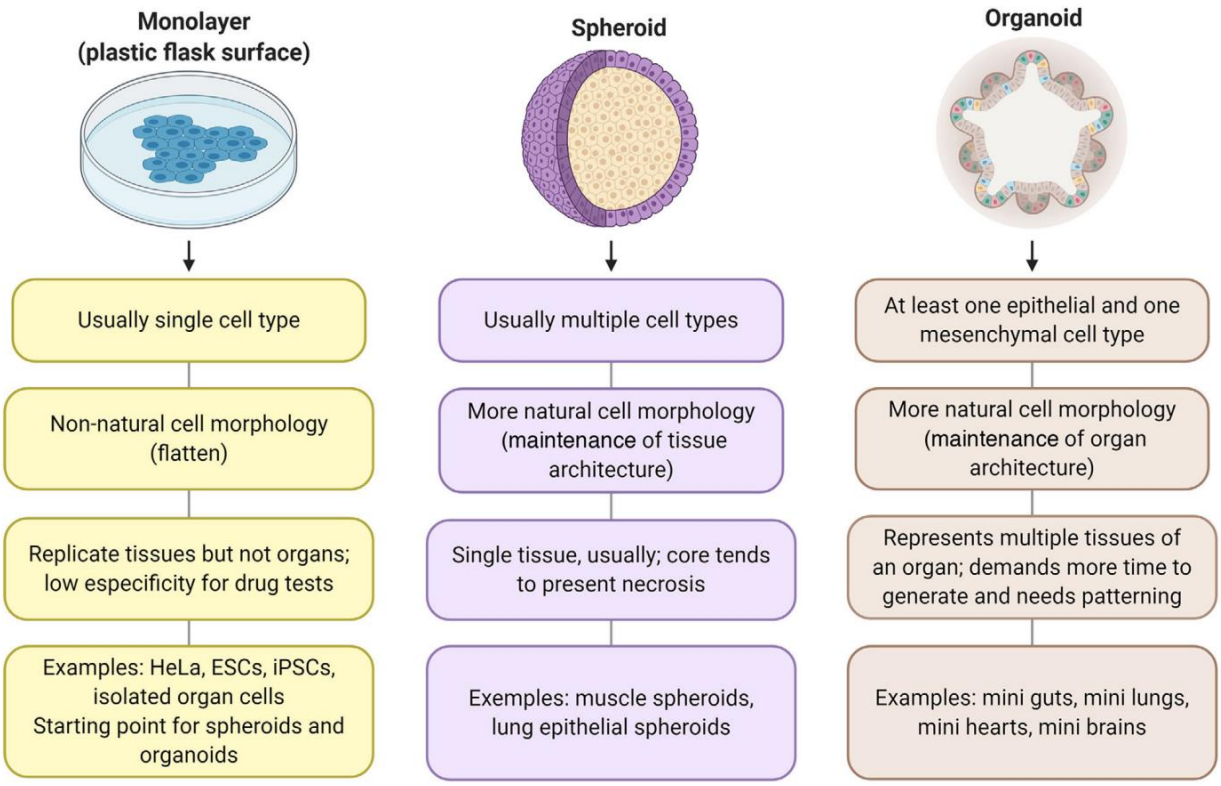

Figure 1.2 Comparison of monolayer, spheroid, and organoid cultures.[1] (Figure used with permission)

Traditionally, cells are grown on a flat surface resulting in a 2-dimensional (2D) monolayer.[4] Although the material and coating of cell culture surface have seen many iterations over the past few decades, 2D cultures are still commonplace and even used in standardized assays in research. They provide an affordable means to model mammalian physiology to either elucidate the functional intra/intercellular interactions or to test novel therapeutics before transitioning to animal models. Despite the widespread adoption, 2D cultures have limitations. Physically, cells are attached on one side to a surface and the other exposed to media. Generally, every individual cell is exposed to a comparable environment, and although there may be a degree of cell-to-cell contact, these systems do not capture the conditions in actual tissue.[5] Zonation, hypoxia, cell diversity, and fluid exchange are all not represented in 2D tissue culture.

Three-dimensional (3D) cell cultures attempt to fix these issues by providing a more tissue-like environment.[1,6] The added dimensionality provides space for added complexity and a large variety of culture vessels, often tailored to individual needs. As with 2D cell cultures, 3D cell culture techniques were attempted as early as in the early 1900s but were not reliably achievable until the 1950s when researchers began experimenting with round bottom plates and 3D cultures in collagen gels.[1] By the 1970s, hanging drop methods allowed formation of cell aggregates or spheroids, and thus achieving a cell system where every cell experiences a unique degree of cell-to-cell contact, fluid exchange, nutrient concentration, and oxygen exposure.

The 1980s introduced Matrigel, a basement membrane extract derived from mouse sarcoma cells, providing a supportive matrix for cell growth and maintenance in 3D.[7] Later in the 1990s other suitable hydrogels were designed to better model the varying consistencies for different cell types and organ compartments. These included optimization of previously used natural polymers such as collagen and alginate but also synthetic polymers such as polyethylene glycol. It was around this time where the importance of cell behavior in response to extracellular matrix (ECM) was discovered and therefore resulted in inclusion of ECM proteins to hydrogels.

1.1.2 Modern Techniques: Chips and Organoids

With the turn of the century and the push for interdisciplinary collaboration, an increase of biomedical engineers focused on designing microfluidic devices for 3D cell culture.[8] Microfluidic devices often deemed “chips”, position 3D cultures in a channel hooked up to a fluid pump to enable flow of media across cells. Simpler designs achieve media flow through without a pump by applying liquid gradients across compartments.[9] In the past decade, microfluidic devices have achieved a level of adoption so that they are now commercially available. Emulate Inc, founded in 2013, has been prominent in this field having successfully

developed a myriad of organ-on-chip models.[10–12] Although costly, these models are now amongst the best models for *in vitro* mimicry of human physiology.

Compartmentalization and localization of cells is an important aspect in 3D cell culture. In spheroids, cells may develop independently based on their seeded location but ultimately organization of the cells do not alter their function. This is the biggest differentiator of spheroids to organoids, complex 3D cell cultures which gained popularity in the 2010s following groundbreaking work by Dr. Hans Clevers and his team.[13] Clever's team developed a method to grow intestinal organoids, also known as "mini-guts," from adult stem cells. This achievement opened the doors to creating organoids from other organs and specific patients, leading to rapid advancements in the field.[14]

Organoids have since been generated for a wide range of tissues and organs.[1] and have become valuable tools for studying human development, disease modeling, drug discovery, and personalized medicine. Key uses of organoids in research include disease modeling, developmental biology, drug discovery and toxicology, precision medicine, and of course basic biological research. Organoid research is rapidly evolving, with ongoing efforts to improve their complexity, functionality, and scalability.[15] Although there are challenges to overcome, such as the lack of full organ functionality and the need for better vascularization, organoids hold great promise for advancing our understanding of human biology and revolutionizing various areas of medicine. Most recent advancements combine organoids with microfluidic devices effectively adapting complex biology in physiologically relevant environments.[16]

As expected, this has exploded into a voluminous catalog of technologies. With the passing of the FDA Modernization Act 2.0,[17] refuting the previous mandate of animal testing for new therapies, there is a push to identify the best *in vitro* model systems. Organoids and these

other advanced cell culture technologies are currently at the forefront of attention in drug development to overcome unreliable and inconsistent results from animal models. Despite the upcoming hurdles to identify and standardize these models, it is expected that the next generation of drugs will be discovered through organoid research.

1.2 The Liver and Drug-Induced Liver Injury

1.2.1 Liver Function and Make Up

The liver, found in all vertebrates, is a multifunctional organ which orchestrates an intricate array of physiological processes critical for maintaining homeostasis and overall organismal well-being.[18] Serving as an initial filter for all digested or injected substances, the liver metabolizes carbohydrates and lipids through a combination of hormonal and nutritional signaling to maintain homeostasis.[19] Typically one of the largest organ in the body, the liver acts as a metabolic hub managing biochemical reactions and pathways that govern nutrient metabolism, detoxification, bile production, storage, excretion, synthesis of blood components, and immune modulation. These functions are regulated by enzymatic activity, transcription factors, and signaling cascades. Bile production represents another pivotal function of the liver, playing a fundamental role in the digestion and absorption of dietary lipids.[20]

From orchestrating intricate metabolic processes and detoxification to bile production, storage and release of essential molecules, synthesis of blood components, and immune modulation, the liver is a highly sophisticated organ vital for sustaining systemic balance and overall health. Understanding the intricacies of hepatic physiology is crucial for deciphering the etiology and progression of liver diseases and developing targeted therapeutic interventions. This includes the detailed function of parenchymal (majority functional cell type) hepatocytes and non-parenchymal (minority cell types) cells.

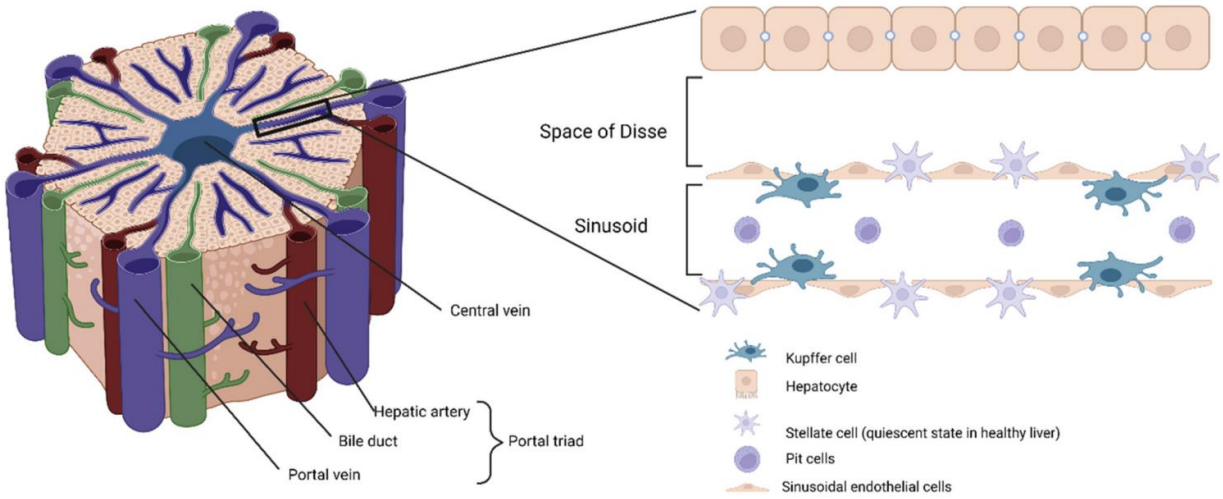

Figure 1.3 Sectional view of the diversity and organization of liver cell types.[21] (Figure used with permission)

1.2.1.1 Hepatocytes

Hepatocytes, the primary cell type in the liver, synthesize and secrete bile acids, cholesterol, phospholipids, and bilirubin, which collectively form bile.[20] Cholesterol, synthesized by the liver, is an essential precursor for bile acid synthesis. Bile acids, the primary constituents of bile, emulsify dietary fats in the duodenum, facilitating their enzymatic breakdown and subsequent absorption. Hepatocytes also synthesize various blood components that are indispensable for hemostasis and systemic homeostasis. They produce clotting factors, such as fibrinogen and prothrombin, essential for coagulation, thereby preventing excessive bleeding.[22,23] Hepatocytes also contribute to the production of albumin, a principal serum protein critical for maintaining colloid osmotic pressure, transport of small molecules in the bloodstream, and modulation of the body's protein balance.[24]

Another primary role of hepatocytes is detoxification, safeguarding the organism against endogenous and exogenous toxins.[25] Hepatocytes possess enzymatic systems, including cytochrome P450s (CYP450s), glucuronosyltransferases, and sulfotransferases, which facilitate the biotransformation and elimination of xenobiotics and endogenous waste products. Through a

series of phase I (e.g. reduction, oxidation, hydrolysis) and phase II (conjugation, glucuronidation, acetylation, sulfation) reactions, hepatocytes enzymatically modifies lipophilic compounds into hydrophilic metabolites, rendering them more easily excretable via bile or urine.[26] The hepatic detoxification machinery is further supported by efflux transporters that mediate the elimination of detoxified compounds directed into the bloodstream.[27]

1.2.1.2 Hepatic Stellate Cells

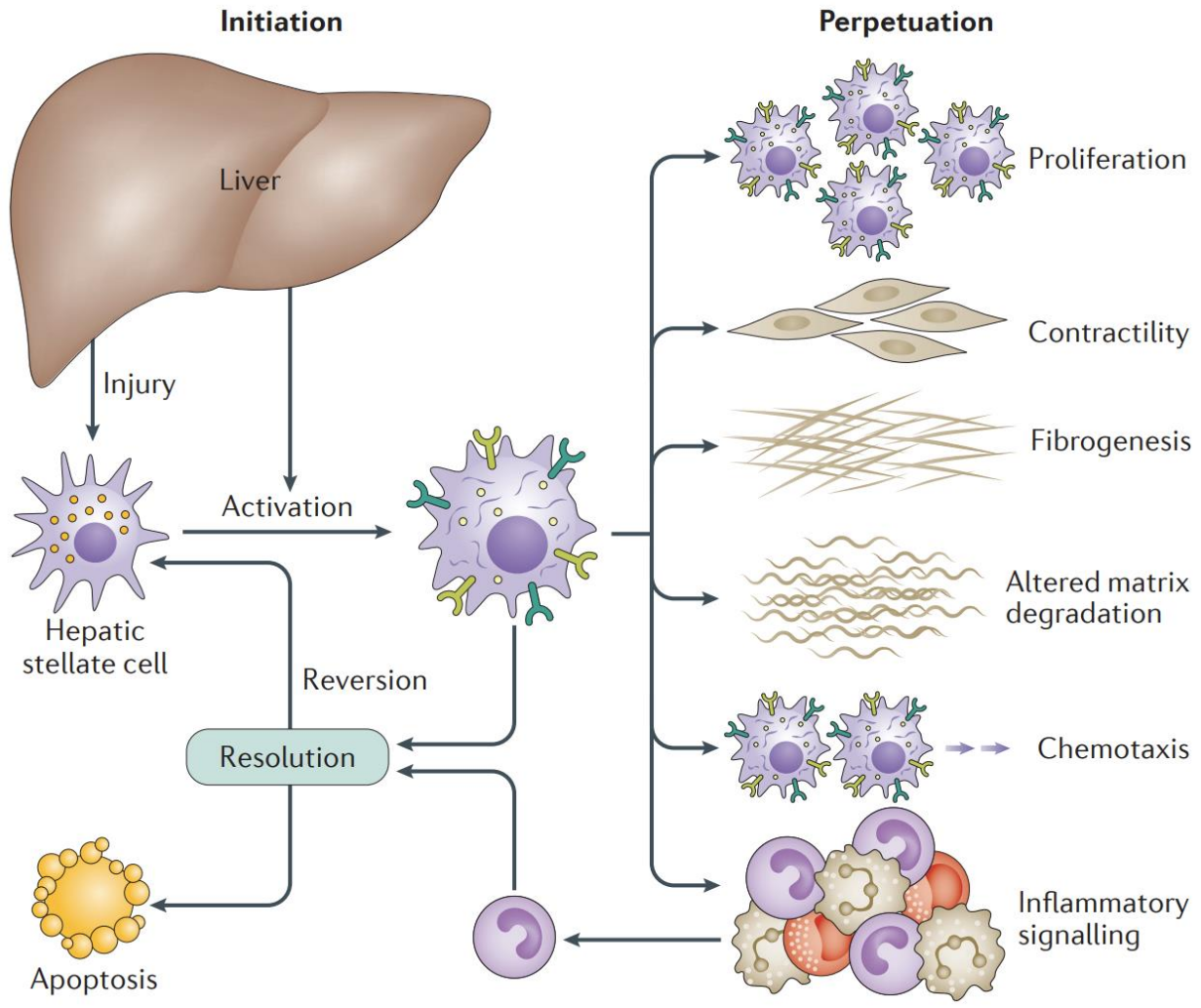

Figure 1.4 Description of the function and activation of HSCs and its downstream effects. Injury results in the activation of HSCs which can lead to HSC proliferation and downstream responses including immune responses and ECM changes.[28] (Figure used with permission)

Although the parenchymal hepatocytes encompass 70% of the liver's cells, the remaining is built up by a collection of non-parenchymal cells.[29] Hepatic stellate cells (HSCs), for example, make up 5-8% of cells found in the liver.[30] Stellate cells are functionally distinct compared to hepatocytes and play a crucial role in the liver's physiology and pathophysiology, particularly in liver fibrosis, a common pathological response to chronic liver injury. In the quiescent state, HSCs are characterized by their location in the space of Disse, residing near sinusoidal endothelial cells and hepatocytes. Quiescent HSCs feature a lipid droplet-rich cytoplasm, which serves as a reservoir for retinoids, vitamin A and vitamers. These stored retinoids are crucial for HSC quiescence, as well as for the maintenance of liver homeostasis and regeneration.[31]

Upon liver injury or in response to profibrogenic signals (e.g. TGFβ), HSCs activate and transition from a quiescent phenotype to an activated myofibroblast-like state (intermediate between a fibroblast and smooth muscle cell).[28] Activated HSCs play a central role in liver fibrogenesis, contributing to the accumulation of extracellular matrix (ECM) components, such as collagen, leading to liver fibrosis and exhibit enhanced proliferative, migratory, and contractile capabilities. They produce and secrete an array of ECM proteins, including collagens, fibronectin, and proteoglycans, which promote the formation of fibrotic scar tissue in the liver. Additionally, activated HSCs release profibrogenic cytokines, such as transforming growth factor-beta (TGF-β),[32] platelet-derived growth factor (PDGF),[33] and connective tissue growth factor (CTGF),[34] which further drive fibrogenesis by stimulating the proliferation and activation of HSCs themselves, as well as other liver cell types, including fibroblasts.

Besides their role in liver fibrosis, activated HSCs also contribute to the modulation of the liver's immune response. They can act as antigen-presenting cells, interacting with and activating immune cells, such as T cells, natural killer cells, and macrophages, through the

expression of surface molecules and the secretion of immunomodulatory factors.[35] This immunoregulatory function of HSCs influences the progression and resolution of liver inflammation and fibrosis.[36] Furthermore, activated HSCs play a role in angiogenesis, the formation of new blood vessels, within the liver.[37] They produce pro-angiogenic factors, including vascular endothelial growth factor (VEGF) and angiopoietin-1, which promote the expansion of the liver's vascular network. This angiogenic activity of HSCs is crucial for tissue remodeling during liver injury and repair processes.

Recent studies have also highlighted the heterogeneity of HSCs, suggesting the presence of distinct subpopulations with diverse functions.[38] Certain subpopulations of HSCs may possess regenerative and reparative capacities, contributing to liver regeneration and tissue repair following injury. Understanding the complex functions of HSCs and their involvement in liver fibrosis is important for developing targeted therapeutic strategies. Targeting the activation, proliferation, and ECM-producing capabilities of HSCs, as well as modulating their immune and angiogenic functions, represents potential avenues for intervening in liver fibrosis and promoting liver regeneration. Knowledge of HSC biology will aid in the development of novel anti-fibrotic therapies and identifying relevant properties to incorporate in liver model design.

1.2.1.3 Kupffer Cells

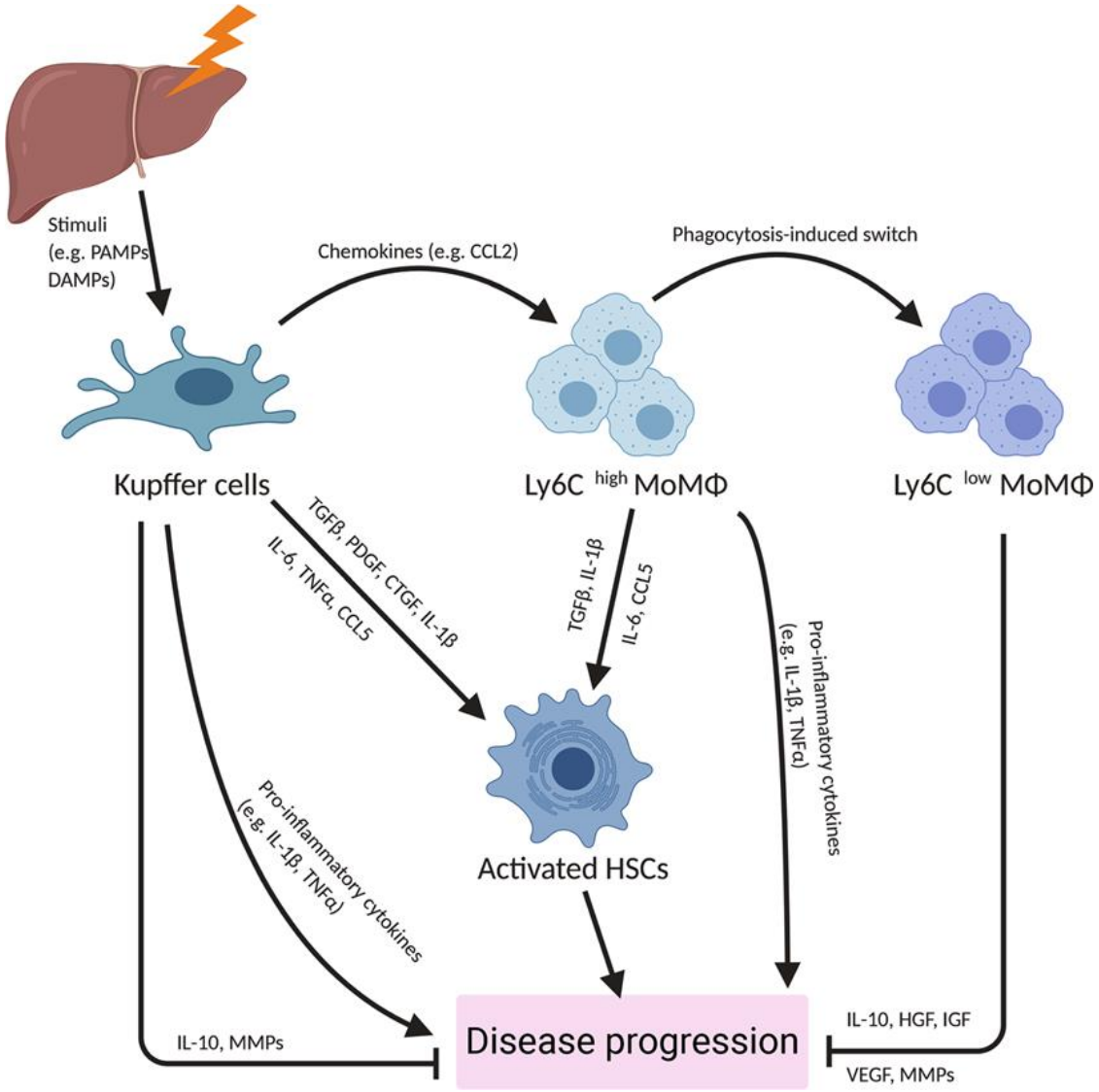

Figure 1.5 Kupffer cell activation and downstream signaling to monocyte-derived macrophages and hepatic stellate cells.[39] (Figure used with permission)

Kupffer cells, the resident macrophages of the liver, are immune cells that facilitate the liver's immune surveillance, homeostasis, and response to injury.[40] They exhibit a distinctive small and round morphology and are strategically positioned within the liver sinusoids, allowing them to detect and respond to stimuli, including pathogens, toxins, and damaged cells. Kupffer cells also survey the bloodstream for foreign particles, pathogens, and cellular debris. Through the expression of pattern recognition receptors, such as Toll-like receptors (TLRs), Kupffer cells

recognize and bind to pathogen-associated molecular patterns (PAMPs) and damage-associated molecular patterns (DAMPs).[41] This recognition triggers a cascade of immune responses, including the production and release of pro-inflammatory cytokines, chemokines, and reactive oxygen species (ROS), which serve to eliminate the threat and initiate the recruitment of other immune cells.

Kupffer cells, like other macrophages, possess phagocytic capabilities, enabling them to efficiently engulf and internalize pathogens, cellular debris, and immune complexes.[39] This phagocytic activity is supported by a plethora of surface receptors, such as scavenger receptors, complement receptors, and Fc receptors, which facilitate the recognition and uptake of opsonized particles.[42] Upon internalization, Kupffer cells can process and present antigens to T cells, thereby initiating adaptive immune responses. In addition to their immune surveillance role, Kupffer cells actively participate in the regulation of liver inflammation and immune responses. They serve as key modulators of hepatic immune tolerance, preventing excessive immune activation against harmless antigens from the gut, such as food antigens and commensal bacteria.[43]

Kupffer cells also contribute to the resolution of inflammation and tissue repair processes. As inflammation subsides, Kupffer cells transition from a pro-inflammatory to an anti-inflammatory phenotype. They secrete anti-inflammatory cytokines, such as interleukin-10 (IL-10)[44] and transforming growth factor-beta (TGF-β)[45], promoting the resolution of inflammation and tissue healing. Kupffer cells also produce growth factors and matrix remodeling enzymes that facilitate tissue repair and regeneration. Beyond their immune functions, Kupffer cells actively participate in the clearance and metabolism of endogenous and exogenous substances.[40] They contribute to the metabolism and elimination of drugs, bilirubin,

cholesterol, and other waste products. Kupffer cells express an array of drug-metabolizing enzymes and transporters, enabling them to modify and eliminate xenobiotics and metabolic byproducts.

Importantly, Kupffer cells are not a homogeneous population but exhibit remarkable heterogeneity.[46] Emerging evidence suggests the existence of distinct subsets of Kupffer cells with specialized roles in immune responses, tissue repair, or metabolic functions. Further research is needed to fully elucidate the functional heterogeneity of Kupffer cells and its impact on liver physiology and disease. Understanding the multifaceted functions of Kupffer cells is crucial for unraveling the complex interplay between the liver and the immune system, particularly as many serious liver diseases contain prominent immune components. Insights into Kupffer cell biology will contribute to the development of targeted therapeutic strategies for liver diseases, including viral hepatitis, alcoholic liver disease, non-alcoholic fatty liver disease, and liver fibrosis. Expanding our knowledge of Kupffer cell phenotypes and functions will pave the way for the development of novel immunomodulatory approaches in hepatology.

1.2.2 The Relationship Between the Liver and Drugs

The detoxification machinery found in the liver to manage exogenous substances modulates drug exposure in the body.[47] Understanding the intricate interplay between the liver and drugs is paramount for optimizing drug therapies, predicting drug responses, and mitigating potential adverse effects. Drug metabolism can lead to the activation or inactivation of drugs, ultimately modulating their pharmacological and toxicological properties. Hepatic drug metabolism entails enzymatic reactions catalyzed by cytochrome P450 enzymes (CYP450s) and other drug-metabolizing enzymes. These enzymes catalyze reactions, including oxidation, reduction, hydrolysis, and conjugation, generating metabolites that are more hydrophilic and

readily excretable.[48] Harbored primarily within hepatocytes, the functions not only facilitate drug elimination but also influence drug bioavailability and therapeutic efficacy.

The CYP450 superfamily comprises of 57 isoforms, with CYP3A4, CYP2D6, CYP2C9, and CYP2C19 being among the most clinically significant due to their relevance in drug metabolism.[49] Variability in the expression and activity of these enzymes can lead to significant variations in drug metabolism and, consequently, individual responses to drugs. The variations come in the form of genetic polymorphisms, drug-drug interactions, and environmental factors can profoundly influence the expression, activity, and regulation of drug-metabolizing enzymes, resulting differing therapeutic outcomes.[50]

While drug metabolism generally enhances the elimination of drugs, it can also generate metabolites that possess distinct pharmacological activities, occasionally contributing to therapeutic outcomes or adverse reactions. These mechanics are leveraged when designing drugs, such as in the case of designing “prodrugs”, a modified variant of an active compound to be metabolized in the body to restore the active compound.[51] Prodrugs are designed for pharmacokinetic purposes and often when the active compound has poor solubility or absorption. Apart from drug metabolism, the liver plays a crucial role in drug transport and disposition. Hepatocytes are equipped with an array of transporters, including uptake transporters (such as organic anion-transporting polypeptides, OATPs) and efflux transporters (such as P-glycoprotein, multidrug resistance-associated proteins, and bile salt export pump), which regulate the influx and efflux of drugs and their metabolites from the bloodstream.[52] These transporters determine drug concentrations within hepatocytes, impacting both intracellular drug metabolism and hepatic drug excretion into bile.

Understanding the intricate relationship between the liver and drugs is not only essential for optimizing drug efficacy and minimizing toxicity but also for predicting drug-drug interactions. Co-administration of drugs can lead to complex interactions, such as induction or inhibition of CYP450s[53] and transporters,[54] altering the pharmacokinetics and pharmacodynamics of co-administered drugs. For example, ritonavir, a protease inhibitor commonly used to support treatment of HIV, is a potent inhibitor of CYP3A4, an enzyme crucial for adequate elimination or prodrug metabolism of other drugs.[55] Ritonavir would then need to be prescribed carefully to ensure less adverse effects. These interactions can have significant clinical implications, necessitating careful consideration when prescribing drug regimens. A recent example is Paxlovid, a SARS-CoV-2 combinational therapy that includes ritonavir and therefore limits its use in elderly patients most susceptible to serious symptoms due to interactions with other drugs.[56]

1.2.3 Manifestation of Drug-Induced Liver Injury

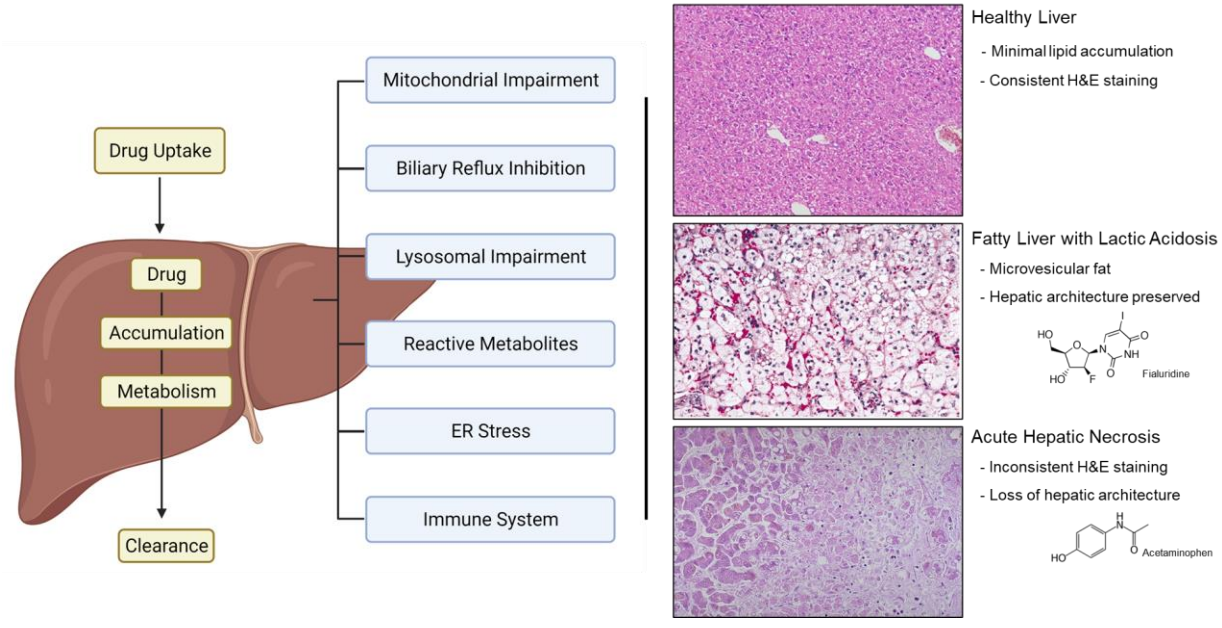

Figure 1.6 Overview of various mechanisms of actions involved in DILI[57] and the diverse histological presentations based on drug. While healthy liver histology includes consistent H&E staining with little lipid accumulation,

fialuridine-damaged liver present with large accumulation of microvesicular fat while acetaminophen-damaged liver presents with necrosis and loss of hepatic architecture. (Left figure recreated with permission)

Drug-induced liver injury (DILI) refers to a complex and multifactorial condition characterized by liver damage caused by the administration of therapeutic drugs, and herbal and dietary supplements (HDS), or other xenobiotics.[58] DILI represents a significant clinical challenge, as it can lead to liver dysfunction, hepatotoxicity, and, in severe cases, acute liver failure, necessitating liver transplantation and even death. Elucidating the mechanisms underlying DILI is crucial for understanding its pathogenesis, predicting individual susceptibility, and developing strategies to mitigate its occurrence. DILI can manifest in various forms, ranging from mild asymptomatic elevations in liver enzymes to severe hepatocellular or cholestatic liver injury.[59] The clinical presentation of DILI can be highly variable, with symptoms including fatigue, jaundice, abdominal pain, nausea, and altered liver function tests. The onset of DILI can occur shortly after drug initiation or after prolonged drug exposure, and its severity can be influenced by factors such as the dose, duration of treatment, genetic predisposition, and co-existing liver disease.[60]

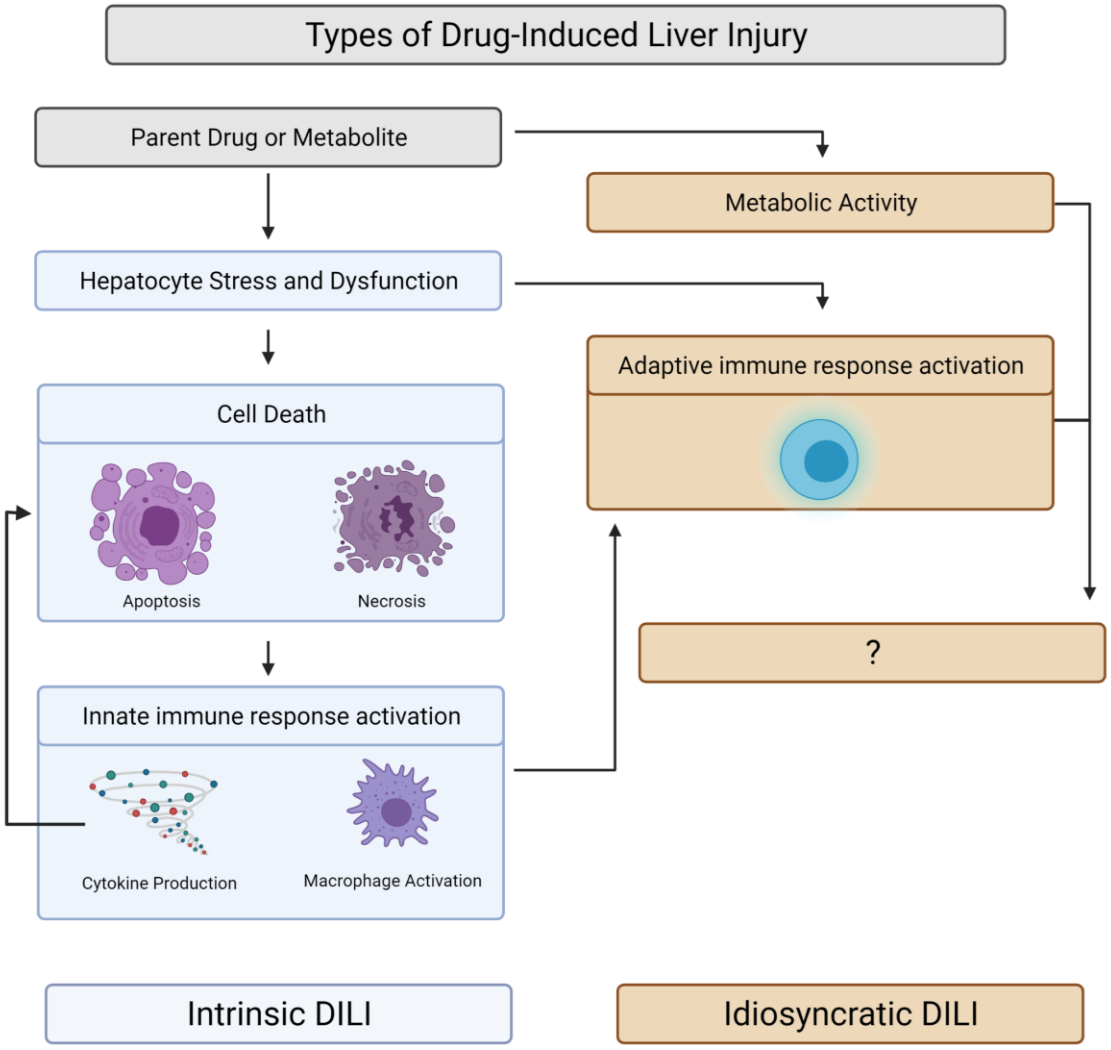

Figure 1.7 Flowchart describing the differences in occurrence of intrinsic and idiosyncratic DILI.[61] (Figure adapted with permission)

The pathogenesis of DILI is complex and multifaceted, involving a combination of intrinsic and idiosyncratic factors.[61] Intrinsic DILI is dose-dependent and predictable, resulting from direct hepatotoxic effects of the drug or its metabolites. It often occurs due to high doses, prolonged exposure, or inherent hepatotoxic properties of certain drugs, such as acetaminophen and nonsteroidal anti-inflammatory drugs (NSAIDs). The mechanisms underlying intrinsic DILI

include direct mitochondrial damage, oxidative stress, disruption of cellular membranes, and immune-mediated hepatocyte injury.

In contrast, idiosyncratic DILI is unpredictable and occurs in a small subset of susceptible individuals who exhibit an abnormal immune response to a drug. Idiosyncratic DILI is not dose-dependent and can occur even at therapeutic drug levels.[62] Evidence strongly suggests involvement of complex interplay between drug-related factors (such as drug metabolism, generation of reactive metabolites, and drug-induced immune responses) and host-related factors (such as genetic predisposition, altered immune regulation, and underlying liver disease). The exact mechanisms of idiosyncratic DILI remain elusive, but hypotheses include immune-mediated cytotoxicity, adaptive immune responses, and dysregulation of drug metabolism.

Immune-mediated mechanisms are increasingly recognized as playing a significant role in DILI.[63] Drug-specific T cells and activation of innate immune cells, such as natural killer cells and Kupffer cells, contribute to the immune response and hepatocyte injury. Inflammation and cytokine release further perpetuate liver damage and trigger a cascade of events leading to hepatocyte apoptosis, necrosis, and inflammation-mediated tissue remodeling. To mitigate the risk of DILI, preclinical and clinical studies are essential for evaluating drug safety profiles, identifying potential hepatotoxic effects, and developing biomarkers to predict individual susceptibility. The use of in vitro models, such as liver organoids and hepatocyte cultures, can facilitate the screening of drug candidates and provide mechanistic insights into DILI. Furthermore, pharmacogenomic studies aim to identify genetic variants associated with DILI susceptibility and help guide personalized drug therapy.

1.2.4 Drug-Induced Liver Injury in the Clinic

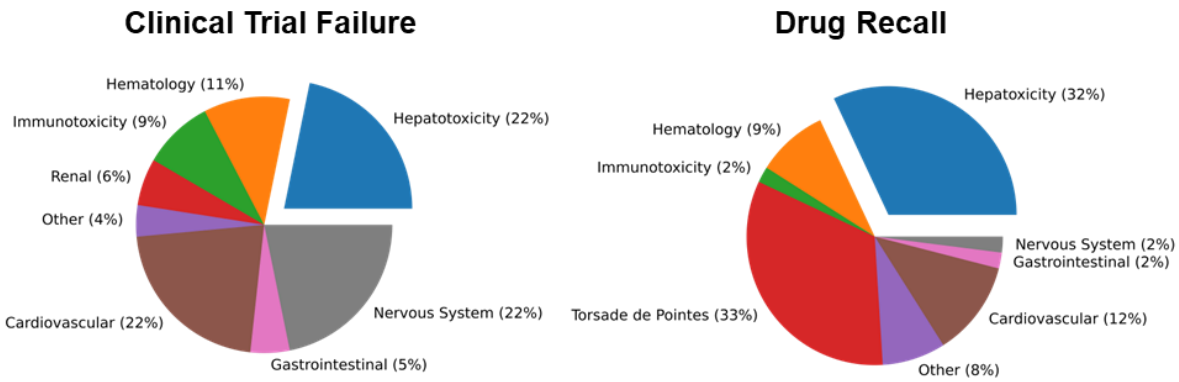

Figure 1.8 Classifications of all clinical trial failures and drug recalls by cause.[64] (Figure adapted with permission)

DILI poses a considerable challenge in drug development and clinical practice due to its infrequent occurrence, unpredictable nature, and potential for severe liver damage. Despite extensive preclinical and clinical evaluations, hepatotoxicity often goes undetected until a drug enters the market or is used in real-world clinical settings. An estimated 22% of clinical trial failures and 32% of market withdrawals of therapeutics are due to hepatotoxicity,[64] highlighting the role of the liver as a significant site of adverse drug reactions leading to drug failure. As there are currently over 1000 prescription medications and ~100,000 herbal and dietary supplements (HDS) available for use in the United States,[65] with 45% of all Americans reported taking at least one prescription medication in the past month and 11% reported taking more than 5 prescriptions, the potential for additive or synergistic liver toxicity is high.

Idiosyncratic DILI represents a subset of cases that occur sporadically and unpredictably, independent of a high drug dose or duration of use. These idiosyncratic reactions are often characterized by a prolonged latency period, ranging from weeks to months, and can manifest with diverse clinical presentations ranging from acute liver failure to jaundice. This uniqueness makes it difficult to predict and prevent idiosyncratic DILI during drug development and underscores the need for enhanced understanding of its underlying mechanisms.[66]

The consequences of DILI are not only limited to patient health but also have significant financial implications in drug development. Hepatotoxicity accounts for a substantial proportion of clinical trial failures and market withdrawals of therapeutics. The costs associated with these failures, along with the potential legal consequences, can be immense for pharmaceutical companies. Therefore, there is a pressing need to identify and mitigate hepatotoxicity risks early in the drug development process.[67] In addition to preclinical advancements, post-marketing surveillance systems, including pharmacovigilance programs, play a crucial role in identifying and managing DILI. These systems rely on voluntary reporting of adverse drug reactions by healthcare professionals and patients, as well as data mining from electronic health records and other sources. Timely detection and evaluation of DILI signals allow regulatory agencies to take appropriate actions, such as updating drug labels, issuing warnings, or even withdrawing drugs from the market when necessary.[68] The expanding field of pharmacogenomics holds promise for identifying genetic factors that may contribute to idiosyncratic DILI susceptibility. Genome-wide association studies (GWAS) and other high-throughput technologies are being utilized to uncover genetic variations associated with an increased risk of DILI.[69] This knowledge can potentially aid in the development of personalized medicine approaches, where patients' genetic profiles are considered to minimize the risk of DILI.

1.3 The Evolution of *In Vitro* DILI Models

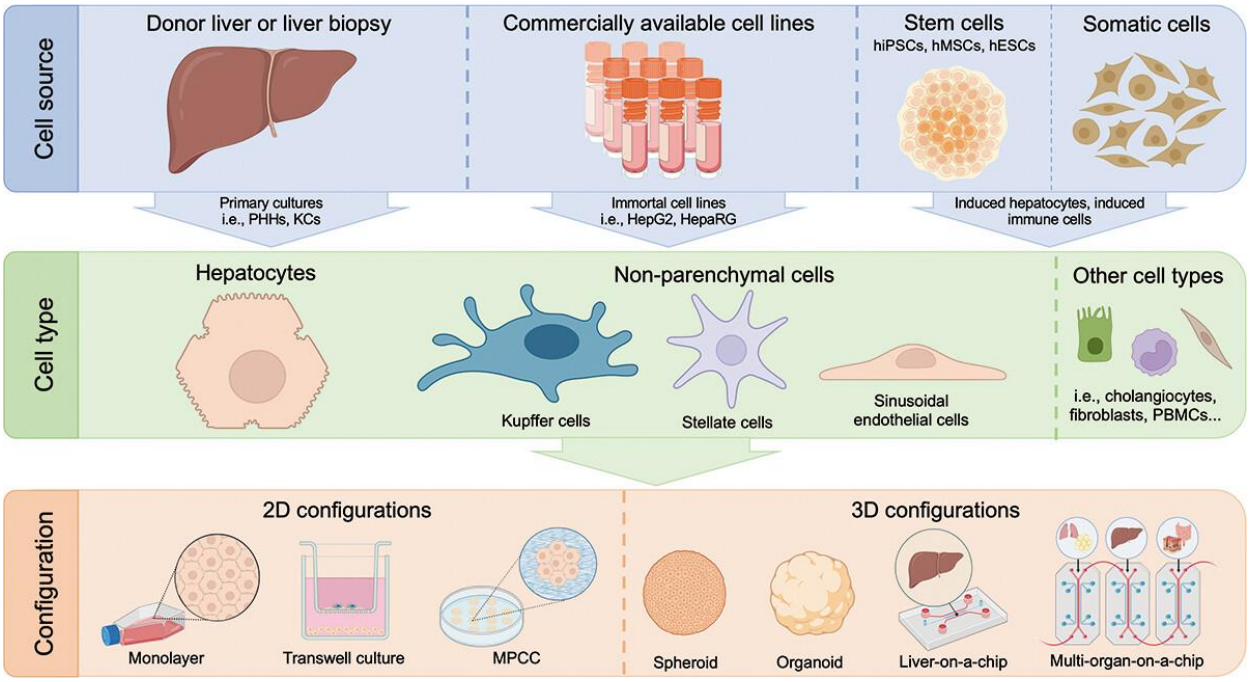

Figure 1.9 Existing liver models evaluated for DILI.[70] (Figure used with permission)

1.3.1 Primary and Immortalized Hepatocytes

The use of *in vitro* liver models began with the use of primary hepatocytes, isolated directly from animal or human livers in the 1980s.[71] Primary hepatocytes possess many essential liver functions, including drug metabolism and detoxification. Even with advancements in *in vitro* liver modelling, primary hepatocytes are still standard in preclinical drug safety assessment.[72] These assays measure parameters such as cell viability, metabolic activity, and alanine aminotransferase (ALT) or aspartate aminotransferase (AST) (hepatic enzymes shed from liver injury) activity as indicators of potential hepatotoxicity. Furthermore, primary hepatocytes can evaluate drug metabolism, including phase I and phase II drug-metabolizing enzyme activities, to identify potential hepatotoxic metabolites.

However, their cost, limited availability, rapid loss of functionality in culture, and inter-donor variability hindered their widespread use and unreliable translatability.[73] To address these

limitations, efforts were made to establish immortalized cell lines, such as HepG2, HepaRG, and Huh7 cells, which provided a readily available and more stable cell source. These cell lines allowed for easier manipulation and expansion, enabling high-throughput screening of drug candidates. However, they often exhibited reduced metabolic capacity and lacked key liver-specific functions compared to primary hepatocytes.[74] These cell lines are generally considered unreliable for DILI screening and are rarely used to give indication of how a drug may perform in clinical trials.

1.3.2 Liver Organoids: Primary and Stem Cells

The next significant breakthrough came with the development of primary hepatocyte liver organoids. As with other organoids, these involved the cultivation of hepatocytes in a 3D configuration, either as self-assembled aggregates or within hydrogels. 3D liver models demonstrate improved cellular functions, prolonged viability, and enhanced drug metabolism compared to traditional two-dimensional (2D) cultures.[75] However, challenges remain in terms of achieving long-term stability and reproducibility of these complex systems. Newer organoids attempt to add complexity to the model with the co-culturing of non-parenchymal cells during organoid formation.[76] Despite an improvement in liver-like function, the different cell types found in these organoids are assembled from different donors or immortalized cell lines and patient-specific function is lost.

Advances in stem cell technologies have revolutionized the field of liver organoids. Original efforts focused on developing hepatocyte-like cells from stem cells, although the lack of cell diversity mitigated the success of these cells as suitable DILI models.[77] Recently, the Takebe lab at the Cincinnati's Children's Hospital has been the most prominent in this field, recently developing and publishing their protocol to generate a multicellular liver organoid from stem

cells.[78,79] Induced pluripotent stem cells (iPSCs) reprogrammed from other cell types or human embryonic stem cells (hESCs) can be differentiated into hepatocyte-like, stellate-like, Kupffer-like, and biliary-like cells, offering a potentially unlimited and patient-specific cell source.

While still exhibiting signs of immaturity, these iPSC-derived organoids exhibit improved functionality and drug metabolism capabilities compared to immortalized cell lines, making them potentially valuable tools for personalized medicine and toxicity screening.[80] Because iPSCs can be split and grown indefinitely, development of a patient-specific iPSC line means other methods of differentiation can be done based on future research. Also, other cell types can be developed as deemed necessary and cell lines can be shared across research groups due to iPSC's viability. These are all key factors for studying idiosyncratic DILI as the disease phenomenon is complex and exact cell types for an appropriate model is not yet known.

1.3.3 Microfluidic and Multi-Organ Models

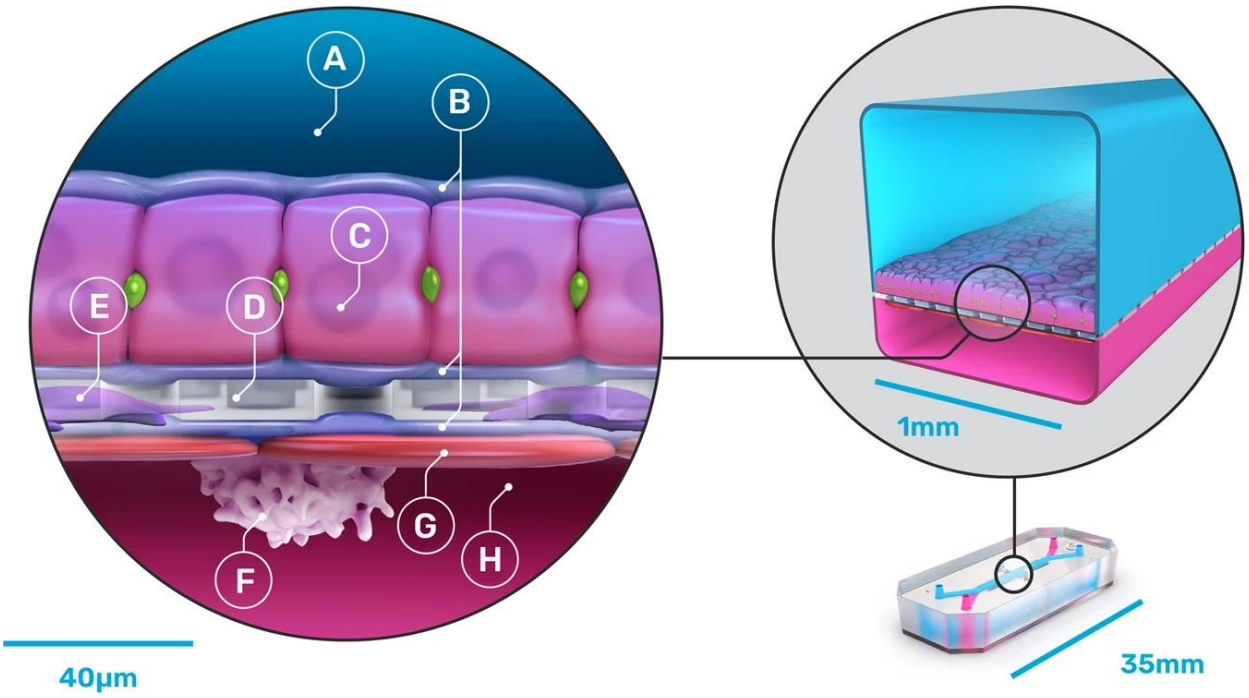

Figure 1.10 Schematic of an Emulate liver chip with an A) upper parenchymal channel with B) extracellular matrix, and C) hepatocytes, with a H) lower vascular channel separated by a D) porous membrane containing E) stellate cells, F) Kupffer cells, and G) LSECs[81]. (Figure used with permission)

As with other organ systems mentioned in Chapter 1.1.2, advancements in tissue engineering and microfabrication techniques led to the development of microscale liver models, often referred to as "liver- chip" or "organ-on-a-chip" platforms.[82] These microfluidic systems integrate multiple cell types, such as hepatocytes, endothelial cells, and Kupffer cells, within a physiologically relevant microenvironment. Emulate Inc is a key player in this area, having developed up to a quad-culture liver chip.[83] These models provide precise control over fluid flow, nutrient gradients, and cell-cell interactions, allowing for better recapitulation of liver physiology and response to drugs and have shown promising results in predicting drug metabolism, toxicity, and drug-drug interactions and seemingly capture donor-to-donor differences. Emulate initially demonstrated that their liver chip was able to capture species-specific responses to hepatotoxins, namely confirming that their human, rodent, and dog liver chip models were only responsive to hepatotoxins for the respective species.[11,81] Moving towards

preclinical drug safety assessment, Emulate has also shown that their liver chip identified hepatotoxins and non-toxins with a sensitivity of 87% and specificity of 100%, citing that this would result in large savings in drug development costs and de-risking clinical trials.

In parallel, efforts have been made to develop complex multi-organ systems, integrating liver models with other organ models, such as kidney, intestine, or lung. There are both organogenesis approaches (fusion of different organoid types into a single complex organoid system)[15] and "body-chip" platforms which connect liver chips with other organ chips.[84] Liver organogenesis has largely been focused on vascularization of liver organoids, often with liver sinusoidal endothelial cells (LSECs), and fusion with closely associated organs such as pancreatic organoids. Body-chips keep the different organ systems more compartmentalized, usually allowing only the media passthrough of one chip to enter the next without direct cell contact.[85] However, more recent advancements organize the different cell types in closer proximity on a single chip.

Overall, the evolution of in vitro liver models has progressed from simple 2D cultures to more sophisticated 3D systems and microfluidic devices. The integration of stem cell technologies, tissue engineering approaches, and microfabrication techniques has significantly enhanced the physiological relevance and predictive capabilities of these models. Future directions involve further improvements in long-term stability, scalability, reproducibility, and incorporation of additional cell types and organs to achieve even more comprehensive and realistic models of liver physiology and drug response, ultimately standardizing them for preclinical assays. Barriers still exist in confirming biological relevance to human physiology and robustness in capturing DILI events.

1.4 High-Content Screening Applications in DILI Research

Traditional methods for assessing DILI, such as animal models and biochemical assays, have limited predictive accuracy for human hepatotoxicity. High-content screening (HCS) techniques provide a more advanced approach by integrating automated imaging, image analysis, and multivariate data analysis.[86] This is crucial in observing hepatotoxicity as no concrete markers have been identified and because hepatotoxicity arises through a unique mechanism of action depending on the culprit drug.[87] HCS enables the evaluation of complex cellular responses and early identification of potentially hepatotoxic compounds during drug development.

1.4.1 High-Content Screening Techniques

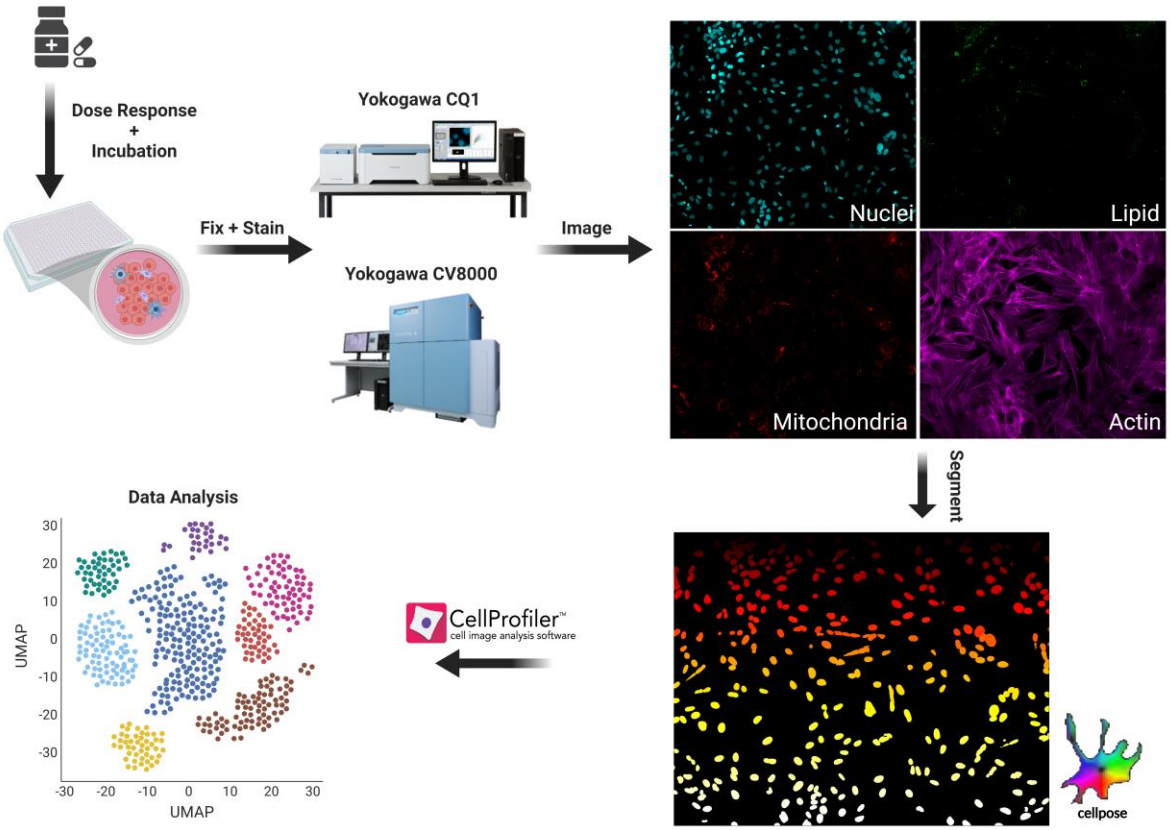

Figure 1.11 A simplified overview of the steps involved in a standard high-content screen from cell culture and drug treatment to image acquisition and analysis.

1.4.1.1 Automated Imaging Platforms:

HCS platforms utilize automated microscopy systems to capture images of cells. These platforms offer high throughput, enabling the simultaneous screening of thousands of compounds.[88] Simpler platforms may use a single acquisition camera, an automated stage, and a widefield microscope whereas higher end models may allow for simultaneous acquisition of multiple fluorescent channels, be equipped with confocal microscopy, automate water immersion imaging, have built in liquid handlers, and/or allow for detailed environmental control.[89]

The preferred form factors for HCS assays are generally 384-well plates, which balance throughput and cell culture conditions, although 96 and 1536-well plates are also frequently used.[90] Across all HCS platforms, a key feature is capability in imaging the exact x-y-z location in every well to maintain consistency in acquired data. This is to combat artifacts that arise during the cell culture and treatment period, such as cell accumulation on edges or plate effects.[91]

1.4.1.2 Fluorescent Probes and Biomarkers:

Specific fluorescent probes and biomarkers are used to assess relevant cellular processes in DILI research, such as mitochondrial dysfunction, oxidative stress, apoptosis, and inflammation. These probes enable the visualization and quantification of specific cellular events within the high-content screening format. HCS assay development focuses on optimization of a stain set: a set of small molecule dyes and antibody systems to provide detailed representation of a cell in the context of any given assay.[92]

Cell Painting,[93] developed by Anne Carpenter's group at the Broad Institute, is a popular approach in designing stain sets where cells are stained to observe key components rather than for specific markers. These components are usually nucleus, endoplasmic reticulum, mitochondria, cytoskeleton, Golgi apparatus, and RNA but exact sets can be dependent on the

specific assay. Therefore, assays are developed with the goal of identifying compounds to alter a diseased cell's overall morphology into that of a healthy cell rather than the unreliable increase or decrease of disease-associated markers.

1.4.1.3 Image Analysis and Data Processing:

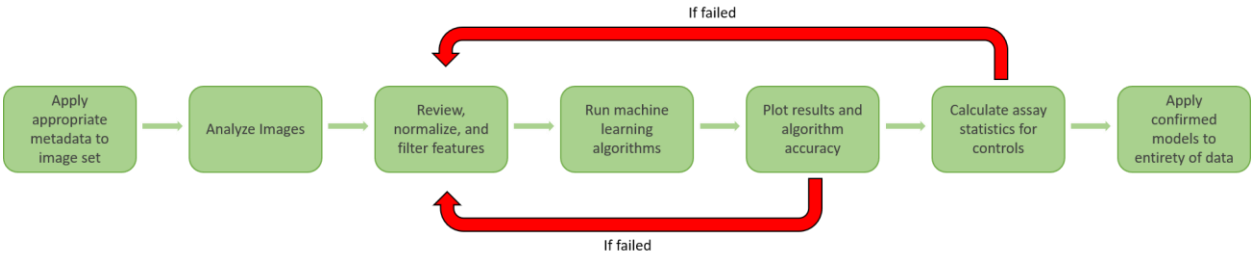

Figure 1.12 Standard workflow for image analysis and machine learning

Namely, the Cell Painting approach leverages image analysis and deep phenotyping to tease out and quantify perturbations by drug treatments through machine learning-enabled multivariate analyses.[94] Also developed by the Carpenter group is the open-source CellProfiler image analysis software which enables automated nuclei and cell segmentation followed by heavy feature extraction.[95] Although other image analysis methods exist, CellProfiler provides an easily approachable package to integrate into a research group's data analysis workflow, particularly that of an academic group. As an open-source software both the input and output of data through CellProfiler is compatible with suites such as JMP or KNIME and integration of other segmentation methods such as Cellpose[96], a machine learning-based segmentation tool, is seamless.

The hundreds or thousands of cell-level feature measurements would then need machine learning-based methods to interpret. These algorithms identify morphological changes, measure protein expression levels, assess subcellular localization for each cell and compare them across treatments.[97] Models such as random forest or linear discriminant analysis can be built around

positive and negative controls and then used to score unknowns.[91] In such cases where concrete positive control does not exist, distance scoring can be used to identify treatments which result in the largest morphological perturbation compared to control.

Complex assays, however, generally require an added degree of difficulty in terms of image/data analysis. Co-cultures for example generally require an initial categorization of cell types achieved by either specific markers or based on cell morphology.[98] 3D cultures can be analyzed by individual z-slices which are then correlated with one another as a whole, but at any rate is finicky with many research efforts focused on improved algorithms.[99] Lastly, live-cell imaging analyses involve either whole-image motility scoring or individual cell tracking.[100]

1.4.2 Early HCS for DILI

Early popularization of HCS assays in the 2000's led to the design of high-throughput assays to detect hepatotoxicity. Many of the early attempts in developing these assays for DILI involved sifting through the non-direct endpoints such as lipid accumulation, reactive oxygen species, and mitochondrial activity in relation to hepatotoxicity. It was quickly determined that immortalized cell lines such as HepG2 could predict certain forms of human hepatotoxicity given morphological endpoints such as mitochondrial membrane potential and membrane permeability in addition to simple loss of cell viability.[101] Similar assays quickly emerged with the use of primary human hepatocytes which provided an extremely low false positive rate but with variable accuracy.[102] Although demonstrating the utility of HCS and consideration of morphological measurements in assessing DILI, physiological relevance was poor. These assays did not incorporate cell diversity in the liver nor administer compounds and realistic concentration and therefore translatability to humans was poor. As a result, almost two decades later there has not been a standardized HCS assay for DILI that has seen widespread adoption.

With realistic compound concentrations in mind many later assays incorporated a concentration cutoff in determining hepatoxicity. Feature acquisition became more numerous and complex and thresholds for hepatotoxicity were determined based on the observation of an hepatotoxic measurement being well below a compound's C_{max}.[103] Despite these efforts to achieve relevance, and although the assays demonstrated low false positive rates, they were still not able to reliably detect true positives.

1.4.3 Mechanism Focused HCS Assays

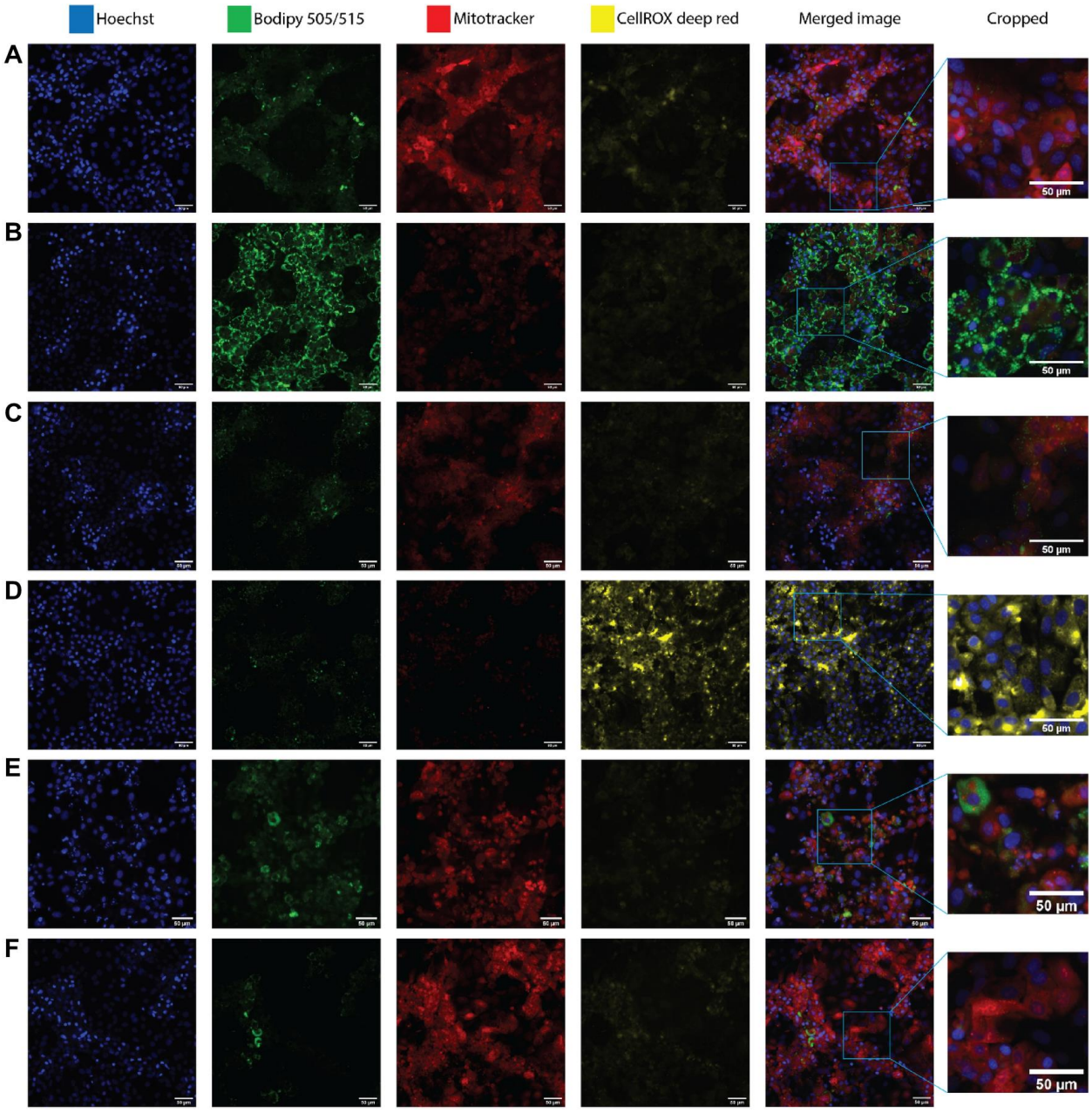

Figure 1.13 HCS images of HepaRG cells treated with A) DMSO control, B) oleic acid, C) rotenone, D) amiodarone, E) mendione, and F) caffeine to show various routes of hepatotoxicity through staining with BODIPY (lipids), mitochondria (Mitotracker), and ROS (CellROX deep red).[104] (Figured used with permission)

Other HCS DILI screens asked more directed questions focusing on specific DILI mechanisms in addition to cell viability obtained from nuclei counts. For example, those focusing on cholestasis developed assays to interrogate bile salt transport mechanisms and showed a high success rates in not only identifying cholestatic compounds but also in not falsely

identifying non-cholestatic DILI compounds.[105] Importantly, these compounds are rarely identified in animal testing due to deviations in rodent bile salt content and transport compared to humans. The high accuracy and relative ease of scalability for novel compound screening resulted in multiple developments of cholestatic-focused assays.

Compound-induced steatosis, which clinically presents as steatotic liver, has also been of focus in developing HCS screens. Steatosis in hepatocytes can be easily measured with BODIPY[106] and LipidTOX[107,108] stains. These stains allow for the direct visualization and quantification of lipid droplets within cells. While lipid measurements by themselves do not provide an adequate assessment of hepatotoxicity, their inclusion in multiparametric assays have shown to improve results[104,106]. Lipid content may also be more crucial for assessing hepatotoxicity of certain compound classes more prone to causing steatosis.[107]

Mitochondrial impairment is also emphasized in HCS assays but features a diversity of morphological. Ingeniously, HCS assays have been developed to capture all listed mitochondrial perturbations with a single stain set for nuclei, mitochondria, intracellular calcium, and ROS [109]. This stain set allows for measurement of total mitochondrial mass through mitochondrial fluorescence, membrane permeability and intracellular calcium based on calcium localization, reactive oxygen species (ROS) production and localization, and cell death as a result of either necrosis or apoptosis based on cell morphology.[110]

Mitochondrial impairment resulting in ROS has seen particular interest in HCS DILI assays. ROS-induced oxidative stress occurs when generation of oxidant species, mainly from the mitochondrial respiratory chain, surpass the antioxidant capabilities of the cells leading to DNA, protein, and lipid damage.[111] Oxidative stress can occur through impairment of the mitochondrial respiratory chain,[112,113] depletion of antioxidant reduced glutathione,[114] production

of electrophilic metabolites,[115] or redox cycling-induction.[110,116]. While GFP linkage to a direct reporter such as p21, ICAM1, CHOP, or Srnx1 exist,[117] HCS assays often prefer more general ROS stains for an unbiased approach in multiparametric feature measurement. Stains such as CellROX and MitoSOX serve this goal and react directly with ROS for fluorescence.[118,119] BODIPY, commonly used as a lipid stain, can also be used as an indirect informer of lipid-modulating ROS.[120]

Many ROS-based HCS screens have been developed with a degree of success. With emphasis on low variability and ease of scalability, most of these assays have been developed based around HepG2 or HepG2 reporter cell lines.[102,117,118,121–125] Although efforts to achieve physiological relevance have focused around developing ROS specific assays around human hepatocytes[102,126,127] or iPSC-derived cell lines.[128,129]

1.4.4 Co-Culture and 3D HCS Assays

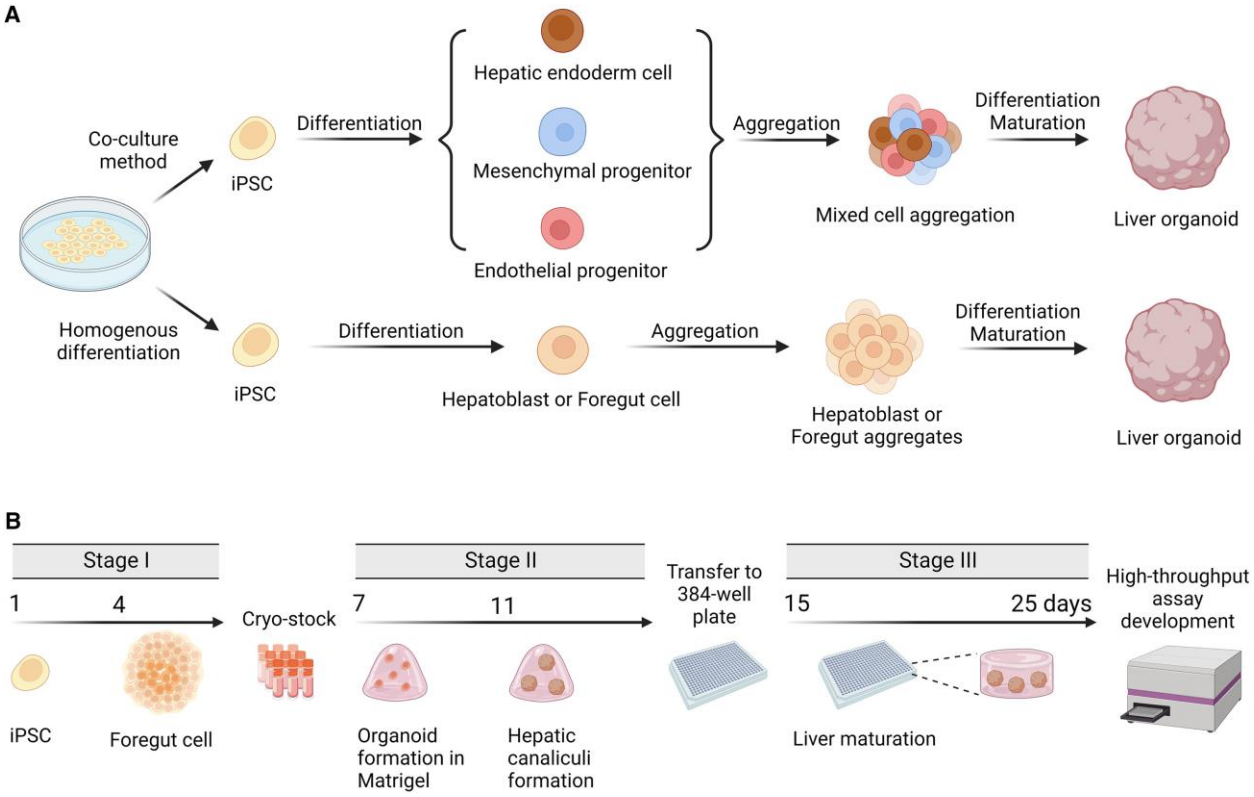

Figure 1.14 Schematic demonstrating A) common processes of deriving liver organoids from iPSCs and B) use of liver organoids as tools in HCS.[130] (Figure used with permission)

Although single cell line assays show greater representation of hepatotoxicity through HCS-enabled multiparametric measurements versus single-endpoint assays, there still exists a limitation due to false negatives. These compounds are suspected to be missed in these assays if their DILI mechanism requires vascularization, is a result of fibrosis, or immune-mediated, calling for the inclusion of other cell types.[131–134] While simply differentiation immortalized HepG2s improve their modelling capabilities,[135] further improvements are seen by mixing immortalized hepatocytes and monocytes/macrophages suggested more accurate DILI modelling, even potentially idiosyncratic DILI modelling[136,137] while formation of multicellular liver spheroids/organoid provided further liver representation.[76,138,139]

As aggregation of cells into 3D spheroids is often done in round bottom plates which are available in high-throughput formats they have seen widespread adoption in building accurate

HCS DILI assays.[140,141] However, with these methods it is near impossible to achieve spheroids/organoids with multiple cell types originating from the same organism let alone from the same human patient let alone acquiring enough cell material for screening purposes. iPSC-derived HLOs allow us to meet this need as whole organoids consisting of both parenchymal and non-parenchymal liver cells can be grown from a single lineage.[78] These iPSC-derived liver organoids have shown remarkable accuracy in HCS assay with nearly 90% sensitivity and specificity,[80] outperforming any of the previous models. iPSC-derived HLOs even maintain donor biology by capturing patient-specific DILI responses. Despite their outstanding performance, HLOs still have limitations as a tool in HCS due to inter-organoid variability and difficulty in assortment onto high-throughput formats.[130]

As described in Chapter 2, HLOs can still be used in high-throughput through trypsinization into a single-cell dispersion for plate seeding, and while many of the hepatocyte and non-parenchymal functions maintain cell to cell contact is lost. However, this format does gain an added capability of clear single-cell resolution and segmentation to obtain concrete morphological measurements for machine learning that may provide added detail in understanding DILI mechanisms. Also described in Chapter 2 is the culture of these dispersed cells onto a microfluidic chip system that demonstrates improved physiological relevance and capabilities to accurately model DILI.

While Chapter 2 introduces microfluidic chip-based iPSC-liver models, limitations in their throughput and cost to develop is highlighted. Chapter 3 explores the use of a higher throughput microfluidic system amenable to existing lab automation technologies. Additionally, Chapter 3 tests this new system as a long-term model of DILI, successfully maintaining HLO integrity up to 28-days post-transfer.

Chapter 2 Characterization of an iPSC-Human Liver Organoid Platform for Intrinsic DILI

2.1 Summary

Drug-induced liver injury (DILI), both intrinsic and idiosyncratic, causes frequent morbidity, mortality, clinical trial failures and post-approval withdrawal. This suggests an unmet need for improved in vitro models for DILI risk prediction that can account for diverse host genetics and other clinical factors. In this study, we evaluated the utility of human liver organoids (HLOs) for high-throughput DILI risk prediction and in an organ-on-chip system.

HLOs were derived from 3 separate iPSC lines and benchmarked on two platforms for their ability to model in vitro liver function and identify hepatotoxic compounds using biochemical assays for albumin, ALT, and AST, microscopy-based morphological profiling, and single-cell transcriptomics: 1) HLOs dispersed in 384-well formatted plates and exposed to a library of compounds. 2) HLOs adapted to a liver-on-chip system.

1) Dispersed HLOs derived from the 3 iPSC lines had similar DILI predictive capacity to intact HLOs in a high-throughput screening format allowing for measurable IC50 values of compound cytotoxicity. Distinct morphological differences were observed in cells treated with drugs exerting differing mechanisms of toxicity. 2) On-chip HLOs significantly increased albumin production, CYP450 expression, and ALT/AST release when treated with known DILI drugs compared to dispersed HLOs and primary human hepatocytes. On-chip HLOs were able to

*The contents of this chapter have been published: Zhang, C. J. et al. A human liver organoid screening platform for DILI risk prediction. J. Hepatol. 78, 998–1006 (2023).

predict the synergistic hepatotoxicity of tenofovir-inarigivir and showed steatosis and mitochondrial perturbation via phenotypic and transcriptomic analysis with exposure to FIAU and acetaminophen, respectively.

The high throughput and liver-on-chip system exhibit enhanced in vivo-like function and demonstrate the potential utility of these platforms for hepatotoxicity risk assessment. Tenofovir-inarigivr associated hepatotoxicity was observed and correlates with the clinical manifestation of DILI observed in patients.

2.2 Introduction

Drug-induced liver injury (DILI) is an infrequent but important cause of both acute and chronic liver disease.[142,143] An estimated 22% of clinical trial failures and 32% of market withdrawals of therapeutics are due to hepatotoxicity.[64,144] Hepatotoxicity is typically not identified until clinical trials or post-marketing which creates an increased risk for clinical trial participants as well as a financial burden in drug development. Most instances of DILI are termed “idiosyncratic,” since they are largely independent of the dose and duration of drug use and develop in only a small proportion of treated patients for as-yet unclear reasons. As there are currently over 1000 prescription medications and >80,000 herbal and dietary supplements (HDS) available for use in the United States[65], the potential for additive or synergistic liver toxicity is high with low predictive capability.

Recently, inarigivir soproxil (GS-9992) was investigated against Hepatitis B (HBV).[145] Inarigivir monotherapy showed no clear signs of toxicity in two clinical trials for HBV. However, a later phase-2 inarigivir/tenofovir study identified severe DILI in patients given the combination of both drugs after 16 weeks of therapy that lead to the discontinuation of this drug development program. All 7 patients had an elevated alanine aminotransferease (ALT) after 16

weeks of therapy, 4 of the 7 had associated hyperbilirubinemia, and one subject died due to multiorgan system failure with lactic acidosis and evidence of hepatic steatosis.[146] Yet, recent studies continuously demonstrate the safety of inarigivr as a lone treatment.[147] These clinical trial findings emphasize the need for high fidelity pre-clinical DILI risk prediction. Primary human hepatocyte (PHH) cell cultures currently used in these assays retain hepatocyte function but decline rapidly in metabolic function and vary greatly between cadaveric fresh and cryopreserved samples.[148] PHH availability and source patient diversity is also limited preventing their use in large-scale screening for DILI-risk.[73]

To meet this challenge, we explored the use of human liver organoids (HLOs) as a more physiologically organotypic system for recapitulating DILI in vitro, with added adaptations for high-throughput screening. HLOs consist primarily of hepatocyte-like cells while also containing non-parenchymal-like cells derived from the same individual donor.[78] In this study, we utilized a previously-developed protocol for derivation of HLOs from induced pluripotent stem cells (iPSC)[79] allowing for a personalized approach in assessing DILI based on iPSC donor selection. We adapted HLOs both for high-throughput drug screening in 384-well plates and for enhanced physiological fidelity in a liver-chip system (Emulate Bio)[149] previously used to successfully predict species-specific DILI with PHHs.[11,83]

Due to the complexity and inconsistency of DILI based on culprit drug modality, we developed an integrated multi-omics platform including biomarker/analyte detection, high content imaging-enabled phenotyping, and single-cell RNA sequencing to deliver a comprehensive platform for dissection of DILI with inarigivir + tenofovir as a benchmark. In this study, we demonstrate the potential of dispersed HLOs for rapid 384-well based compound

DILI-risk screening, and also the validation of a patient-derived liver-on-chip (PaDLOC) system for a more intricate and mechanistic assessment of DILI pathogenesis.

2.3 Results

2.3.1 Use of Dispersed HLOs in 384-well Based High-Content Screening and Drug Clustering

A

Compound	72.3 IC_{50} (μM) (95% CI)	2E IC_{50} (μM) (95% CI)	CC3 IC_{50} (μM) (95% CI)
allopurinol	1.385 (1.074 - 1.792)	2.259 (1.646 - 3.105)	1.689 (1.220 - 2.341)
amiodarone	6.411 (4.907 - 8.364)	0.1688 (0.1075 - 0.2677)	1.638 (0.6478 - 4.114)
dihydrotestosteron	1.522 (1.085 - 2.133)	1.24 (0.7047 - 2.183)	0.3193 (0.1879 - 0.5613)
fialuridine	0.3346 (0.2690 - 0.4166)	0.1139 (0.06868 - 0.1947)	3.384 (1.222 - 8.116)
fioxuridine	10.36 (7.714 - 13.96)	0.3767 (0.2355 - 0.6092)	1.648 (0.9472 - 2.914)
nevirapine	31.38 (19.82 - 52.05)	0.2907 (0.1836 - 0.4682)	0.1476 (0.07711 - 0.2962)
propythiouracil	0.8621 (0.5314 - 1.418)	1.793 (0.9616 - 3.360)	4.079 (2.420 - 6.751)
rifampin	22.29 (14.40 - 35.31)	2.157 (1.467 - 3.178)	0.573 (0.4225 - 0.7795)
stavudine	0.1502 (0.08708 - 0.2732)	1.665 (0.9105 - 3.033)	0.1931 (0.1333 - 0.2814)
tamoxifen	1.216 (0.8984 - 1.655)	0.8463 (0.6083 - 1.177)	4.048 (2.935 - 5.593)
terbinafine	4.175 (3.176 - 5.511)	0.415 (0.2670 - 0.6498)	2.65 (1.934 - 3.616)
thioguanine	6.017 (3.964 - 9.244)	2.887 (2.251 - 3.704)	37 (20.94 - 69.85)

B

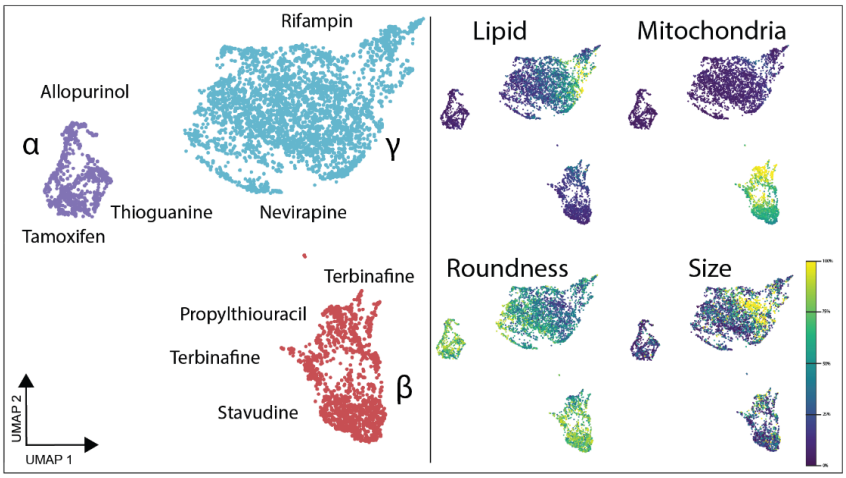

Figure 2.1 384-well adaptation of HLOs. HLOs grown from iPSC lines 72.3, 2E, and CC3 are dispersed into 384-well plates and treated with a 10-point dose response of 12 common DILI causing compounds. After 120 hrs incubation, cells are fixed and stained with Hoechst 33342, MitoView Green, HCS CellMaskOrange, and LipidTox DeepRed and imaged with an automated confocal microscope. (A) IC50 values of these compounds through cell viability counts are calculated (n=4 per concentration, per cell line). (B) CellProfiler was used to extract features at each compound's respective IC50 values for 72.3-derived HLOs and embedded into UMAP. Plot points represent individual cells. Color intensity dictates the percentage of max measurement for each feature.

Foregut spheroids from iPSC lines 72.3[150] (male fibroblast derived), 2E[151] (female fibroblast derived), and CC3[152] (female fibroblast derived) were generated through a 6-day differentiation and subsequently differentiated to HLOs over a 20-day period.[78,153] 3D confocal immunofluorescence imaging shows positivity for HNF4A to identify hepatocytes, α-SMA to identify stellate-like cells, and CD68 to identify Kupffer cells (Figure 2.5A-B). Here, we dispensed 3,500 dispersed HLO cells/well in 384-well plates and observed slow proliferation across 7-days while they retained cell-type-specific markers (Figure 2.5A-C) on day 7 of culture. CellProfiler 4.2.0[154] cell segmenting determined 64.6-75.2% were positive for HNF4A, 18.7-

32.4% for α-SMA, 0.12-0.19% for CD68 and 2.93-5.91% for neither (Figure 2.5C). These cell ratios match previously determined cell distribution through single-cell RNA sequencing (scRNA-seq).[78]

With confirmation of retention of cell type specific markers and ratios in a 384-well format as in intact HLOs, a collection of 12 DILI-associated drugs were screened through HLOs developed through three different iPSC lines to characterize the drug-induced perturbation of single-cells in response to 12 hepatotoxic drugs from 384-well plate screening. These 12 compounds showed dose-responsive loss of cell viability with IC50 values in nanomolar to low micromolar range (Figure 2.1A) while neither immortalized hepatocellular carcinoma line Huh7 and dispersed definitive endoderm obtained at an earlier development stage exhibited overt cytotoxicity (Figure. 2.6).

CellProfiler 4.2.0 was used to segment and extract 845 features per cell to generate a cell-by-feature matrix characterizing drug-induced perturbation of single-cells in response to the 12 hepatotoxic drugs. The dimensionality of the feature vector was reduced to 2-dimensions using the UMAP method[155] and hierarchical density-based clustering was performed with HDBScan[156] to characterize and cluster drug treatments by their resulting phenotypic perturbation. We observe three distinct clusters within this embedding (Figure 2.1B, Figure 2.7). Cluster α consists largely of allopurinol, tamoxifen, and thioguanine-treated cells. Cluster β largely contains cells treated with nucleotide/nucleoside analogs and consists mainly of cells treated with propylthiouracil, and to a lesser extent, stavudine, and thioguanine-treated cells. Lastly, Cluster γ contains a majority of cells treated with allopurinol and tamoxifen as in Cluster β, but with a major presence of nevirapine and rifampin which are thought to cause DILI through CYP450 modulation.[157] With other compounds, less pronounced clustering was observed (Figure 2.7).

2.3.2 Biochemical, phenotypic, and transcriptomic analysis of HLOs in an Organ-on-a-Chip System - iPSC Liver Chips

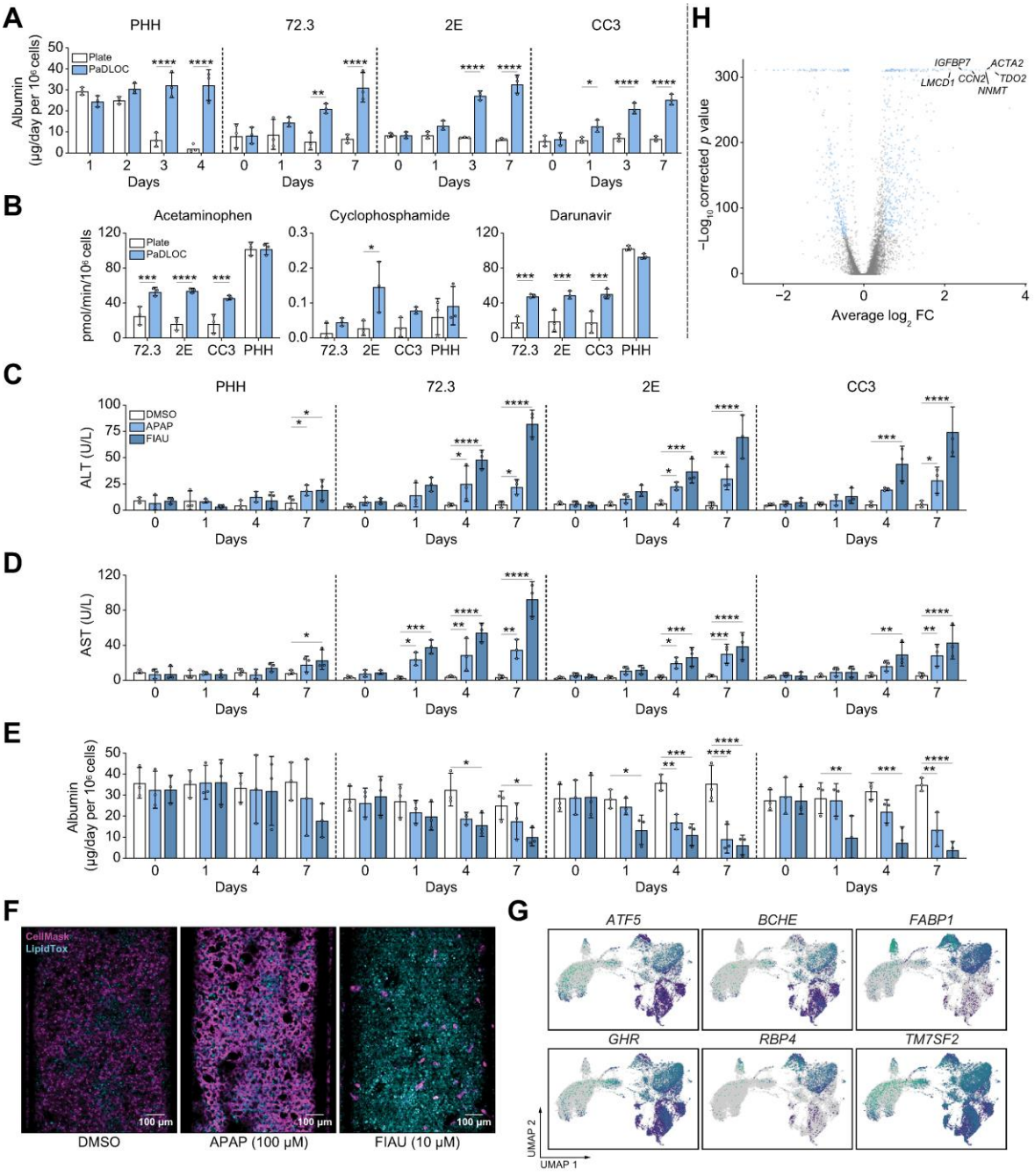

Figure 2.2 Development of a HLO-based Liver Chip. HLOs developed from iPSC lines 72.3, 2E, and CC3 are disrupted into single-cell suspension and cultured into patient-derived liver organoids on chip (PaDLOCs) and compared against intact organoids on 12-well plates. (A) Albumin released in PaDLOCs is identical to that of plate HLOs at day 0 but increases over 7 days (day 21-28 of differentiation). (B) PaDLOCs turnover CYP1A, 2B, and 3A family substrates acetaminophen, cyclophosphamide, and darunavir at increased rate compared to plate HLOs. (C) Cells are treated with DMSO control and known hepatotoxins APAP (100 µM) and FIAU (1 µM). PaDLOCs

demonstrated both ALT (D) and AST release and (E) albumin production diminishment across 7 days. Bars and plot points represent mean ± SD (n=3 PaDLOC chips and n=3 plate HLO wells). Statistical significance was calculated using ANOVA with multiple comparison Dunnett's test. *, **, ***, and **** denote P values of less than 0.05, 0.01, 0.001, and 0.0001 respectively. (F) Confocal images of PaDLOCs at day 7 of treatment stained with CellMask Orange (magenta) and LipidTOX Deep Red (cyan). Images shown are scaled to identical intensity ranges. (G) UMAP clustering of 72.3-derived PaDLOCs highlighting a selection of liver specific genes. Each point represents one cell. Gray values represent no detected expression. (H) Volcano plot comparing gene differential expression between 72.3-derived PaDLOC and HLOs with genes most upregulated in PaDLOC highlighted (>0 designates higher expression in PaDLOCs).

Patient-derived liver-on-chips (PaDLOC) were developed by dispersing HLOs into a single-cell suspension seeded in both upper and lower compartments of a dual-compartment microfluidic S1 chip (Emulate Bio) and cultured for an additional 7 days. The dual-compartment microfluidic S1 chip was previously used for long-term culture and maintenance of primary hepatocytes.[158] Primary hepatocytes on this system were shown to respond to DILI-causing compounds and recapitulate species-specific toxicity over the current preclinical standard models.[156]

While intact HLOs cultured on plates produce under 10 μg/mL albumin per day per 106 cells with slight diminishment after 7 days of culture, PaDLOCs show an increased albumin production rate of 20-30 ug/mL per day per 106 cells (Figure 2.2A). This is comparable to albumin production by PHHs (Gibco, Lot HU8305) on this system and with previous findings while PHHs in plates quickly lost albumin production after few days in culture.[157] PaDLOCs also express CYP450s 1A1, 2D6, and 3A4 at 3-5 fold higher levels as compared to intact HLOs (Figure 2.8). Increased CYP expression was also observed by metabolic turnover, as PaDLOCs metabolized acetaminophen (APAP), cyclophosphamide, and darunavir at increased rates compared to plate-cultured intact HLOs (Figure 2.2B), albeit at slightly lower rates than PHHs.

To confirm the presence of hepatocytes in PaDLOCs and compare the transcriptomic changes imparted by the chip system, we performed scRNAseq of iPSC 72.3 derived HLO cells using the Illumina NovaSeq platform. Single-cell analysis was performed for comparisons of

culture conditions (Figure 2.2G). Differential expression analysis between all cells of HLOs and PaDLOCs (Figured 2.2H) showed an increase of liver proliferation biomarkers TGFBI (collagen binding) and CCN2 expression (cell adhesion) in PaDLOCs.[159] Increased expression of hepatocyte-marker TDO2, commonly correlated with increased CYPs 1A1 and 1A2[160] and ACTA2, a marker for activated stellate cells[161], were observed. Other liver-specific markers demonstrating increased expression in PaDLOCs include NNMT[162], and IGFBP7.[163] Enrichment analysis suggests upregulation of cell structural components, cytoskeleton organization, and increase in inflammatory response elements (Figure 2.11).

2.3.3 iPSC liver chips for DILI risk prediction

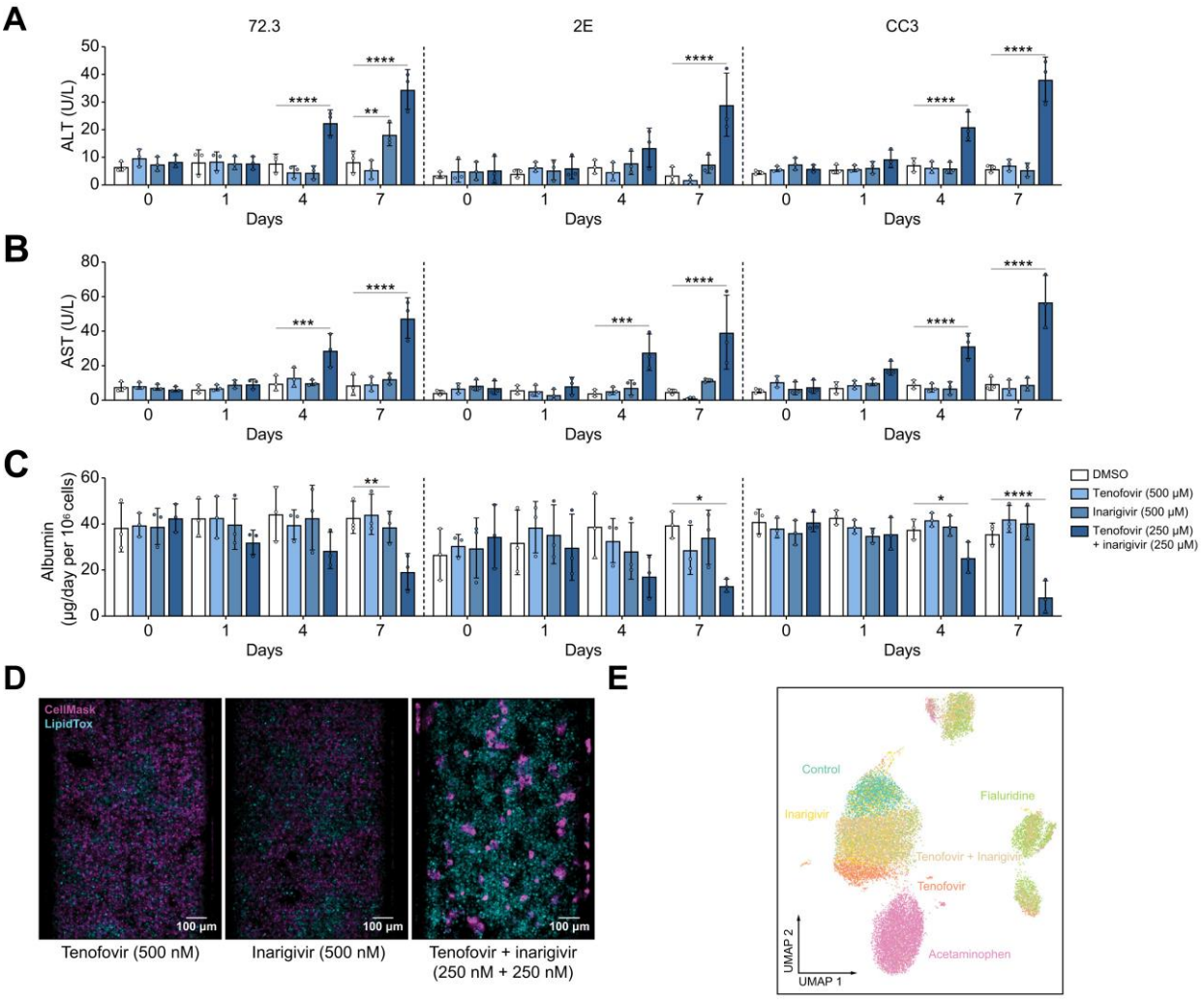

Figure 2.3 Assessment of known DILI-causing drug combination: tenofovi-inarigivir. (A) ALT, (B) AST, (C) and albumin released by 72,3, 2E, and CC3 PaDLOCs over 7 days of treatment with tenofovir (500 nM), inarigivir soproxil (500 nM), and tenofovir-xf inarigivir combination (250 + 250 nM) (n=3 chips per condition). Plot points represent mean ± SD. Statistical significance was calculated using ANOVA with multiple comparison Dunnett's test. *, **, ***, and **** denote P values of less than 0.05, 0.01, 0.001, and 0.0001 respectively. (D) PaDLOCs treated with DMSO control, individual agents, combinations, APAP, and FIAU were stained with Hoechst 33342, CellMask Orange, and LipidTOX Deep Red. Images shown are scaled to identical intensity ranges. (E) CellProfiler extracted cell-level features were embedded into UMAP demonstrating morphological clustering. Plot points represent individual cells。

Serum biomarkers for DILI include elevated ALT and AST[164] and diminished production of albumin.[165] These biomarkers correspond to hepatocellular injury. APAP and filauridine (FIAU) were chosen as compounds with known intrinsic hepatotoxicity with differing mechanisms of action. APAP is metabolized by CYP450-mediated oxidation to NAPQI which exerts hepatotoxicity via the formation of covalent liver protein adducts at cysteine residues as 3-

(cystein-S-yl)-APAP.[166,167] In contrast, FIAU causes hepatotoxicity by stimulating ectopic lipid accumulation and as a mitochondrial toxin. FIAU infamously passed pre-clinical assays but still resulted in overt patient hepatotoxicity.[168,169] For all PaDLOC lines, treatment with 100 μM of APAP increased ALT from a basal level of less than 10 U/L at day 0 to peaks of around 20-30 U/L (Figure 2.2C-D), while treatment with 10 μM FIAU drastically increased both ALT and AST to over 80 U/L. Additionally, albumin production, a guiding biomarker for the diagnosis of DILI severity,[165] was stable in DMSO-treated PaDLOCs while its production was diminished in both APAP and FIAU-treated PaDLOCs. These observations of ALT/AST release and reduced albumin production were not significant in PHH PaDLOCs (Figure 2.2E).

The heterogeneity of DILI presents a challenge for DILI-risk prediction for novel therapeutics. For example, in patients, DILI from APAP and FIAU manifest differently due to differing mechanisms of action. APAP has been reported to cause hepatic necrosis[170] whereas FIAU causes diffuse microvesicular steatosis with retention of hepatic architecture.[171] PaDLOCs treated with APAP and FIAU at 100 μM and 10 μM, respectively, were stained for nuclei/cell regions and lipid droplets to test if PaDLOCs can capture this heterogeneity. Confocal images demonstrate APAP-treated PaDLOCs showed a patchy loss of cell mask and shriveling of cells with no increased lipid accumulation as compared to control (Figure 2.2F). In contrast, FIAU treated PaDLOCs showed high lipid content and a reduction of CellMask staining.

2.3.4 Modeling Hepatotoxicity of Tenofovir and Inarigivir Combinations

Cells in 384-well plates were treated with a 16-point dose range of tenofovir, inarigivir soproxil, and tenofovir -inarigivr in combination. After 120 hrs of treatment confocal images were taken for each treatment condition (n = 4 wells) stained to delineate nuclei/cell regions. Striking, while we observed negligible cytotoxicity for the monotherapies up to concentration of

100 μM, we observed 100% loss of cell viability in the tenofovir-inarigivir combination (Figure 2.9A, IC50 = 56.9).

In PaDLOCs, tenofovir and inarigivir monotherapy at a concentration near their reported C_{max} (500 nM)[172,173] did not increase ALT or AST release after treatment and no morphological deviation from DMSO-treated control (Figure 2.3). However, the combination of tenofovir and inarigivir increased ALT starting at day 4 to 15-25 U/L, and to 25-35 at day 7 and AST to 20-30 U/L at day 4 and 40-50 U/L at day 7 (Figure 2.3A-B). Combination treatments also resulted in a decrease in albumin production while no effect was observed in the single-agent treatments across the 7 days (Figure 2.3C). PaDLOCs from iPSC 72.3 did however demonstrate slight increase in ALT release only at day 7 of treatment.

Visually, PaDLOCs treated with both combinations exhibited a similar phenotype to FIAU-treated controls with regional loss of CellMask staining and high lipid accumulation (Figure 2.3D). These features were measured from confocal images and reduced via UMAP into a 2-dimensional projection (Figure 2.3E). We note tenofovir-inarigivir-treated cells clustering with those FIAU-treated, while tenofovir and inarigivir single-agent treatments clustered with DMSO control. APAP treated cells exhibited a phenotype unlike either of the other groups and resulted in their unique cluster.

2.3.5 Transcriptomic analysis of Tenofovir-Inarigivir, FIAU, APAP treated PaDLOCs

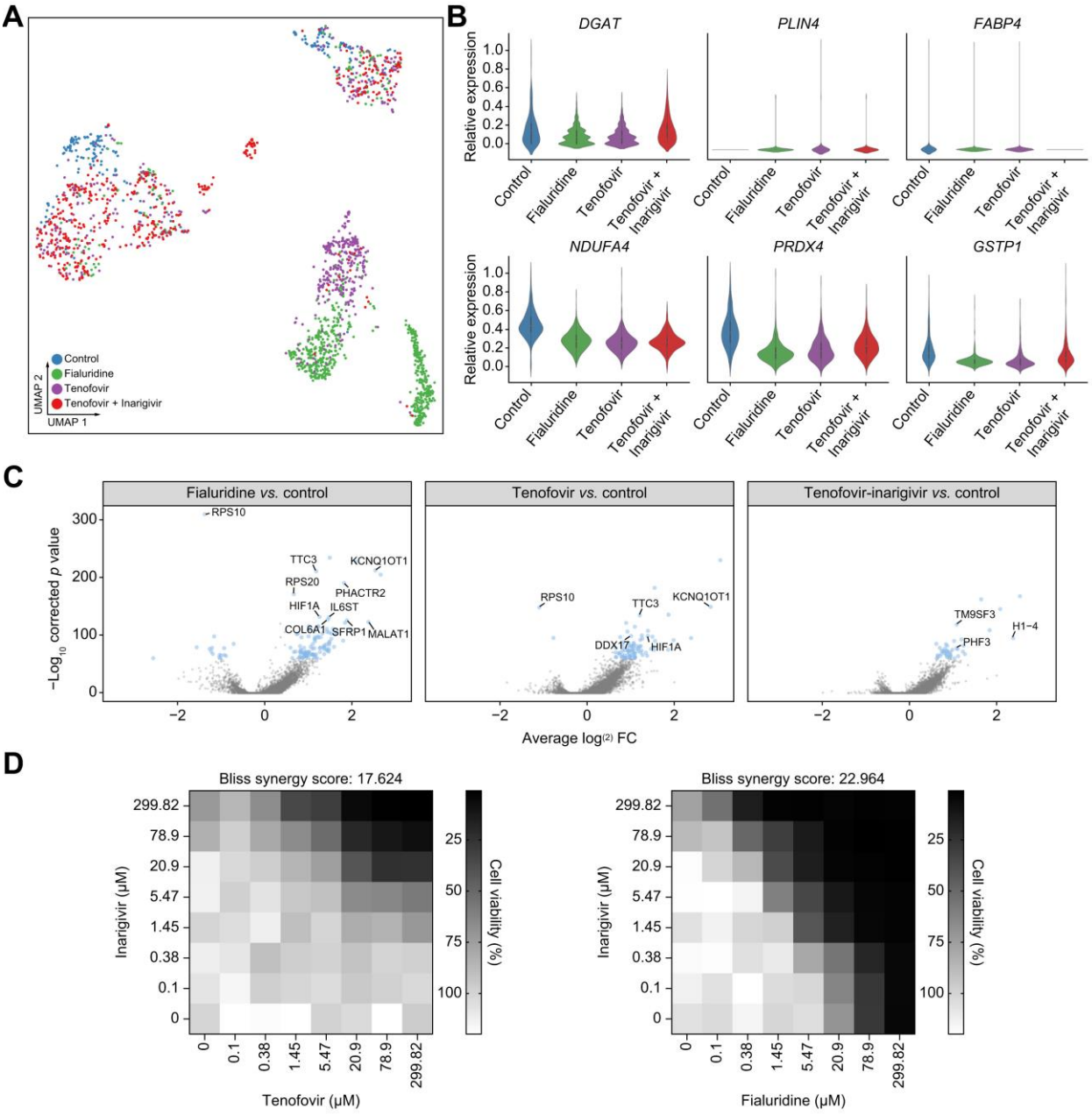

Figure 2.4 Single Cell Transcriptomics of treated PaDLOCs. (A) Hepatocytes across treatments are identified and subset through marker expression and embedded into a UMAP to visualize similarities between treatments. Plot points represent individual cells. (B) Relative expression of DGAT1, PLIN4, FABP4, NDUFA4, PRDX4, and GSTP1 in vehicle control, fialuridine, tenofovir, and tenofovir-inarigivir treated PaDLOCs. (C) Volcano plots highlighting significant differential expression between control and drug treatments (>0 designates higher expression in treatment). (D) In 384-well cultures, 2-dimensional dose response assays show inarigivir and both tenofovir and fialuridine are synergistic with Bliss scores of 17.624 and 22.964, respectively, as calculated by SynergyFinder 2.0.

scRNA-seq was performed on drug-treated and control PaDLOCs on the Illumina NovaSeq platform. The concentration and duration of treatment were optimized using

phenotypic endpoints to capture intermediate phenotypes rather than late-stage cell death. We evaluated DMSO-treated controls, fialuridine (10 μM), tenofovir (500 nM), and tenofovir-inarigivir (250 + 250 nM) combination. Single-cell data was subset to the hepatocyte population based on known hepatocyte markers as listed in Figure 2.2G. Although tenofovir-inarigivir-induced hepatotoxicity has similar clinical features to that of fialuridine, our comparisons suggest a greater transcriptomic similarity between tenofovir monotherapy and fialuridine. First, UMAP re-embedding of the hepatocytes shows close clustering between fialuridine and tenofovir treatments (Figure 2.4A). Volcano plots (Figure 2.4C) show that both conditions, compared to control, result in overexpression of KCNQ10T1, upregulation of which was previously shown to diminish DILI effect[174] and suppressed expression of RPS10 .

Hepatocyte-specific differential expression analysis shows correlative transcriptomic perturbation by fialuridine and tenofovir. Fatty acid, triglyceride, and lipid storage markers (Figure 2.4B) were of particular interest due to observations through confocal microscopy (Figure 2.3B). DGAT1, involved in triglyceride synthesis and storage[175], is downregulated under both fialuridine and tenofovir treatment when expression under tenofovir-inarigivir combination treatment matches that of vehicle control. PLIN4, thought to aid in lipid droplet accumulation in the liver[176], is not detected in the vehicle control but increased in all other conditions. FABP4 is expressed consistently in all but the combination treatment, conflicting with previous evidence that FABP4 is overexpressed in liver injury due to hepatocellular carcinoma.[177–179] However, other reports have shown that FABP4 knockdown results in greater adiposity in mice.[180] Across all treatments, we observe diminishment of NDUFA4 as compared to control.[181] We also observed decreased expression of PRDX4 in all treatments, and GSTP1 in fialuridine and tenofovir single treatments, indicators of oxidative stress.[182,183]

As we observed similar transcriptomic perturbations between fialuridine and tenofovir treatments, we assessed whether fialuridine-inarigivir combination treatments showed synergistic toxicity similar to tenofovir-inarigivir treatments. Interestingly, in 384-well dispersed HLO assays, both tenofovir-inarigivir and fialuridine/inarigivir combinatory treatment likely result in synergistic toxicity with calculated Bliss synergy scores of 17.624 and 22.964, respectively (Figure 2.4D).

2.4 Discussion

HLOs both from our findings and other reports[80] show promise as a viable in vitro model for DILI risk prediction. They are amenable to both a high-throughput screening and adaptation to PaDLOCs to further enhance their organotypic function. Compared to PHHs, HLOs enable large-scale and high throughput DILI risk assessment due to their relative scalability and consistency. Their application in 384-well format serves as basis for an early-stage preclinical assessment of novel drugs. PaDLOCs exhibit physiological similarities to human liver including: 1) production of cell types from the same host genetics including hepatocyte-like and stellate-like cells, 2) albumin production, and 3) cytochrome P450 expression.

HLOs as a dispersed monolayer can minimize well to well variability and obtain clear single-cell resolution images. This enables high-content screening, Cell Painting[93], and morphological cell profiling. As we demonstrated, these multivariate outputs cluster drugs by their phenotypic perturbation to infer similar mechanisms of action and compare to other compounds. Multivariate analysis also enables cumulative hepatotoxic scores unable to be defined by individual endpoints. For example, FIAU treatment at sub-cytotoxic concentrations results in multidimensional perturbation of cells including diminished mitochondrial mass and

lipid accumulation (Figure 2.9 B-C). Machine learning-based multivariate analysis can combine multiple features into a robust prediction score.

While high-throughput screening with dispersed HLOs in 384-well plates allows rapid expansion for large screening efforts across multiple iPSC lines, they suffer from lower CYP450 expression and lack of crucial hepatocyte function.[79] Although superior to hepatocellular carcinoma cell lines which often do not demonstrate hepatotoxicity, some observed IC50 values for HLOs loss of cell viability are higher than achievable in vivo Cmax. For example, the reported IC50 for nevirapine in 72.3 derived HLOs is over double that of reported Cmax in patients.[184] PaDLOCs, likely due to more adequate drug metabolism and mixture of parenchymal and non-parenchymal cell types, seem to respond to many drugs at in vivo concentrations.

In our studies, fialuridine and tenofovir-inarigivir were administered at Cmax concentrations and responded with clear hepatotoxicity across multiple cell lines. Hepatotoxicity of both therapies was not detected until clinical trials nor detected in the 384-well platform until higher concentrations. In APAP treatments, previous PHH studies on the Emulate system used 30-fold higher APAP concentrations to achieve a hepatotoxic effect[182], due to reliance of APAP turnover to NAPQI by CYP2E1.[185] Despite greater CYP expression and metabolic turnover, these effects are not observed at the same concentrations in PHHs suggesting also the necessity of the diverse cell types found in intact HLOs and PaDLOCs. Lastly, in patients, APAP and FIAU damaged liver histology present as hepatic necrosis[170] and diffuse microvesicular steatosis with retention of hepatic architecture,[171] respectively. Our confocal images show APAP-treated PaDLOCs with patchy loss of cell mass while FIAU-treatment results in over accumulation of lipids, seemingly mimicking their presentation in patient histology.

The integration of scRNA-seq, shown here as a proof-of-concept for liver chip systems, provides detailed predictive power for synergistic DILI. Herein, our unified multi-omics platform supported with transcriptomics data predicted FIAU-inarigivir synergy given known tenofovir-inarigivir synergy in a complex PaDLOC system, which was then confirmed in 2-dimensional dose response in the higher throughput platform. Although further optimizations are necessary, PaDLOCs show promise as an informative model for DILI allowing multi-omic endpoints. As they are iPSC-based, and iPSCs can be reprogrammed from patient cells acquired non-invasively (e.g. PBMCs)[186] or even hESCs (Figure 2.10), this platform can be expanded to encompass patient genetic diversity. An adequate biobank of PaDLOCs would be ideal to benchmark compounds before clinical trials and mitigate rare hepatotoxic events. Future studies will focus on developing a biobank of complex HLO co-cultures established from well phenotyped and genotyped idiosyncratic DILI patients of varying age and ethnicity thereby concentrating genetics to a screenable number of patient lines as a predictive platform that may improve DILI risk assessment.

2.5 Acknowledgements

The authors would like to thank Emulate Inc. for assistance with experimental design. We thank Kevin Jan at Yokogawa for microscopy support. We thank Teresa O'Meara for writing assistance and proofreading, and Carmen Mirabelli, Chung Owyang, and Bishr Omary for thoughtful advice. We thank Andrew Tidball, Wei Niu, and Xiaotian (Tracy) Qiao for gifting the iPSC lines and providing cell culture support. Lastly, we thank Yihao Zhuang for assistance with acquiring LC/MS data.

2.6 Methods

2.6.1 Human liver organoid culture and dispersion

Human iPSC line 72.3 was obtained from Cincinnati Children's Hospital Medical Center[150] and iPSC lines 2E[151] and CC3[152] were gifted by the University of Michigan Human Stem Cell and Gene Editing Core. iPSCs were differentiated into HLOs based on a previously described protocol.[78,79] In brief, iPSCs were grown to 90% confluency on growth factor reduced Matrigel (Corning, 354230) coated 6-well plates (ThermoScientific, 140675). Cells were then treated with Activin A (R&D Biosystems, 338-AC) for 3 days and FGF4 (purified in house[187]) for 3 additional days to form definitive endoderm spheroids. Spheroids were embedded in 75 μL Matrigel (Corning, 354234) droplets in 24 well plates (ThermoScientific, 1142475) and treated with retinoic acid for 4 days followed by hepatocyte growth media (Hepatocyte Culture Medium BulletKit (Lonza, CC-3198) supplemented with 10 ng/mL hepatocyte growth factor (PeproTech, 100-39), 20 ng/mL oncostatin M (R&D Systems, 295OM050), and 0.1 μM dexamethasone (Millipore Sigma, D4902)) for 12 days.

HLOs were then taken out of Matrigel by treatment with dispase (0.2 mg/mL) for 10 minutes at 37 ^{o}C followed by washing with DMEM/F12 (ThermoScientific, 11320033) and centrifugation at 300 x g for 3 minutes to pellet. To achieve a single cell suspension, cells were treated with trypsin (0.25%) (Invitrogen, 25200056) and incubated at 37 ^{o}C for 10 minutes, mechanically dissociated by pipetting, and incubated until dissociation for up to an additional 10 minutes. Trypsin was quenched with 100% FBS (Corning, 35-010-CV) and washed 3 times with DMEM/F12 followed by resuspension in HCM.

2.6.2 PaDLOC Culture and Compound Treatment

Dispersed HLO cells were transferred to the Chip S1TM based on the co-culture Liver-Chip Culture Protocol as described by Emulate Bio.[188] In brief, both channels were coated with an extracellular matrix consisting of collagen I (100 µg/mL) (Corning, 354249) and fibronectin (25 µg/mL) (ThermoScientific, 33010018) at 4 ºC overnight followed by 1 hr at 37 ºC. Dispersed HLOs were concentrated to a density of 4 x 106 cells/mL. 50 µL of cell suspension was quickly pipetted into the bottom channel and the chip immediately flipped over to allow attachment to the membrane to allow even dispersion and cultured static (no media flow) at 37 ºC for 8 hrs for attachment to the semi-permeable membrane. Next, 30 µL of cell suspension was seeded into the top channel and again left to attach for 8 hrs at 37 ºC. Both channels were then washed with hepatocyte growth media containing hepatocyte growth factor, oncostatin M, dexamethasone de-gassed with a 0.45 µm Steriflip-HV Sterile Centrifuge Tube Top Filter Unit (MilliporeSigma, SE1M003M00).

Each seeded Chip S1 was then attached to a respective PodTM Portable Module. Loaded Pods were placed into the ZoëTM Culture Module at 37 ºC. All chips then underwent a regulate cycle followed by a constant flow rate of 30 µL/hr of the reservoir's media for each of both channels modulated by an OrbTM Hub Module. Media outflow collected in respective reservoirs was obtained for ALT, AST, and albumin measurement. Fresh de-gassed hepatocyte growth media was added into the inlet reservoirs every 2 days. Cells were cultured with flow for 7 days before treatment.

After 7 days, residual hepatocyte growth media was aspirated and replaced with hepatocyte growth media containing either 0.1% DMSO, APAP (100 µM), FIAU (1 µM), tenofovir (500 nM), inarigivir soproxil (500 nM), or tenofovir and inarigivir soproxil (250 nM

and 250 nM). The flow rate was maintained at a constant rate for an additional 7 days and outflow media was collected at days 1, 4, and 7 post-treatment.

2.6.3 Dispersed 384-well HLO culture and drug delivery

Dispersed HLOs were seeded in collagen type 1-coated CellCarrier-384 Ultra Microplates (PerkinElmer, 6057308) at a seeding density of 8,000 cells/well in hepatocyte growth media. Cells were left to adhere and culture for 48 hrs before treatment with compounds. For screening, compounds were dispensed in 10-point dose-response from 2 nM to 500 μM using an HP D300e Digital Dispenser. For tenofovir-inarigivir synergy assessment, tenofovir, inarigivir sorpoxil, and in combination were dispensed in triplicate with 12-point dose-response curves in 1/3 dilutions starting with a high of 500 μM. Cells were then incubated for 120-hours before fixation and staining.

2.6.4 Plate and Organoid Fixation and Staining

Plates were fixed with 4% paraformaldehyde for 15 minutes followed by permeabilization by 0.1% Triton X-100 (MP Biomedicals, 194854) for 15 minutes (50 μL per well). Cells were then blocked by a buffer containing 5% BSA (MilliporeSigma, A9647) and 0.01% Tween (FisherScientific, BP337-100) in PBS for 1 hour (50 μL per well). At this point, the protocol deviated based on necessary stains.

For 384-well hepatotoxicity assays, plates were stained with Hoechst 33342, MitoView Green (Biotium, 70054), HCS CellMask Orange (ThermoFisher Scientific, H32713), and HCS LipidTox Deep Red (ThermoFisher Scientific, H34477). PaDLOCs were stained with Hoechst 33342, HCS CellMask Orange, and HCS LipidTox Deep Red. Stains were diluted based on

manufacturer's recommendations in blocking buffer and applied to cells (25 μL per well), washed 3 times with PBS (50 μL per well).

For 384-well biomarker immunofluorescence assays, cells were stained with Hoechst 33342 (ThermoFisher Scientific, H3570), HNF4A (ThermoFisher Scientific, MA5-14891), α-SMA (Abcam, ab21027), and CD68 (Abcam, ab53444). Antibodies were diluted at 1:500 in blocking buffer and added to each well and incubated overnight at 4 ^{o}C (25 μL per well). Antibody solution was then washed 3 times with PBS (50 μL per well) and stained with a secondary solution. For immunofluorescence containing rat, rabbit goat, primary antibodies, the secondary solution contained anti-rat Alexa Fluor 488, anti-rabbit Alexa Fluor 555, and anti-mouse Alexa Fluor 647 Highly Cross-Adsorbed Secondary Antibodies (ThermoFisher Scientific, A21208, A31572, A31571). Plates were incubated for 1 hour at room temperature followed by another three PBS washes before imaging.

2.6.5 Image Acquisition

All images were acquired with a Yokogawa CQ1 Benchtop High-Content Screening System. 384-well plates were imaged with 1μm Z-spacing and 15 μm depth at 20X (Olympus UCPLFLN20X). PaDLOCs were imaged with 1 μm sections through 100 μm depth also at 20X. Cell Morphological Profiling and Data Analysis

Individual nuclei were first delineated in the Hoechst 33342 stained channel using Cellpose 2.0.[96] Multi-channel fluorescence images were then analyzed with CellProfiler 4.2.0. Whole cell was delineated using nuclei as seed objects and dilation to the extent of the cell boundary which enabled measurements of fluorescent intensity, intensity distribution, texture, size, and shape from the respective regions in each fluorescent channel.

The resulting data set included hundreds of measurements on a per-cell level with necessary cell-level metadata. Cell viability across compound dose-range was obtained based on the number of identified cells per condition with DMSO vehicle-treated control as the 100% viability reference. Uniform Manifold Approximation and Projection (UMAP) embedding was done with the Python umap-learn package. Measurements for each feature were centered at zero and scaled with Z-score=1. Features with low variance were omitted.[155] Bliss synergy scores were calculated using SynergyFinder 2.0.[189]

2.6.6 Cell Type Confirmation by Marker Positivity

Based on visual inspection, cells positive for respective markers were selected to obtain an estimated intensity value for positivity in relation to cell compartment (nuclear for HNF4A, cytoplasmic for α-SMA and CD68) in CellProfiler Analyst 3.0[95] and set as thresholds for cell type identification. Cells with no expression of these three markers were classified as "other".

2.6.7 Single-Cell Transcriptomics

HLOs were dispersed as described previously and cells were removed from control and treated PaDLOCs with trypsin (0.25%) (Invitrogen, 25200056) followed by FBS inactivation and PBS washing. Cells were kept on ice, confirmed to have >85% cell viability, and sent to the University of Michigan Advanced Genomics Core to prepare single cell libraries on the 10x Chromium with a cell capture target of 5,000 cells. Sequencing was performed by the core on a NovaSeq 6000 with a target of 100,000 reads per cell.

Each sample generated between 440 and 860 million barcoded reads corresponding. Transcripts were mapped to the GRCh38 2020-A (GENCODE v32/Ensembl 98) (July 7th, 2020) reference transcriptome[190] using 10x Genomics Cell Ranger 5.0.1,[191] where between 45% and

58% of reads per sample confidently map to the transcriptome, yielding between 500 and 4,700 median genes per cell. As a quality filter, genes were excluded if they were only detected in 5 or fewer cells, and cells were excluded if over 30% of reads were mitochondrial or if they had fewer than 10,000 total reads. Given that hepatocytes may be binucleated,[192] we did not remove doublets.

To estimate differential expression, we first correct for over-dispersion using sctransform v2[193] with Seurat v4[194] which fits a robust negative binomial model for the per-gene variance by the expression mean. We then used DESeq2 to compute the average log fold-change and adjusted p-value for each gene between cells under different conditions.[195]

2.6.8 UMAP Embedding

To visualize and cluster cells with distinct phenotypes, we used UMAP non-linear dimensionality reduction.[196] For scRNA-seq data, UMAP embeddings were done in monocle3.[197] Expression values were normalized by dividing by per-cell size factors, adding a pseudo-count of 1, and taking the natural log; reducing the dimensionality with principal component analysis to 100 dimensions; and then applying the UMAP algorithm implemented in uwot[198] using the monocle3 default arguments: similarity="cosine", min_dist=0.1, n_neighbors=15. For CellProfiler morphological data, cell features were normalized (mean=0, stdev=1) and cells were filtered down to n-500 cells for each treatment compound following embedding in umap-learn.[196]

2.6.9 Human Serum Albumin, ALT, and AST Measurements

Media from PaDLOCs outflow or culture plates were obtained. HSA from chip media outflow was measured using an albumin human ELISA Kit (ThermoFisher Scientific, EHALB). 10 uL of media was diluted 100-fold in PBS before incubation on ELISA plate. A standard curve

was made in accordance with kit guidelines and used to determine albumin concentration in all samples. Each sample was assayed in triplicate.

For ALT and AST measurement, 30 uL of media and PBS blanks were dispensed into respective wells in a 96-well assay plate. 300 uL of room temperature ALT/GPT Reagent (Thermo Scientific, TR71121) or AST/GOT Reagent (Thermo Scientific, TR70121) was then dispensed into all wells in the plate and incubated at 37 ^{o}C for 30 seconds before recording absorbance at 340 nm for 3 minutes. Activity of ALT or AST was determined using the following equation:

$$\text{Abs/min} \times \text{Factor}$$

Where Factor is pre-determined for this assay and is 1746, from the manufacturer's manual. Average activity from blanks was subtracted from all other samples. All plates were read with a BioTek Synergy H1 Microplate Reader.

2.6.10 CYP450 Expression Quantification

RNA was purified with the Direct-zol RNA Miniprep (Zymo Research, R2052) and expression was measured using CFX96 Touch Deep Well Real-Time PCR System (BioRaD) and iTaq Universal Probes One-Step Kit (BioRad, 1725141). Primers used were CYP1A1 (ThermoFisher Scientific, Hs01054796_g1), CYP2D6 (Hs04931916_gH), CYP3A4 (Hs00604506_m1), and housekeeping gene GAPDH (ThermoFisher Scientific, Hs02786624_g1). Fold change was calculated using the ΔΔCt method over PaDLOC.

2.6.11 CYP450 Metabolic Turnover

Acetaminophen, cyclophosphamide, and darunavir were chosen as substrates for CYP 1, 2, and 3 families respectively. For this purpose, PaDLOCs at day 7 were taken out of the Zoe

Culture Module. Media in PaDLOCs and plate cultures were replaced with 500 µL media containing a cocktail of the substrates each at 10 µM. 100 µL of media was taken after 1 hour and 2 hours of incubation. Reactions were immediately stopped using 100 µL of cold methanol and centrifuged for 5-minutes at 3,000 RPM and supernatant was collected.

Samples and substrate standards (0.11, 0.33, and 1 uM in media:methanol 50:50) were measured using an Agilent qTOF 6545 LC/MS system with the following parameters: Phenomenex Kinetex 1.7µm Phenyl-Hexyl 100 Å (50 x 2.1 mm) column; 2 µL injection volume; LC gradient, solvent A, 5% acetonitrile and 0.1% formic acid; solvent B, 100% acetonitrile and 0.1% formic acid; 0 min, 0% B; 1 min, 0%B; 7 min, 80% B; flow rate 0.4mL/min; MS, positive ion mode. Quantification was done using Masshunter Workstation by peak area integration from extracted ion chromatograms (EIC) for target masses of 152.0706, 261.0321, and 548.2425 for acetaminophen, cyclophosphamide and darunavir, respectively. Linear regressions were fit in KNIME for each standard vs. peak area and used to determine concentration of all samples.

2.6.12 Dose-Response Curve and Statistical Analysis

Dose-response curves were fitted and IC50 values were determined in GraphPad Prism 9 using the nonlinear regression [inhibitor] vs response method. Statistical significance was calculated using ANOVA with multiple comparison Dunnett's test. *, **, ***, and **** denote P values of less than 0.05, 0.01, 0.001, and 0.0001 respectively

2.7 Supplementary Figures

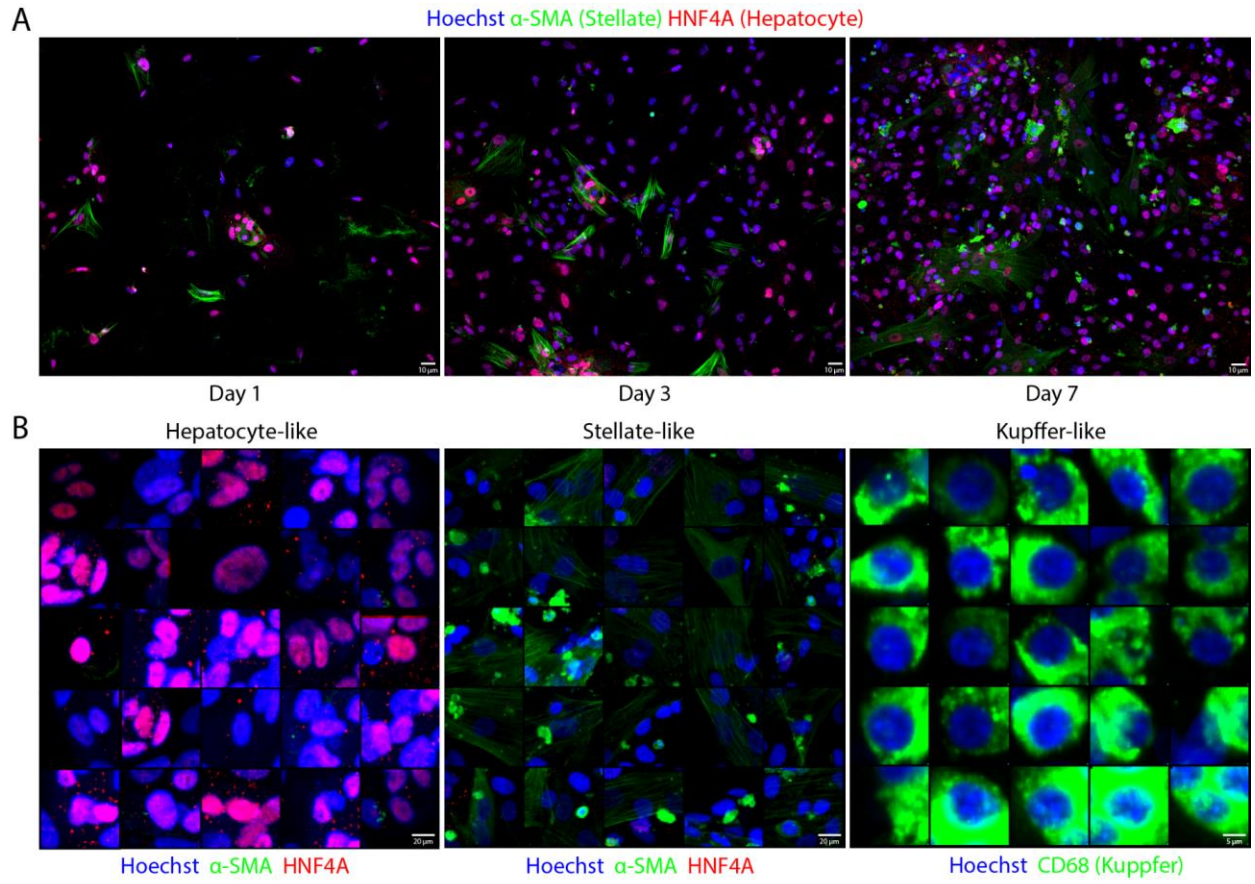

Cell Type (%)	72.3	2E	CC3
Hepatocyte-like	64.56	68.54	75.23
Stellate-like	32.38	26.09	18.72
Kupffer-like	0.12	0.19	0.15
Other	2.93	5.18	5.91

Figure 2.5 (A) Confocal images of 384-well monolayer cultures of dispersed HLOs across 7 days of culture showing retention of cell type specific markers HNF4A (hepatocytes) and α-SMA (stellates). (B) Collage of a subset of identified hepatocyte-like, stellate-like, and kupffer-like cells assembled in CellProfiler Analyst 3.0. (C) UMAP embedding of cell morphological features of 384-well monolayer cultures with the previous stain set. Percentage of hepatocytes, stellates, and Kupffer cells were estimated by marker positivity. Intensity scales of markers were determined from a range of empty background to highest cell intensities.

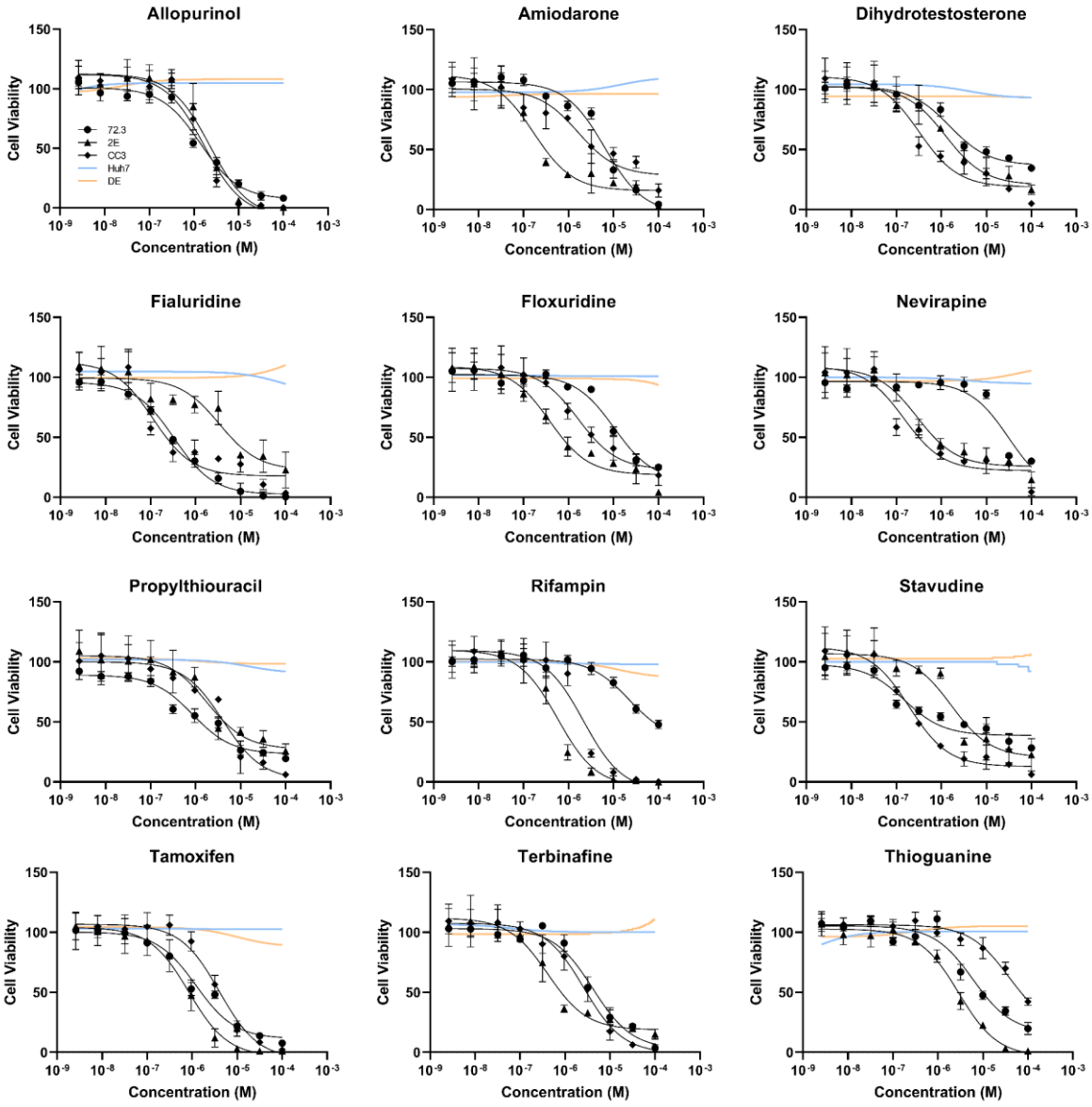

Figure 2.6 Cell viability dose response curves for 12 compounds commonly implicated in DILI against HLOs grown in three independent iPSC lines dispersed into 384-well plates and used to calculate IC50 values shown in Figure 1. Immortalized cell lines and definitive endoderm from earlier in the HLO differentiation process are included as controls.

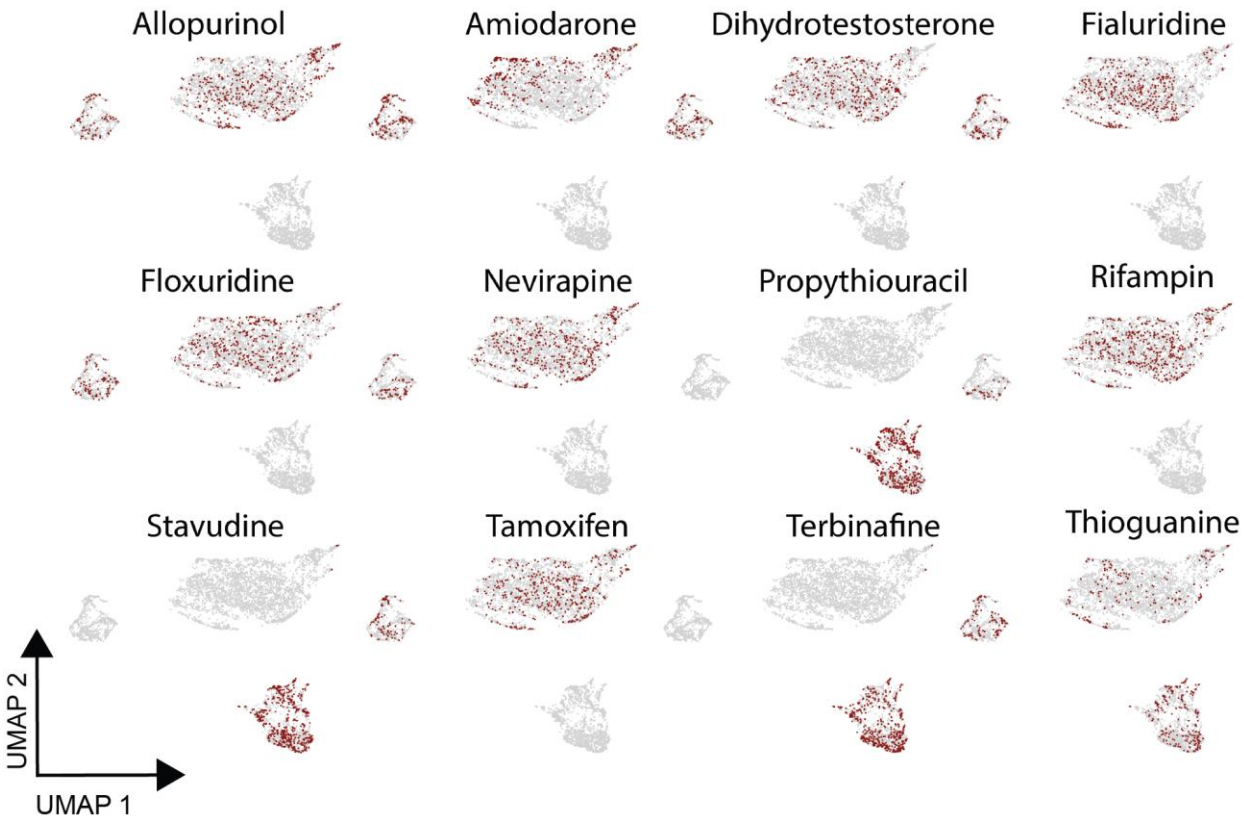

Figure 2.7 HLOs were dispersed into 384-well plates and treated with 10-point dose response for 12 commonly identified DILI compounds. Plates were then fixed and stained with Hoechst 33342, MitoView Green, HCS CellMask Orange, and HCS LipidTox Deep Red. CellProfiler 4.2.0 was used to extract morphological features of cells at their respective IC50 values and embedded into UMAPs with respective compounds highlighted in red.

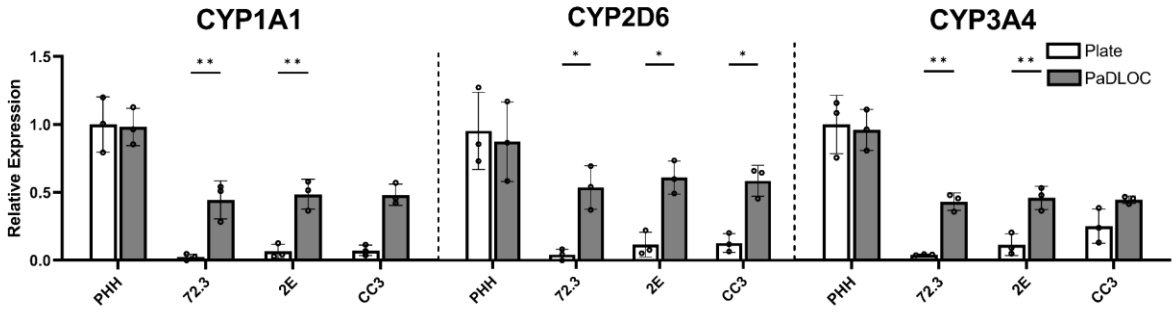

Figure 2.8 CYP 1A1, 2D6, and 3A4 expression of PHHs and HLOs grown from iPSC lines 72.3, 2E and CC3 on plate and after 7 days culture on PaDLOC. Statistical significance was calculated using ANOVA with multiple comparison Dunnett's test. * and ** denote P values of less than 0.05 and 0.01 respectively.

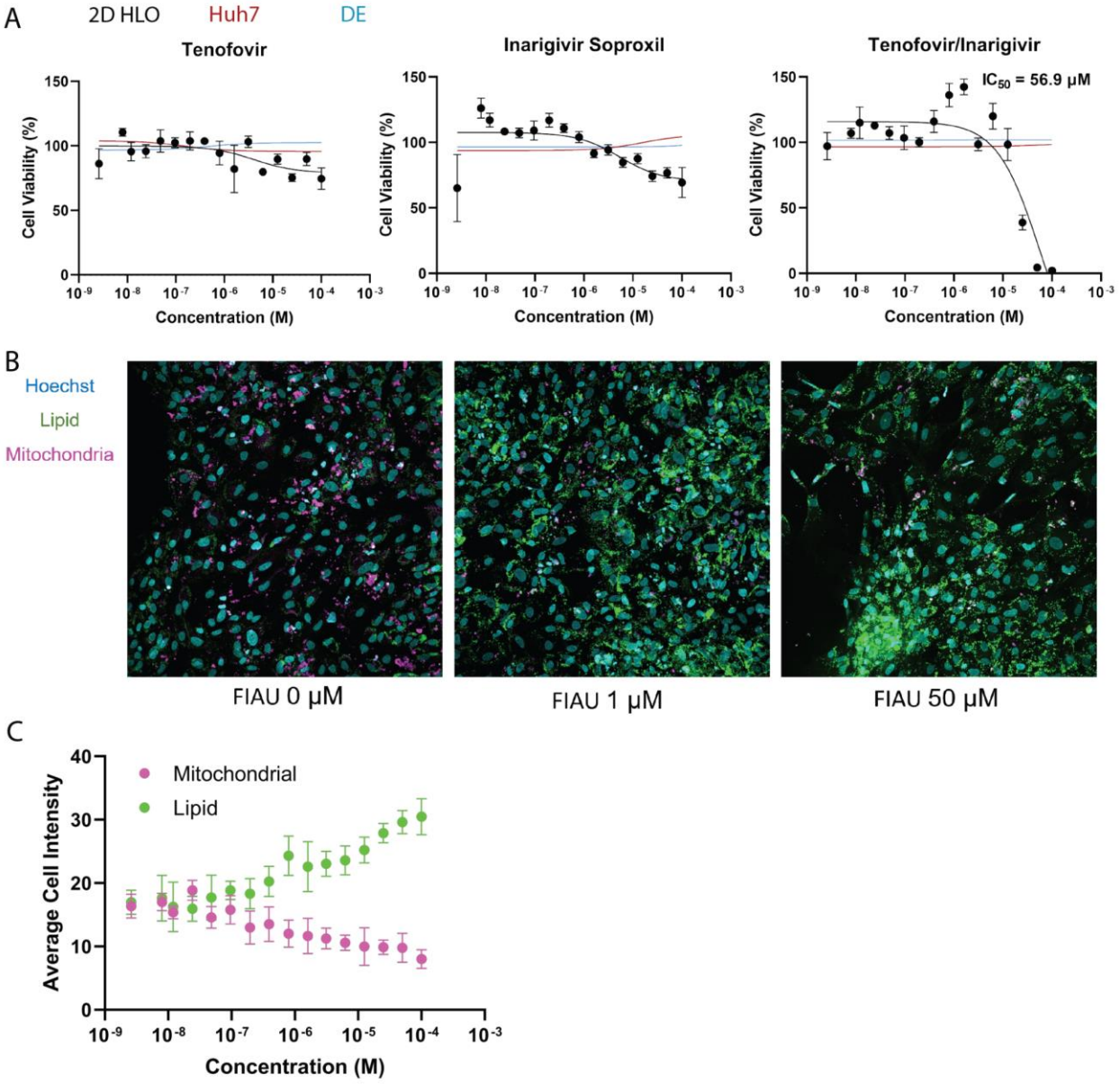

Figure 2.9 (A) Cell viability of 2D 384-well monolayer cultures of dispersed HLOs treated in 16-point dose-response with tenofovir, inarigivir soproxil, or in combination (n=4 per concentration) and measured IC50. (B) Confocal microscopy of FIAU treated 2D monolayers stained for nuclei, lipids, and mitochondria and (C) the per-cell measurement of these features across a dose-range of FIAU. Plot points represent mean ± SD (n=4 per concentration).

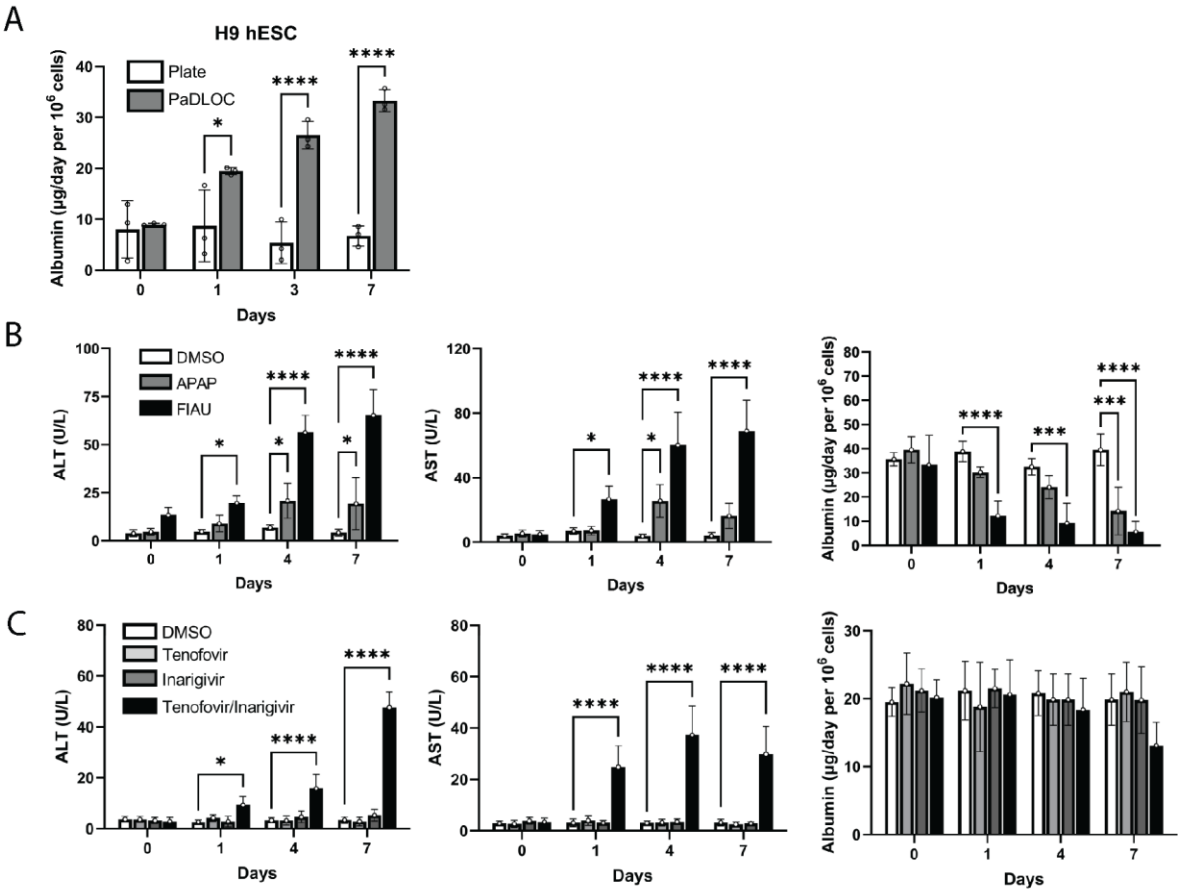

Figure 2.10 H9 human embryonic stem cell derived PaDLOCs show (A) increased albumin production as compared to intact HLOs and (B) consistent ALT, AST, and albumin response to known DILI compounds APAP (100 µM) and FIAU (10 µM). (C) H9 PaDLOCs also respond to inarigivir/tenofovir (250 + 250 µM) induced hepatotoxicity without apparent hepatotoxicity in response to the individual compounds (500 µM).

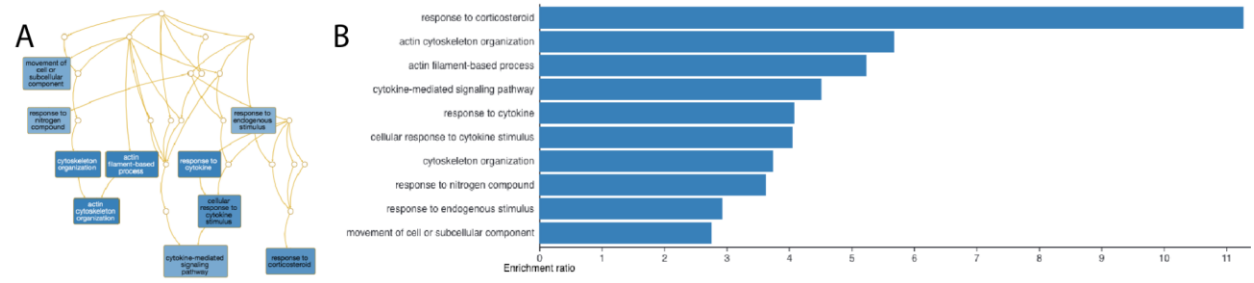

Figure 2.11 Enrichment analysis of scRNAseq data from HLOs vs PaDLOCs generated from iPSC line 72.3

Chapter 3 Engineering a High-Throughput Microfluidic Liver Chip for Chronic DILI

3.1 Summary

Although recent years have seen innovative developments in cell-based assays as alternatives to animal testing there has always been a barrier in throughput and manual labor necessary to build these models. Herein, we describe the engineering of a 16-well microfluidic chip. Each well serves as an independent culture consisting of three compartments allowing for the combining of three separate hydrogel compartments. The developed chip is amenable to existing automation techniques including liquid handling and water-immersion high-content imaging. iPSC-derived human liver organoids (HLOs) were embedded into hydrogel and cultured on this device and assessed for their advancements in liver functionality as compared to previous liver chips. Liver chips were confirmed for hepatocyte and stellate cell-type markers, albumin production, and CYP450 activity at days 7, 14, 21, and 28. Liver chips aged through 21-days were then tested as models for drug-induced liver injury (DILI). All tested chips showed responsiveness to known DILI compounds after an additional 7 days of treatment suggesting long-term viability of this high-throughput liver chip. Additionally, foregut spheroids from prior in the differentiation process were directly embedded into the chips and successfully continued differentiation. Our findings suggest that this 16-well microfluidic chip is viable for long-term maintenance of iPSC-derived HLOs for chronic liver research or drug screening. These chips may also serve as a vessel for direct differentiation of other iPSC-derived organ systems.

3.2 Introduction

Drug-induced liver injury (DILI) represents a significant challenge in both clinical pharmacology and drug development. The liver, being the principal organ for drug metabolism and detoxification, is highly susceptible to damage caused by drug compounds. The ability to predict DILI during the early stages of drug development is crucial to ensure both the efficacy and safety of pharmaceuticals. Recent advancements in *in vitro* microfluidic liver models have allowed for more informed preclinical predictions of hepatotoxicity and are more cost-effective compared to primary human hepatocytes (PHH). Although many of these microfluidic models maintain hepatocyte or iPSC-derived organoids for longer periods of time than traditional 2D PHH assays, there are still difficulties in long-term culture.

Lack of a viable long-term *in vitro* liver models limits existing models in their ability to study chronic DILI and allow for modelling of only the simplest and most direct forms of DILI, that in which a direct hepatotoxic response results in immediate liver damage. However, based on clinical presentations in patients, DILI often occurs weeks or months into a prescription regimen or even weeks after treatment. Clinically, chronic DILI is highly heterogeneous in its presentation and severity. In many cases, liver injury does not self-repair after withdrawal of culprit drugs and may even continue to worsen despite full removal of the drug therapy. Little is known regarding the genetic and environmental factors that contribute to chronic DILI. These phenomena cannot be modelled without long-term hepatocyte models that maintain physiological relevance weeks after seeding or patterning on microfluidic systems. In addition, desired models would need to be rapidly employable across various patient lines to account for genetic diversity. Demand for an effective long-term liver model also exists for other disease states, such as steatotic liver disease (SLD) and viral hepatitis.

Current microfluidic liver models also have limitations in the difficulty to achieve scalability, reproducibility, and consistency. These issues exist as current microfluidic systems are costly and resource-intensive, greatly limiting batch sizes, replicates, and expansive drug dose range testing. In addition, microfluidic device material often consists of polydimethylsiloxane (PDMS) or other highly absorbent materials resulting in artifactual observations in relation to drug effects and kinetics. In an attempt at devising a system that overcomes all these issues, we adapted iPSC-derived human liver organoids (HLOs) to an engineered high-throughput microfluidic system emphasizing on consistency across replicates and minimal inherent drug interactions for robustness when applied to large-scale compound testing. This system was designed for compatibility with standard lab automation allowing for bioassays, immunofluorescence staining, transcriptomics, and high-content confocal imaging. Despite the miniaturized system, liver chips retained the feature of media flow and hydrogel embedding. As an iPSC-derived system, there is potential for this model to be developed on a per-patient basis and to produce cells en masse for large-scale applications.

3.3 Results

3.3.1 Maintenance of Liver Physiology in a High-Throughput Format

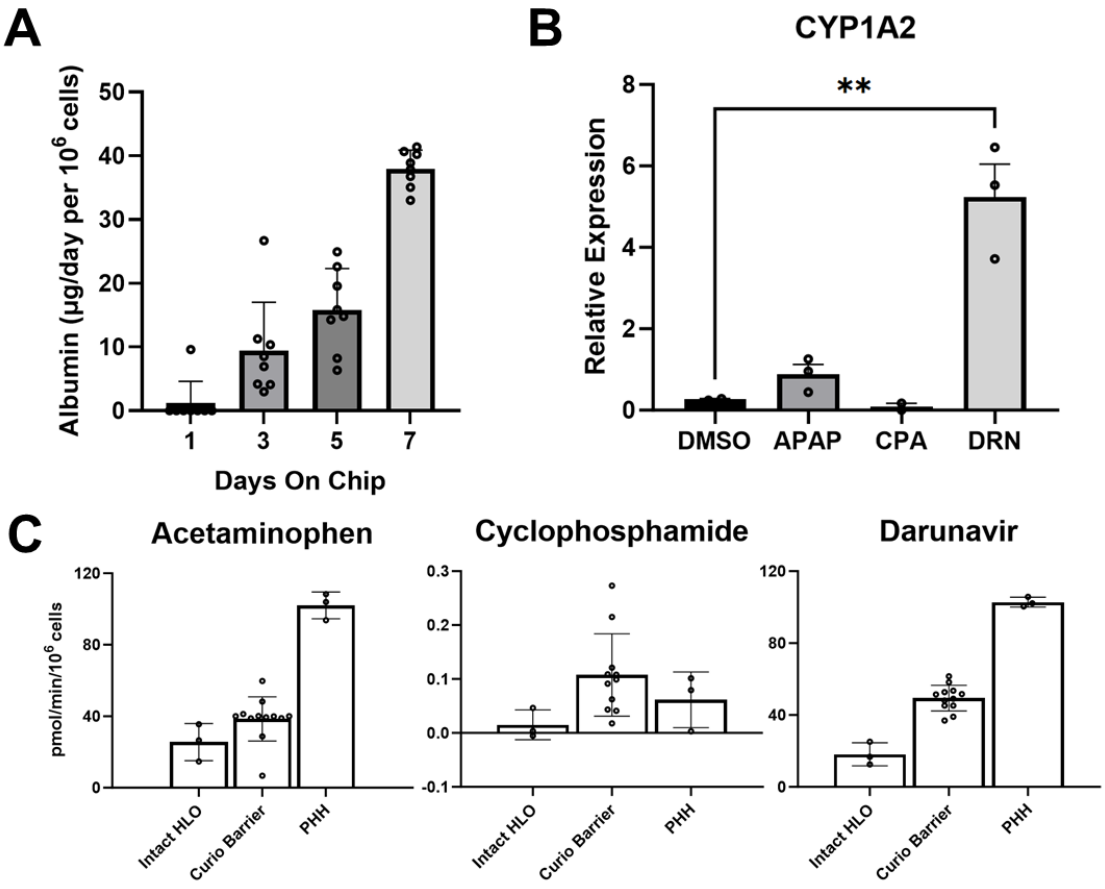

Figure 3.1 Dispersed HLO growth on Curio Barrier chips show A) continuous increase in albumin production across 7 days of culture, B) induction of CYP1A2 by acetaminophen (APAP) and darunavir (DRN), and C) increased CYP450 activity of Curio Barrier liver chips compared to intact embedded HLOs.

Each well contained two media ports and for our purposes of developing HLO liver chips, these ports were leveraged with media gradients to achieve a steady flow rate. With this emphasis on designing a high-throughput format, media collection and maintenance was achieved in Curio-Barriers by standard multichannel/automated liquid handling techniques.

HLOs dispersed and cultured onto Curio-Barrier Chips with consistent media flow continue proliferation and retain hepatocyte and stellate markers across 7 days of culture. Visually, hepatocytes maintain rounded morphology and continued growth into clusters whereas stellates exhibit an extended fibrotic phenotype. Liver chips show a consistent increase in albumin expression across this timeframe (Figure 3.1A) comparable to previous reports of

albumin expressed by hepatocyte-like cells on chip.[78,108] Liver chips on day 7 show CYP 1A, 2D, and 3A family activities based on metabolic turnover of acetaminophen, cyclophosphamide, and darunavir, respectively (Figure 3.1C). While CYP 1A and 3A family activities are comparable to previously developed liver chips, metabolic turnover still shies from liver chips grown with primary human hepatocytes. CYP 2D however showed a drastic performance increase compared to previous HLO liver chips while nearing the enzymatic activity of primary human hepatocyte liver chips. In addition, after 24 hours incubation with substrates, an increased expression of CYPs 1A2 is observed (Figure 3.1C), suggesting a degree of CYP induction. Absorption studies with Curio Barriers patterned with only hydrogel show no inherent compound absorption by the microfluidic device (Figure S2).

Liver chips show hepatotoxic response to acetaminophen (APAP) suggesting adequate CYP metabolism to toxic metabolite NAPQI and fialuridine (FIAU) suggesting adequate modeling of human liver physiology. Increased ALT activity in collected media is observed from both treatments across 7-days of drug treatment. In addition, measured total albumin decreased after treatment with low well to well variability. Chips stained for LipidTox show heavy accumulation of lipids in FIAU-treated wells as measured through confocal microscopy.

3.3.2 Aged Microfluidic Liver Chips as DILI Models

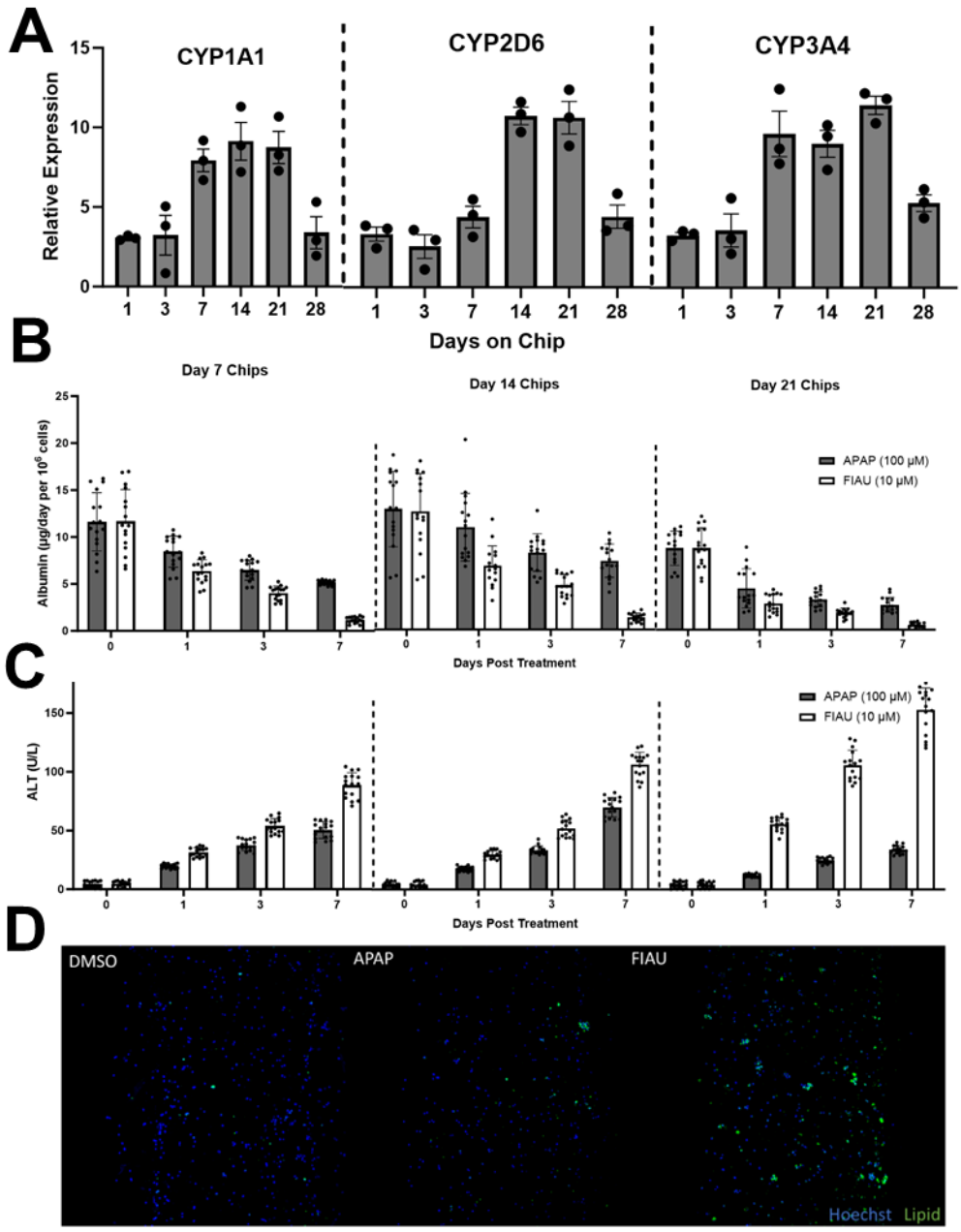

Figure 3.2 Establishing a long-term liver chip for DILI modelling. A) CYP450 levels increase through day 7 and are maintained through day 21. Day 7, 14, and 21 Curio Barrier liver chips are all viable models for assessing APAP and FIAU-induced DILI in both B) albumin and C) ALT responses. D) Fluorescence imaging of Curio Barrier chips show increased lipid accumulation in FIAU treated chip wells.

While our findings in HLO adaptation to Curio Barrier chips matched previous findings in other microfluidic systems, we believe that either space restrictions or lack of hydrogel embedding were limitations in long-term maintenance of liver chips. To this end, Curio Barrier

liver chips were maintained for 28 days. Periodic assaying of output media demonstrated consistent albumin expression through day 21 liver chips with reduced production measured at day 28 liver chips. CYP expression demonstrated somewhat more week to week variability, but significant diminishments were also not identified until day 28. Liver chips fixed and stained for hepatocyte and stellate markers at days 7, 14, and 21 showed identical marker expression in both percent positivity and fluorescent intensity.

As notable and significant loss of function was not observed until day 28 liver chips, liver chips at days 7, 14, and 21 were compared in their utility as DILI models to benchmark their viability across differentially aged liver chips. Liver chips at day 7 show hepatotoxic response to acetaminophen (APAP) suggesting adequate CYP metabolism to toxic metabolite NAPQI and fialuridine (FIAU) suggesting adequate modeling of human liver physiology (Figure 3.2B and C). Increased ALT activity in collected media is observed from both treatments across 7-days of drug treatment. In addition, measured total albumin decreased after treatment with low well to well variability. Interestingly, day 7 and day 14 liver chips demonstrated identical response patterns to APAP and FIAU in both albumin production and ALT release through an additional 7 days culture with drug treatment. Day 14 liver chips used to assess APAP and FIAU-induced DILI also demonstrated similar pattern of staining with emphasis on mitochondrial staining and lipid content. Interestingly, day 21 liver chips showed a unique hepatotoxic response, where significantly higher ALT release was observed following FIAU treatment suggesting worsened cell health at this timepoint. Inversely, APAP-treated liver chips showed minimal ALT release. Chips stained for LipidTox show heavy accumulation of lipids in FIAU-treated wells as measured through confocal microscopy (Figure 3.2D). As we observed a reduction in CYP

expression nearing 28 days of culture, we predicted that this deviation was a result of reduced metabolic turnover of APAP to NAPQI.

3.4 Discussion

Efforts in recent years have demonstrated the superiority of advanced patient-derived models and their potential for standardization in drug discovery, though there are real limitations to accessibility, replicability, and scalability. Liver chips built around the Curio Barrier chip system were designed to mitigate these issues. The iPSC differentiation to HLO protocol was originally designed around existing culture and has recently seen popular adoption in liver research. This is in high contrast to existing PHH methods which are costly and reliant on batch availability. Additionally, PHH-based systems are limited in their physiologically relevance due to the inability to co-culture with non-parenchymal cells from the same patient lineage.

Although the level of complexity associated with multicellular, 3D cultures, and physiological flow has shown to be a hallmark in manufacturing realistic models, historically, these features were not compatible with high-throughput platforms and automated liquid handlers. However, our efforts effectively miniaturize the complex organ-on-chip systems to achieve higher throughput without sacrificing environmental parameters representing physiological relevance. In effect, this enables Curio Barrier liver chips as utilities in early-stage drug discovery. The availability of real estate also allows for complex, large dose-range or even multidrug combination testing.

Our findings also suggest that miniaturized liver chips are capable for long-term maintenance of iPSC-derived liver cell types. Currently, models for chronic DILI and other chronic liver diseases are limited in the available treatment timeframe. Curio Barrier liver chips showed the ability to maintain viable liver cells for up to 28-days and demonstrate their usability

in low-dose, long-term studies, or liver recovery/regeneration research. Particularly, this long-term model may also be used as a model to study viral hepatitis. Future studies will focus around exploring other possibilities of Curio Barrier liver chips and idiosyncratic DILI by use of patient derived HLOs.

3.5 Methods

3.5.1 Human liver organoid differentiation and chip culture

HLOs were differentiated as previously described. In brief, human iPSC line 72.3 obtained from Cincinnati Children's Hospital Medical Center were differentiated into HLOs based on a previously described protocol. iPSCs were seeded at high density on growth factor reduced Matrigel (Corning, 354230) coated 6-well plates (ThermoScientific, 140675) to achieve 90% confluency after 24-hrs culture. iPSCs were then treated with Activin A (R&D Biosystems, 338-AC) for 3 days and FGF4 (purified in house) for 3 additional days to bud definitive endoderm spheroids.

Spheroids were embedded in 75 µL Matrigel (Corning, 354234) droplets in 6 well plates and treated with retinoic acid for 4 days followed by hepatocyte growth media (Hepatocyte Culture Medium BulletKit (Lonza, CC-3198) supplemented with 10 ng/mL hepatocyte growth factor (PeproTech, 100-39), 20 ng/mL oncostatin M (R&D Systems, 295OM050), and 0.1 µM dexamethasone (Millipore Sigma, D4902)) for 12 days. Following culture, cells were removed from Matrigel embeddings by mechanical dislodging with 10 mL wash media (DMEM/F12 supplemented with 1X pen/strep). In a 15 mL tube, organoids in Matrigel were broken apart by repetitive pipetting and spun down at 300 x g for 3 minutes. Media and empty Matrigel was carefully aspirated before repeating washing with fresh 10 mL of wash media. This procedure was repeated until most Matrigel residue was removed as observed visually, roughly 3-5 washes.

Freed organoids were then dispersed by resuspension in 0.25% Trypsin and transferring to a 6-well plate for 37 ^{o}C incubation. After 10 minutes of incubation, cells were pipetted up and down and returned to incubator for an additional 5 minutes of incubation. Trypsin activity was stopped by the addition of 1 mL FBS, transferred to a fresh 15 mL tube, and spun down at 500 x g for 5 minutes. Trypsin with FBS was then aspirated and cells were resuspended in PBS and passed through a 100 µm filter. Cells in PBS were then counted for downstream applications.

3.5.2 Curio Barrier Patterning and Culture

Dispersed HLOs were resuspended in a collagen:Matrigel mixture at a seeding density of 10,000 cells per 1.4 µL and kept on ice. The collagen component was prepared with 5 mg/mL rat tail collagen (Corning, 354236) in 1X PBS (Gibco, 70011044) and 12 mM NaOH (Millipore Sigma, S2770) and mixed 1:1 with Matrigel (Corning, 354234). 1.4 µL of the hydrogel cell suspension was pipetted into compartment 1 of each Curio Barrier chip well and incubated at 37 ^{o}C for 15 minutes to solidify. An additional volume of empty hydrogel mixture was loaded into compartments 2 and 3 and incubated at 37 ^{o}C for 15 minutes to solidify. 100 µL of complete HGM media was added to the top reservoir while 20 µL was added to the bottom reservoir to create a volume gradient which would allow for gradual flow. Media was collected and changed 1 day after patterning followed by every other day.

For assessing differentiation of definitive endoderm to HLOs, foregut spheroids from day 7 of the differentiation were resuspended in the hydrogel mixture and loaded into compartment 1 of the Curio Barrier chips in lieu of dispersed HLOs. Following solidification and hydrogel addition to compartments 2 and 3, the following differentiation medias were identical to standard HLO differentiation. 100 µL of each media was added to both reservoirs (no flow) until addition

of HGM, where the 100 µL of media was added to the top reservoir and 20 µL in the bottom reservoir to introduce flow.

3.5.3 Human Serum Albumin, ALT, and AST Measurements

HSA from chip media outflow was measured using the Human Serum Albumin DuoSet ELISA Kit (R&D Systems, DY1455). ELISA plates were prepared on 96-well plates based on manufacturer's protocol. 50 µL of media from both reservoirs for each chip well was collected and pooled at respective timepoints. 5 uL of pooled media was diluted 100-fold in PBS. 100 uL of diluted media was transferred and incubated on the prepared ELISA plate. Albumin standards of 1.25 to 160 ng/mL were created to fit into a standard curve. Linear regression was used to fit unknown samples to quantify albumin concentration. Each condition contained n=8 biological replicates.

For measuring ALT and AST, 30 uL of media and PBS were dispensed into respective wells in a 96-well assay plate. 300 uL of room temperature ALT/GPT Reagent (Thermo Scientific, TR71121) or AST/GOT Reagent (Thermo Scientific, TR70121) was then dispensed into all wells in the plate and incubated at 37 ^{o}C for 30 seconds before recording absorbance at 340 nm for 3 minutes. Activity of ALT or AST was determined using the following equation:

$$\text{Abs/min} \times \text{Factor}$$

Where Factor is pre-determined for this assay and is 1746, from the manufacturer's manual. Average activity from blanks was subtracted from all other samples. Plates were read with a BioTek Synergy H1 Microplate Reader.

3.5.4 CYP450 Metabolic Turnover

Acetaminophen, cyclophosphamide, and darunavir were chosen as substrates for CYP 1, 2, and 3 families respectively. Media in Curio Barrier chips were replaced with 100 µL media in each reservoir containing substrates at 10 µM. 50 µL of media from each reservoir, pooled together to achieve 100 µL of total media, was taken after 1 hour and 2 hours of incubation. Reactions were immediately stopped using 100 µL of cold methanol and centrifuged for 5-minutes at 3,000 RPM to collect supernatant.

3.5.5 Image Acquisition

All images were acquired with a Yokogawa CQ1 Benchtop or CV8000 High-Content Screening Systems in a machined Curio Barrier chip holder. Each holder was slotted to hold three Curio Barriers, totaling 48 unique chip wells. Imaging on the CQ1 system was acquired at 20X by obtaining 5 µm Z-stacks across 100 µm and acquiring the resulting maximum intensity projection. CV8000 system enabled water immersion imaging and was acquired at 40X resolution by imaging through 1 µm Z-stacks across 25 µm distances to obtain maximum intensity projections.

Chapter 4 Compound Screening in Multiple Patient-derived Liver Organoids Enables Accurate Hepatotoxicity Prediction

4.1 Summary

Throughput has always limited recently developed advanced liver models for their utility in preclinical safety testing of novel molecular entities. While we have previously reported a high-content screening system built around iPSC-derived human liver organoids (HLOs), and that the morphological profiling approach allows for an added layer of mechanistic information compared to traditional hepatotoxicity assays, we note that screening in a single line only achieves specificity of around 60%. Herein, we describe a process of developing patient specific HLOs from whole blood drawn from patients who have suffered severe DILI as part of the DILI Network (DILIN) prospective study and its subsequent usage in compound screening. We notate that redundant screening across four patient lines enhances the assay specificity to over 98% and highlighting that the remaining compounds that evade this screening may require HLOs to be pretreated with inflammatory cytokines.

4.2 Introduction

Drug-induced liver injury (DILI) is a prominent cause of failure in drug discovery and withdrawals in post-marketed drugs.[64] Recent years have seen the development of countless platforms to better assess hepatotoxicity that are superior to immortalized cell lines or primary human hepatocyte assays,[21,70] but as high-throughput methods have seen widespread adoption many of these models fail to keep up with the rate of discovery. As we approach 100,000 herbal

and dietary supplements marketed in the US with unknown liver toxicity profiles,[65] there is a demand for a robust but high-throughput assay to validate xenobiotic safety.

While countless 2D and 3D high-throughput assays exist for DILI screening,[71] an underlying issue with these assays is the often low sensitivity (high false negatives) even in assays which boast a high specificity (low false positives). It is also well reported that findings in animal models are not comparable to humans.[1] Lastly, it is near impossible to consider the diversity in human genetics that result in deviations in CYP450 metabolism, oxidative stress management, lipid accumulation and more that is involved in DILI pathogenesis. This has historically resulted in hepatotoxic compounds evading preclinical assays and making it into human trials[199] or resulting in DILI in a niche subset of patients not represented in clinical trials.[62]

Recent innovations in the field of iPSC-derived human liver organoids (HLOs) have made it possible to replicate any individual patient's liver physiology for *in vitro* testing.[78,80] Additionally, this platform has already demonstrated as a viable model as a DILI high-conten screen and previous findings suggest the representation of interpatient genetics between HLO lines[108] We seek to further enhance this platform's viability as a preclinical screening platform by deriving multiple HLO lines from DILI patients enrolled in the DILI Network (DILIN) at Michigan Medicine. By doing so, we are concentrating the genetics of patients with high susceptibility to DILI based on medical history and allowing for essentially per-patient screening of existing and novel compounds.

4.3 Results

4.3.1 Derivation of human liver organoids from idiosyncratic DILI patients

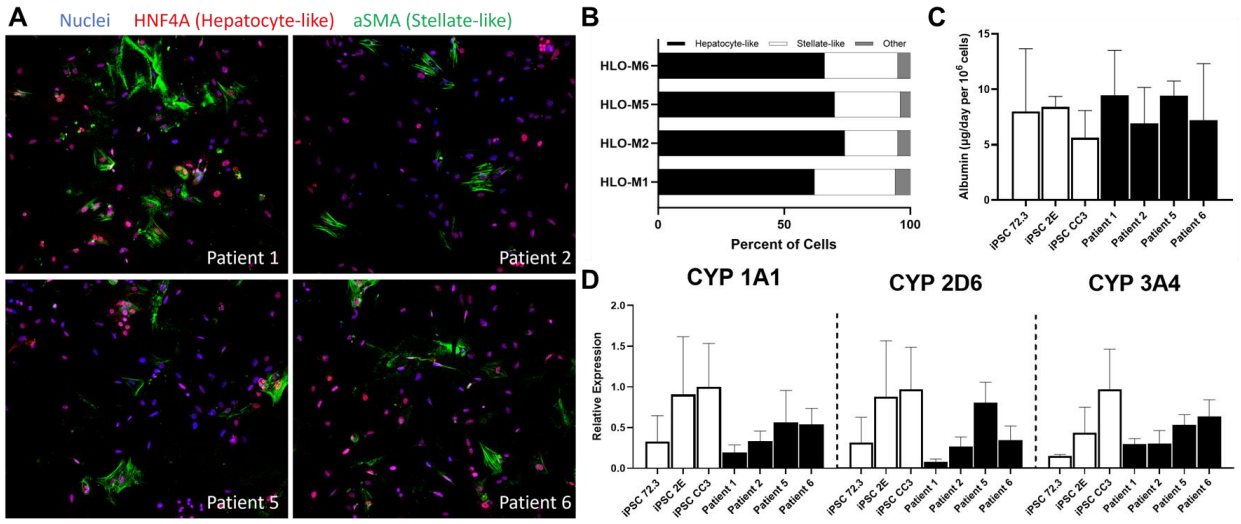

Figure 4.1 HLO's developed from four patients show comparable A) hepatocyte and stellate marker expression, B) ratios of hepatocyte-like and stellate-like cells, C) albumin production, and D) relative expression of CYP450 (n=3 biological replicates).

Whole blood from four patients with DILI due to a single agent and a high causality score enrolled into the DILIN prospective study was collected. All patients provided adequate blood samples with sufficient and quality PBMCs to begin reprograming on date of collection. Erythroid progenitor population expanded from PBMCs were reprogrammed to iPSCs and confirmed positive for pluripotency markers (Sup Figure 1A) and episomal negative (Sup Fig 1B).

iPSCs beginning on passage 8 were differentiated to HLOs and confirmed for hepatocyte marker HNF4A and stellate marker α-SMA expression (Figure 4.1A). Our findings reveal strong consistency between patient-derived HLOs by all measures. First, marker expression shows between 62-74% hepatocyte-like cells and 21-32% stellate-like cells across the four lines (Figure 4.11B). Additionally, no significance was found between any of the DILI patient-derived HLOs in terms of albumin production or CYP450 expression nor between any of the lines and HLOs developed from previously characterized iPSC lines (Figure 1C and D). Cell ratios, albumin, and CYP450 expressions are also consistent previously reported HLOs.[78,108]

4.3.2 Non-biased screening of DILI compounds shows differential patient response

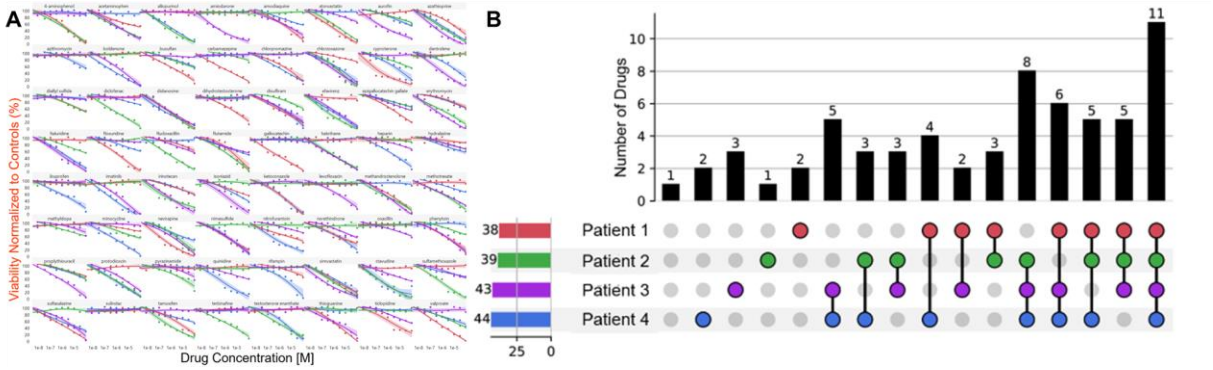

Figure 4.2 A) Results of a 10-point dose response treatment of known hepatotoxins across four patient-derived HLO lines and B) corresponding upset plot analysis demonstrating number of drugs responsive in which subset of patients. (n=4 biological replicates across two independent assays)

All four HLO lines were dispersed into 384-well plates as a single cell suspension and treated with a library of known DILI-causing compounds (Appendix 1A) based on a previously described protocol.[108] Interestingly, each HLO line demonstrated a completely unique response pattern to given drugs with good consistency across two replicate screens. Each individual line responded to 59% to 64% of the compounds matching the sensitivity of many previously developed 2D high-content screens.[101,110,119] However, there is little overlap with the response pattern detected across patients. Only 11 out of the 64 compounds were detected to cause hepatotoxicity across all patients at concentrations up to 100 µM. An additional 24 of these compounds were responsive in a subset of three patient lines and 20 compounds in a subset of two lines. Interestingly, each patient responded showed unique responses to 1-3 of the hepatotoxins suggesting the capture of unique biology not represented in the other cell lines. Sulindac, a compound previously reported to only cause hepatotoxicity with the pretreatment of cytokines,[200] was the only compound to not respond in any patient line.

4.4 Discussion

Our findings demonstrate that redundant drug screening in multiple patient-derived HLO lines is beneficial in accurately detecting DILI across the patient population. With screening in as little as four patient lines, we achieve a 98% sensitivity across our 64 hepatotoxin compound library. However, a minimum of 93% sensitivity can be achieved through selection of any three lines with a sensitivity of around 80% with selection of any two lines. Single line screening would allow for only a maximum of 64% sensitivity and represents why many compounds evade preclinical safety screens.

While we have not achieved 100% sensitivity, the lone undetected compound, sulindac, can be used to generate hypotheses for follow-up studies. As previously demonstrated sulindac is only hepatotoxic with pre-treatment of TNFα, suggesting that an enhancement to this screening platform would involve greater focus on immune-mediated DILI. As it stands, HLOs contain <1% Kupffer cells,[78] the resident macrophage in the liver. Non-liver specific immune cells are not present in this cell population. Therefore, we predict that an added pre-treatment of inflammatory cytokines or co-culturing with a larger immune cell population (which can be obtained through differentiating the same patient's iPSC) may perturb the HLO cell system to result in response to these compounds.

Future studies will focus on profiling each patient-derived HLO line's response to a panel of lone cytokines and cytokines in combination. Clarifying the cytokine mixtures that perturb each HLO will be necessary before redoing the above screens with a cytokine pretreatment. If this pretreatment results in enhanced sensitivity, it will further demonstrate the utility of patient HLO line screening as a high-throughput assessment of hepatotoxicity. As many idiosyncratic

DILIs are thought to be immune-mediated[62], this will also be a step towards elucidating the complex cell interactions occurring in this rare form of DILI.

4.5 Methods

4.5.1 Patient PBMC collection and reprogramming to iPSCs

All selected patients were adults (> 18 yrs) with idiosyncratic DILI from a single drug or HDS product and previously enrolled in the DILIN prospective study at the University of Michigan (clinicaltrials.gov = NCT00345930). Subjects with HIV, HCV, or HBV infection, prior organ or bone marrow transplant, or receiving immunosuppressive drugs were excluded. All subjects provided written informed consent and had 2 x 10 mL tubes of blood drawn for iPSC reprogramming and 1 x 10 mL blood drawn for PBMC preservation. Laboratory investigators remain blinded to the suspect drugs/HDS product.

Reprogramming was done using the Erythroid Progenitor Reprogramming Kit (STEMCELL Technologies, 05924) with assistance from the University of Michigan Human Stem Cell and Gene Editing Core. In brief, erythroid progenitors from PBMCs are expanded and transduced with pluripotency transcription factors. Transduced cells are then cultured on Geltrex coated 6-well dishes until colony formation (~4 weeks). Individual colonies (clones) are then picked into fresh 6-well dishes for expansion and characterization.

4.5.2 384-well plating, treatment, and imaging of dispersed HLOs

384-well plates were prepared with dispersed HLOs as described previously.[108] In brief, HLOs were treated with trypsin to achieve a single cell dispersion which was then seeded in collagen type 1-coated CellCarrier-384 Ultra Microplates (PerkinElmer, 6057308) at a seeding density of 8,000 cells/well in hepatocyte growth media (Hepatocyte Culture Medium BulletKit

(Lonza, CC-3198) supplemented with 10 ng/mL hepatocyte growth factor (PeproTech, 100-39), 20 ng/mL oncostatin M (R&D Systems, 295OM050), and 0.1 μM dexamethasone (Millipore Sigma, D4902)). Cells were incubated to adhere for 48 hrs before media change and treatment with compounds. Compounds were dispensed in 10-point dose-response from a high concentration of 100 μM using an HP D300e Digital Dispenser. Each concentration was dispensed in quadruplicate. Plates were incubated at 37 ^{o}C for 120 hours.

Plates were fixed with 4% paraformaldehyde for 15 minutes followed by permeabilization by 0.1% Triton X-100 (MP Biomedicals, 194854) for 15 minutes (50 μL per well). Cells were blocked by a buffer containing 5% BSA (MilliporeSigma, A9647) and 0.01% Tween (FisherScientific, BP337-100) in PBS for 1 hour (50 μL per well) on an orbital rotator.

Citrate synthase antibody (Cell Signaling, 14309) diluted 1:500 in blocking buffer was then dispensed onto plates and left on an orbital rotator at 4 ^{o}C overnight. Plates were then washed 3X with PBS and treated with a staining mixture containing Hoechst 33342, HCS LipidTox Green (ThermoFisher Scientific, H34475), Donkey anti-Rabbit Alexa Fluor 555 (ThermoFisher Scientific, A31572) and Alexa Fluor 647 Phalloidin (ThermoFisher Scientific, A22287) for 1 hour at room temperature on a rotator protected from light. Plates were washed 3X with PBS before imaging on a Yokogawa CQ1 High-Content Screening Platform at 20X.

Chapter 5 Dissertation Summary and Future Directions

5.1 Summary

Recent discoveries in organoids and the passing of the FDA Modernization Act 2.0 initiated a transitionary phase for drug discovery. While the community adopts various organoids as disease models to identify novel therapies, there is also a demand for robust and accurate models for later stage safety evaluations. As hepatotoxicity is the top contender for drug failures, we are in search of a reliable liver model. While developmental biologists have made strides in new protocols for growing organoids these are not necessarily done with the physical constraints of high-throughput/high-content screening in mind.

Our initial focus was adapting a recent liver organoid[78] to high-content screening. As with many other iPSC-derived organoids, hydrogel embedding, variability in organoid size, and difficulty in taking single-cell morphological measurements is a challenge in screening. In the first section of Chapter 2 we discuss our findings of treating a batch of HLOs with trypsin to suspend in single-cell to seed into 384-well plates. While not without drawbacks (discussed in depth in Limitations), this platform showed feasibility in assaying for hepatotoxicity while preserving the potential of scalability. Additionally, we did not notice deviations in hepatocyte or stellate biology after dispersing cells while high-content imaging showed plausibility in finding similarities between compound hepatotoxicity mechanisms based on resulting perturbations.

Also in Chapter 2, we describe the adaptation of HLOs onto an advanced and highly physiologically relevant organ-on-chip system. This patient-derived organ on chip (PaDLOC)

remarkably enhances liver function of HLOs through increasing albumin secretion and CYP450 activity. PaDLOCs showed strong capability as a DILI model responding to both acetaminophen and fialuridine at physiological concentrations. PaDLOCs were also able to reliably capture a recent case of synergistic DILI across three iPSC-derived HLO lines which had evaded preclinical safety assessment and resulted in a clinical trial failure. In attempt to elucidate the mechanism of action of this synergistic toxicity we obtained single-cell transcriptomics from PaDLOCs and while we were unable to find a concrete mechanism, we were able to generate many hypotheses and hint on another case of synergistic toxicity based on similar transcriptomic patterns.

Due to the low throughput of PaDLOCs, this case of synergistic toxicity was tested and confirmed in the original high-throughput dispersed format. We believe this demonstrates the power of mixing use of these utilities to bounce between generating and confirming hypotheses. In Chapter 3, we attempt to identify a middle ground between these two technologies by culturing HLOs on Curio Barrier chips. Curio Barrier chips seem to retain the physiologically relevant environment provided by Emulate chips in a miniaturized format. Although we were not yet able to characterize a full panel of DILI compounds in this system, we did confirm viability of Curio Barrier liver chips through 28-days of culture. This is a significant finding due to the limited availability of liver models for studying chronic or long-term diseases.

Lastly, as a main advantage of iPSC-derived HLOs is the acquisition of multiple liver cell types from the cell lineage, Chapter 4 was focused on using this feature of HLOs to our advantage. In this study we recruited idiosyncratic DILI patients through DILIN registered at Medicine Medicine to supply a blood draw. PBMCs were obtained from whole blood to reprogram into iPSCs to produce patient-derived HLOs. Interestingly, each patient-derived HLO

lines exhibited a unique response pattern to a panel of hepatotoxic compounds in 10-point dose response assays. As mentioned in the introduction, while previous HCS assays have achieved low false positivity, false negativity is still an issue given a single screening system. Our findings support the need for genetic and cell line diversity in redundant HCS screens to accurately capture the hepatotoxic effects of administered compounds. While this redundancy may be resource intensive it currently exists as one of the sole protocols to consider a wide range of patient genetics *in vitro* and preclinically.

5.2 Limitations

Many limitations in the work described in this dissertation exist. First, we did not adequately describe the maturity and zonation of PaDLOCs. We have not yet determined if the improvements we see with HLOs on chip are a result of becoming less fetal-like or a simple induction of liver marker expression. Due to the long channel of the Emulate chips, we anticipate a detectable oxygen gradient from media inlets and outlets suggesting the possibility of zonation. We also collected a mass set of scRNA sequencing data of PaDLOCs treated with hepatotoxins which was not fully explored. Hopefully this dataset proves useful in other research efforts as it has now been made publicly available.

Our work also presents issues in accessibility to reproduce at other institutions. Although this can be stated as an issue for all iPSC-derived organoids, our purpose in developing DILI models is ultimately to work towards an assay that can be standardized. As it stands iPSC differentiation success is inconsistent across institutions and research groups. Outside of iPSC differentiation, the Emulate chip system is extremely costly and the Curio Barrier chips are not currently available to purchase. Because we consider benefiting the scientific community a high priority, we see this aspect of this research as a severe limitation.

Also, while we collected and developed idiosyncratic DILI patient-derived HLOs we have not yet been able to recreate the idiosyncratic DILI event *in vitro*. At this time, we are unsure if these HLOs contain the complexity necessary in recreating the hepatotoxic event given the original culprit compounds. As idiosyncratic DILI is poorly understood, there is even the possibility that its occurrence is due to other factors such as gut microbiome which would not be represented in this system. However, due to the nature of culturing and passing iPSCs, we have so far been able to bank a collection of samples from patients who suffered from a rare disease which we can continue to study or share.

Lastly, an overall limitation in our work is the lack of clarified checkpoints to determine adequate representation of liver (and by extension other organ models). At this time, it cannot be stated that ours or any other group's models are indeed "truly the desired organ" as there are many underlying determining factors outside of gene and marker expression and certain functional endpoints. While we have confirmed marker expression and production of key liver relevant proteins and enzymes, there is not yet a reliable benchmark in properly validating a liver model and little ability in pitting models against each other. These determining factors should slowly be ironed out while the community works to standardize models in drug discovery but until then it seems as if we are still far away from achieving animal model replacement. With that said, we recently observed the first FDA approved drug that did not see animal testing[201], showing what little this graduate student knows about the world

5.3 Future Studies

Several future studies are already planned to build off the work we've done thus far. Thus far, a library of HDS products implicated in DILI was provided by DILIN. We have obtained crude extracts from these HDS products and screened in HLOs (Appendix B.8-10). Ongoing

research will focus on collecting the full set of features from known single agent natural product hepatotoxins to use as ground truth to identify implicated compounds in the HDS library. Currently, we have assayed a library of organic extracts known hepatotoxic HDS products in qHTS in iPSC 72.3 differentiated HLOs. What can be done next is single agent hepatotoxin identification from extracts by further purification of extracts or by molecular networking. The former can be done by extract fractionation while the latter can be done by assaying a set of known natural product hepatotoxins. Methods used can involve proteomics and mass spectrometry-enabled metabolomics for a multi-omic approach. Due to poor regulation of marketed HDS products, a successful assay may be used to sift through existing HDS products and act as a convenient test for future products.

We will also continue building better DILI models from our patient-derived iPSCs. While HLOs contain most liver cell types, other directed differentiation protocols may prove useful in obtaining endothelial or immune cells from the same genetic lineage. While we do not know the exact interactions necessary to capture idiosyncratic DILI, we will maintain our blinded approach and slowly layer on model complexity (i.e. added macrophages, vascularization, etc.) to treat with a list of possible culprit drugs. Initially, we can better utilize the non-parenchymal chamber on the Emulate chip system. As it exists now, cell dispersions are seeded in both top and bottom channels of the Emulate chips. However, iPSC-derived endothelial cells from the same patient can be seeded in the lower compartment to add vascularity. For patient-derived liver chips, the same patient's PBMCs can also be added to the lower chamber to recreate and mimic liver tissue proximal to a bloodstream. In this instance, the lower chamber can be the sole site of drug administration.

The multi-patient screen sets up several potential projects. Initially, a few compounds have shown interesting differential responses across patients. For example, acetaminophen, a well-studied hepatotoxin, showed response in 3 of the 4 tested HLO lines. While CYP2E1-mediated conversion of acetaminophen is necessary for production of the toxic metabolite NAPQI, and NAPQI toxicity exists only when glutathione is exhausted, this can be an interesting study for why a single patient is unresponsive. Additionally, sulindac, the only compound unresponsive in all 4 patients, was previously shown to only present as hepatotoxic with previous cytokine incubation and inflammatory activity. This means that it may serve as a suitable drug to identify the exact cytokine cocktails necessary to tease out an immune-mediated hepatotoxic response in HLOs.

From a data scientist angle, we will also continuously use our collected data to support future research. We have currently obtained a large dataset of HLO morphological perturbations based on hepatotoxins and patient variations. Machine learning techniques can be used to bridge the gap between well and poorly understood hepatotoxins based on similar presentations of morphology. In effect, the tested compounds can all use extensive literature search to note the exact mechanisms involved in each compound's hepatotoxicity, if available. Mechanism-specific endpoints can then be compared between compounds within the same cluster. Lastly, we will of course be continuously exploring novel liver organoid differentiation protocols and microfluidic devices.

Appendices

Appendix A: Protocols

A.1 iPSC Culture and Maintenance Devised for the Sexton Lab

Introduction:

Herein this protocol describes the step-by-step procedure for thawing, passaging, and maintaining iPSC cultures. The culture itself is straightforward once familiarized but has a few key things of concern. Also, although it seems quite finicky and the possibility of spontaneous differentiation is high, there are tricks to recover a bad culture.

This protocol is largely adapted from instruction by Sha Huang in Jason Spence's lab. Their lab would be the best resource for assistance if any issues or concerns arise during the protocol.

In short, iPSCs grow and are frozen in colonies. This protocol described how to thaw them and wash off freeze down media without disrupting these colonies too much and culturing the iPSCs on Matrigel coated plates, followed by the necessary monitoring of cells for health and removal of spontaneous differentiation.

Thawing iPSCs:

<u>Materials:</u>

Completed MTeSR 1 (StemCell, 85850) or MTeSR Plus (StemCell, 100-0276)

6-well cell culture plates (VWR)

Coating Matrigel: Growth Factor Reduced Basement Membrane Matrix Matrigel (Corning, 354230) diluted to 0.083 mg/mL (effectively, 0.5 mg/6 well plate)

Wash Media: DMEM/F-12 (ThermoFisher Scientific)

ROCK Inhibitor Y-27632 (various sources, but ours is from Cayman)

15 mL Falcon Tube

Procedure:

Day 1:

1. Dispense 1 mL of coating Matrigel into each well of the 6 well plates. Rotate gently to ensure coating of entire well.

2. Plates can be left at room temperature to coat for at least 1 hr or in the incubator for 30 minutes. Coated plates can be Parafilmed and stored in the fridge (do not remove coating media).

3. Warm up 12 mL of wash media DMEM/F12 and 12 mL of mTeSR + Y (2.5 μM) media in incubator.

4. Using your own body temperature, partially thaw the vial of cells by holding it in your hands. Add fully warmed media to the partially thawed tube and gently pipette up and down. Transfer all thawed suspension to a new 15 mL tube. Repeat previous step until cell suspension is fully thawed and transferred to the new 15 mL tube. Add the remainder of the warmed wash media to this tube.

5. Spin down tube at 500 x g for 5 minutes. Aspirate off wash media and resuspend in 12 mL of warmed mTeSR + Y.

6. Remove coating Matrigel from 6-well plates and store in new tube. Coating Matrigel can be used to coat plates twice before disposal.

7. Dispense 2 mL of iPSCs suspended in mTeSR+Y into each well. Label plate with iPSC line name, passage number, and date.

8. Rotate plate left and right, then back and forth, to evenly distribute iPSCs across well.

Day 2:

1. Take a look at iPSC colonies. Most likely, the well will be too sparse to see anything and in that case aspirate off mTeSR+Y and replace with 2 mL of fresh mTeSR (NO Y).

2. If you can notably see many iPSC colonies, proceed with Day 3 procedure.

Day 3:

1. Inspect iPSC colonies. A good, healthy, iPSC colony will be clear, not white, and look like flakes as in the following picture:

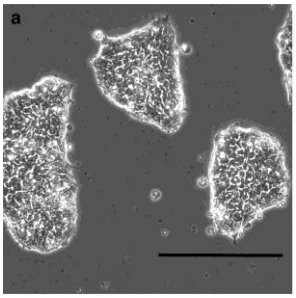

Healthy looking iPSC colonies[202] (figure used with permission)

However, colonies from the first passage after a thaw may look quite different. You may see quite a bit of spontaneous differentiation (any cells that are white and not clear) or the colonies may exhibit a sickle shape. Both are fine to proceed with and should clear up after a few passes, but the more severe it is the more passes it may require before colonies look healthy.

2. If wells are still sparse, put plate back in incubator. No media changes are necessary. If considerable colonies can be observed proceed with steps.

3. Pick off any patches of white with pipette tip. To do so, gently push the Matrigel coating around the patch and it should lift off gently. Ensure that the Matrigel patch is cleanly picked off and no residual Matrigel coating is hanging in suspension but still attached. Going forward, this process will be referred to as cleaning off spontaneous differentiation.

4. After picking, aspirate off media and replace with 2 mL of fresh mTeSR. Place plates back into incubator.

Following Days:

1. Going forward, repeat the process of Day 3 based on colony growth and spontaneous differentiation. Replace media as necessary.

2. Once 70-90% confluency is achieved, or if colonies are notably not growing larger but instead spontaneously differentiating, proceed with passaging.

Passaging iPSCs:

Materials:

Completed MTeSR 1 (StemCell, 85850) or MTeSR Plus (StemCell, 100-0276)

6-well cell culture plates (ThermoFisher Scientific, 140675)

Growth Factor Reduced Basement Membrane Matrix Matrigel (Corning, 354230)

DMEM/F-12 (ThermoFisher Scientific)

Cell scraper

15 mL Falcon Tube

Procedure:

1. Coat 6-well plates as described in first few steps of **Thawing iPSCs**. Each confluent well splits into one 6-well plate for continuing culture, whereas around two confluent wells of iPSCs are passaged into one well of a 6-well plate for differentiation (more explained in HLO differentiation protocol, but basically we need these wells to be at least 90% confluent in one day and not all cells survive the passage or attach). This means for a full confluent 6-well plate, iPSCs are generally passaged into one whole fresh 6-well plate (from one well, in blue in diagram) and into two wells of another plate (from the remaining five wells, in red in diagram).

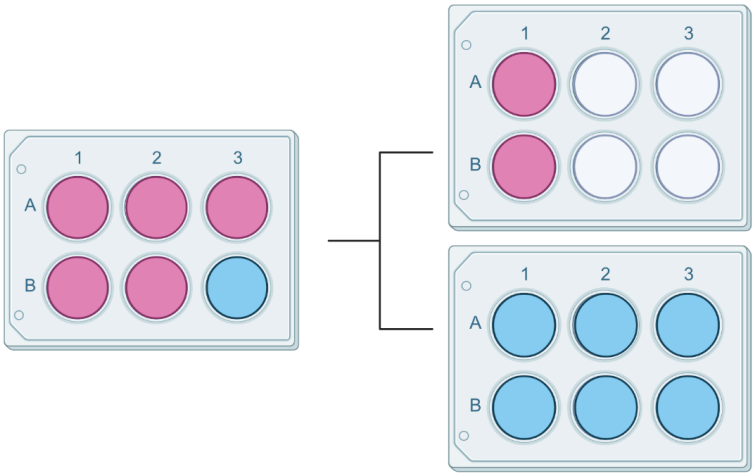

2. Inspect all 6-wells and choose well with healthiest looking colonies. Pick off spontaneous differentiation from all wells.

3. Aspirate off media from all wells. Wash each well 3x with 2 mL of DMEM/F12 wash media each time. Swash media around the wells each was to ensure good cleaning.

4. Add 3.5 mL of fresh mTeSR into best/healthiest looking well. Add 1 mL of fresh mTeSR to all other wells.

5. For each plate, starting with the healthiest well, scrape off Matrigel using cell scraper. Inspect under microscope to ensure little residual Matrigel is left attached.

6. Aspirate off coating Matrigel from fresh plates. For the splitting plate (blue in diagram), add 1 mL of fresh mTeSR into each well. For the differentiation plate (red in diagram) aspirate off coating Matrigel but do not add media.

7. For the well with 3.5 mL mTeSR, pipette up and down exactly two times to slightly break up colonies. One time is generally not enough but three times often breaks up colonies too much. Dispense 0.5 mL of iPSC suspension into each receiving well on splitting plate. This totals to 1.5 mL of media in each well. Label plate with iPSC line name, passage number, and date.

8. For the other wells, pool the contents of the 5 wells and pipette up and down exactly two times. Distribute the ~5 mL of media evenly into two wells on the differentiation plate.

9. Going forward, inspect, maintain, and replace media on the splitting plate as described in Day 3 of **Thawing iPSCs** protocol.

Tips:

1. mTeSR+Y is only used at thawing. Y is not used at any other point in iPSC culture.

2. Every iPSC line grows at different rates, spontaneously differentiates differently, and looks different, which makes managing multiple lines at the same time tricky. It takes some time to know any individual line.

3. For our patient iPSC lines, we have multiple clones of each line. If any line is too tricky you may consider trying another clone.\

4. The “0.5 mL into each well to split” and “2.5 wells into 1 well for differentiation” are a good place to start but will not be standard across lines. It may take a few passages and attempts at differentiation to figure out good parameters.

5. If the wells are still sparse, you may be able to leave the cells unattended for a day. Also, you may double up media (4 mL per well) to leave cells over the weekend. This may result in more spontaneous differentiation to be cleaned but can help with planning. In addition, cells can be split earlier if necessary for scheduling.

A.2 Human Liver Organoid Dispersion to Single Cells

Introduction:

Herein this protocol describes the step-by-step procedure for removing HLOs from their Matrigel embedding, removing as much Matrigel residue as possible, and dispersing the cells into a single

cell resolution. Following dispersal, cells are suitable for seeding in 384-well plates, on chip, or other downstream applications.

Difficulty in this procedure comes from trying to remove as much Matrigel as possible from the cells. There are many methods available with varying degrees of success and this protocol is meant to be the simplest one that retains cell viability even if at the cost of a bit of cell yield. Another popular method uses Cell Recovery solution to dissolve Matrigel but requires cells to be chilled in the fridge for almost an hour. We have tried this and have been successful but with poor cell health.

HLO Dispersion:

Materials:

Matured HLOs embedded in Matrigel, on 6-well plates

Wash Media: DMEM/F12 (Gibco 11320033) supplemented with 1X Pen/Strep (Gibco 15140122)

Trypsin-EDTA (0.25%), phenol red, (Gibco 25200056)

FBS

PBS

Cell Strainer 100 µm (Falcon 352360)

Hepatocyte Growth Media: Hepatocyte Culture Medium BulletKit (Lonza CC-3198), supplemented with 10 ng/mL hepatocyte growth factor (Peprotech 100-39), 20 ng/mL oncostatin M (Peprotech 300-10), and 100 nM dexamethasone (Sigma, D4902).

Trypan Blue solution (Invitrogen, 15250061)

Procedure:

1. Using a P1000 pipet and tip, pipet embedding up and down in well to break up. Transfer contents into a 15 mL tube. If contents $\geq$7 mL, split into two tubes.

2. Add an equal amount of Wash Media into each well as the amount of culture media the cells usually receive. For each well of a 6-well plate, this is usually 2 mL. Pipet Wash Media up and down in each well to ensure capture of all remaining cells/Matrigel and transfer to same 15 mL tube.

3. Using a 10 mL serological, pipet all of tube contents a few more times to once again break up Matrigel and mix contents.

4. Spin tubes at 300 x g for 3 minutes.

5. At this point, you will notice that the cells and Matrigel are pelleted together but should be able to see that pure Matrigel layers higher. At this first step, do NOT aspirate away Matrigel layer. Instead remove only liquid media. We want to break up the Matrigel further with fresh media and try not to lose much cell content.

6. Add 10 mL of fresh Wash Media into tube. Pipet up and down 5-10 times to further break up Matrigel.

7. Spin at 300 x g for 3 minutes. This time, you should see even better layering than before. Carefully aspirate off media and top layer of Matrigel. Do not worry about getting all the Matrigel at this time.

8. Repeat steps 6-7 until you remove majority of the Matrigel. This will take 1-3 repeats.

9. Resuspend organoids in equal amount of 0.25% Trypsin as used to culture them. Meaning, if we are dispersing organoids from 3 wells of a 6-well dish, use 6 mL total of Trypsin. Transfer contents into a fresh 6-well dish.

10. Incubate plates for 10 minutes, pipet each well up and down to manually break up cells. Visually inspect the cells and return them to the incubator for an additional 5 minutes.

11. Transfer cells + Trypsin back into a fresh 15 mL tube. Add 1 mL of FBS into each tube to stop the Trypsin.

12. Spin down cells at 500 x g for 5 minutes. Aspirate Trypsin + FBS and resuspend cells in 10 mL of PBS.

13. Pass cells through a 100 µm filter into a fresh 50 mL tube. Count cells with Trypan blue and a hemacytometer.

14. Spin down cells at 500 x g for 5 minutes. Resuspend in appropriate amount of HGM. Y-27632 can be added at a concentration of 2.5 µM if deemed necessary.

A.3 PBMC and Organoid Co-Culture and Live Cell Imaging

Introduction:

Organoids have been pivotal in the advancement of *in vitro* models in life science research. They have continuously been demonstrated to be superior models of human development and diseases attributable to their three-dimensionality, multicellular buildup, and complex organization. Naturally, there has been emphasis on the use of organoids as models for drug discovery and potentially in lieu of unreliable animal models. However, the difficulty and cost in culturing organoids consistently in high-throughput formats is a hinderance towards their utility in early-stage discovery where large-scale experimentation is preferred.

Additionally, immune cell co-cultures have been in recent focus in attempt to better model immune-related diseases and controlled inflammatory effects. As expected, each step towards complexity or physiological relevance is seemingly a step backwards from adaptation to high-throughput technology. Although new technologies are being developed for

compartmentalized microfluidic culture in high throughput formats, the upfront cost prevents widespread adoption, particularly in academic settings.

Herein, we describe a method to transfer liver pseudo-organoids (PO) cultured on round bottom plates to flat bottom 384-well plates at precisely 1 organoid per well followed by co-culture with PBMCs to observe immune cell migration and interaction with the organoid through live cell imaging. As proof of concept, we demonstrate PBMC activation with inflammatory signals. This method attempts to use budget friendly or open-source tools when possible and should be adaptable to other organoid systems with slight modifications.

Materials:

Biological Materials:

Human liver organoids (differentiated from iPSC 72.3)

PBMCs (purified from whole blood)

Reagents:

Hepatocyte Culture Medium BulletKit (Lonza, 185389)

Hepatocyte growth factor (PeproTech, 100-39)

Oncostatin M (PeproTech, 300-10)

Dexamethasone (Millipore Sigma, D4902)

TNFα

LPS

Trypsin-EDTA (0.25%), phenol red (Gibco, 25200056)

FBS (Corning, 35-010-CV)

PBS, pH 7.4 (Gibco, 10010023)

CellTracker Green CMFDA Dye (Invitorgen, C7025)

CellTracker Red CMPTX Dye (Invitrogen, C34552)

384-well Round Bottom Ultra Low Attachment Spheroid Microplate (Corning, 4516)

384-well PhenoPlate (PerkinElmer, 6057308)

Equipment:

Incubator

Biosafety Cabinet

Centrifuge

37 ^{o}C Water Bath

Opentrons OT-2

OT-2 Tips, 1000 µL (Opentrons, 999-00010)

Yokogawa CellVoyager CQ1 Benchtop High-Content Analysis System

Software:

Opentrons Protocol Designer

Yokogawa CQ1 Acquisition

Yokogawa CellPathfinder

ImageJ 1.53t

CellProfiler 4.2.4

KNIME 4.7.6

Reagent Setup:

Solution	**Components**
Wash Media	DMEM/F12 supplemented1X pen-strep
Hepatocyte Growth Media	Hepatocyte Culture Medium supplemented with all BulletKit components except EGF, 10 ng/mL hepatocyte growth factor, 20 ng/mL oncostatin M, 0.1 µM and dexamethasone

CellTracker Green Stain	
CellTracker Red Stain	

Procedures:

Pseudo-organoid preparation

1. Warm Wash Media and HGM to 37 ^{o}C in water bath.

2. Transfer HLOs from 3 wells of a 6-well plate in Matrigel to a 15 mL Falcon tube. Use an equal volume of Wash Media to wash off any remaining Matrigel in well and transfer to the same tube. Pipet up and down 10 times to break up Matrigel.

3. Centrifuge tubes at 500 x g for 5 minutes. Aspirate off media and top layer Matrigel. Be careful not to aspirate any cell contents.

4. Add 10 mL of Wash Media into tube. Pipet up and down 10 times to resuspend and further beak up Matrigel.

5. Repeat steps 3 and 4 until the majority of Matrigel has been aspirated. Resuspend organoids in 6 mL of 0.25% Trypsin solution. Transfer contents to a 6-well plate.

6. Incubate cells at 37 ^{o}C for 10 minutes. Pipet each well up and down 5 times with a 10 mL serological pipet. Return to incubator for an additional 5 minutes.

7. Transfer all cell contents to a 15 mL Falcon tube. Add 1 mL of FBS to tube to stop trypsin reaction.

8. Centrifuge tubes at 500 x g for 5 minutes. Aspirate media and resuspend in 10 mL of PBS and count cells using desired method.

9. Resuspend cells in 10 mL of CellTracker Red solution. Incubate at 37 ^{o}C for 45 minutes.

10. Centrifuge tubes at 500 x g for 5 minutes. Aspirate media and resuspend in 10 mL of PBS.

11. Repeat step 10 two more times to ensure removal of CellTracker Red solution. After final wash resuspend cells 10 mL of PBS and count using desired method.

12. Centrifuge at 500 x g for 5 minutes. Resuspend cells in Hepatocyte Growth Media at a final concentration of 750 cells/50 μL.

13. Using an Opentrons OT-2, Multidrop, other liquid handler, or multichannel pipet, dispense 50 μL of media into each well of a 384-well ULA round bottom plate.

14. Incubate at 37 ^{o}C for 72-hours to allow pseudo-organoid formation.

Assay setup

1. Dispense 25 μL of HGM into each well in a 384-well Perkin Elmer PhenoPlate. This can be done using any automated liquid handler or manually. It is necessary to have a bed of media in the PhenoPlate prior to transfer so that transferred organoids are centered after transfer.

2. Transfer pseudo-organoids to 384-well plate using Opentrons OT-2 protocol. A sample protocol file has been included. This protocol used a single P1000 head to pipet up 50 μL of media in the exact location of the ULA plate to pick up pseudo-organoid and dispense it over media already in the PhenoPlate. A P1000 is ideal due to bore width. Optimization will be necessary for other organoids.

3. Remove PBMCs from liquid and thaw in 37 ^{o}C water bath. Resuspend in 10 mL of warmed Wash Media.

4. Centrifuge at 900 x g for 5 minutes. Resuspend cells in CellTracker Green solution and incubate for 45 minutes.

5. Centrifuge at 900 x g for 5 minutes. Resuspend cells in 10 mL of warmed Wash Media.

6. Repeat step 5 four times for a total of 5 washes. Washes are necessary to ensure complete removal of CellTracker Green solution. Count cells with preferred method and resuspend PBMCs in HGM or HGM with treatment at a concentration of 5,000 cells/10 μL.

Live Cell Imaging

1. Setup imaging parameters to capture the center of each well at 20X every 15 minutes for 144 steps (total of 36 hr imaging period) for CellTracker Green and CellTracker Red channels. Acquired images should be max intensity projections encompassing the top and bottom of each organoid.

2. Set temperature to 37 ^{o}C, CO_2 to 5%, and add 25 mL of humidity chamber on Yokogawa CQ1 or other high-content imaging system. Ensure that all environmental parameters are achieved before proceeding.

3. Using an automated liquid handler, dispense 10 μL of PBMCs into each well.

4. Immediately, but carefully to not disrupt organoid location, transfer plate into high-content imaging system and begin image acquisition.

Data Analysis

CellProfiler 4.2.0 was used to segment PBMCs and whole organoids for each timepoint. Features measured include size and shape morphology of pseudo-organoids, number of PBMCs visible in field, and number of PBMCs within pseudo-organoid region. These measurements were chosen to capture PBMC mobility, rate of movement, recruitment to pseudo-organoid, and dissociation of pseudo-organoids by PBMCs. Live-cell tracking was done in the Yokogawa CQ1 CellPathfinder software.

Results

Well-to-well pseudo-organoid consistency and image quality

The “pseudo-organoid” (PO) approach was selected as a means to achieve low well-to-well variability in the 384-well format for screening purposes. Round bottom plates were selected as a vessel to reform a batch of dispersed organoid cells as they are already widely available and adopted in screening laboratories while providing the shape necessary for cells to reform adhesions. However, for the purposes of visualizing PBMC mobility, we elected to automate transfer of POs to flat-bottom plates. After transfers, consistency of POs was confirmed by size, where all PO were approximately MICRONS in diameter, and with cell count. Importantly, POs were all successfully transferred to within a 20X field in the center of each well, meaning complex imaging protocols that require a first pass imaging to locate organoids is not necessary.

Approaches to live-cell image analysis

The acquired live cell images capture a multitude of biological phenomenon in terms of PBMC-PO interaction. We believe this assay allows for the selection of analytical complexity based on intended question. For example, in our specific assay we do not observe specific morphological or motility changes of PBMCs at an individual level from our live-cell tracking and elected to remove this captured measurement. However, we found that CellProfiler-enabled PBMC and PO segmentation was effective in capturing the following broad measurements across timepoints: 1) number of PBMCs within the given field, 2) PBMCs directly in contact with PO, 3) size of PO, and 4) fragmentation of PO. Measurements to dye intensity were excluded as they did not provide any direct molecular information and were subject to photobleaching.

Appendix B: Figures and Tables

B.1 Assembled Library of Prominent Hepatotoxins

valproate	disulfiram	terbinafine	flucloxacillin
floxuridine	busulfan	protodioscin	4-aminophenol
stavudine	sulfasalazine	testosterone enanthate	diallyl sulfide
methotrexate	nevirapine	quinidine	amodiaquine
pyrazinamide	amiodarone	epigallocatechin	gallocatechin
diclofenac	carbamazepine	chlorzoxazone	ticlopidine
ibuprofen	azathioprine	norethindrone	oxacillin
isoniazid	erythromycin	efavirenz	ketoconazole
tamoxifen	azithromycin	nitrofurantoin	methyldopa
proplythiouracil	thioguanine	catechin	heparin
didanosine	atorvastatin	epicatechin	minocycline
sulindac	cyproterone	dihydrotestosterone	hydralazine
sulfamethoxazole	chlorpromazine	dantrolene	fialuridine
simvastatin	epigallocatechin gallate	methandrostenolone	acetaminophen
rifampin	irinotecan	levofloxacin	nimesulfide
allopurinol	imatinib	halothane	aurofin
flutamide	phenytoin	boldenone	

Table A.1 Curated selection of clinically prominent DILI compounds

B.2 DESeq2 Differential Expressions Acetaminophen vs Control

hgnc_symbol	p_val	avg_log2FC	avg_log2FC_normed	p_val_adj
RPL41	3.02E-153	-0.991853666	-1.046772434	6.56E-149
RPS21	1.62E-113	-1.098052692	-1.15297146	3.51E-109
RPL37	7.59E-103	-1.078403944	-1.133322712	1.65E-98
RPL37A	5.14E-98	-0.945385201	-1.00030397	1.12E-93
DDX3X	2.54E-97	0.988436731	0.933517962	5.52E-93
RPL38	5.47E-95	-0.958280678	-1.013199446	1.19E-90
DYNC1H1	4.33E-91	0.94235167	0.887432901	9.40E-87
CSDE1	1.44E-90	0.628307654	0.573388885	3.14E-86
HDLBP	5.66E-89	0.791587753	0.736668985	1.23E-84
TTC3	6.04E-88	0.90789005	0.852971282	1.31E-83
CAND1	7.51E-86	0.960083535	0.905164766	1.63E-81

GTF2I	1.39E-85	0.664005841	0.609087072	3.02E-81
TM9SF3	1.94E-85	0.89107853	0.836159761	4.22E-81
ATP5MK	1.85E-84	-1.187769474	-1.242688243	4.03E-80
HNRNPU	6.65E-84	0.838868824	0.783950055	1.44E-79
PHF3	2.87E-82	1.052331371	0.997412603	6.24E-78
NDUFA1	3.76E-81	-1.259866927	-1.314785695	8.16E-77
H1-4	9.83E-80	1.980624313	1.925705545	2.14E-75
RPL39	5.01E-79	-0.999162408	-1.054081177	1.09E-74
EEF2	1.25E-78	0.334851831	0.279933062	2.71E-74
SMARCA5	2.25E-78	0.810811643	0.755892875	4.88E-74
DDX17	2.89E-78	0.820369288	0.76545052	6.28E-74
HUWE1	6.05E-78	0.853864486	0.798945718	1.31E-73
STAT3	1.16E-77	1.111766517	1.056847748	2.53E-73
ZKSCAN1	5.17E-76	1.128033448	1.073114679	1.12E-71
RPL36	8.70E-76	-0.864939376	-0.919858144	1.89E-71
PRRC2C	1.72E-75	0.623568904	0.568650135	3.73E-71
NORAD	8.52E-74	1.130311616	1.075392848	1.85E-69
TMA7	2.17E-73	-0.927520985	-0.982439754	4.70E-69
ATP5F1E	3.64E-73	-1.087463134	-1.142381902	7.91E-69
TOP2B	4.28E-73	0.98564738	0.930728611	9.30E-69
BPTF	5.67E-73	0.790623844	0.735705075	1.23E-68
SLIRP	6.56E-73	-1.176538345	-1.231457114	1.43E-68
PRPF4B	2.43E-72	0.920738858	0.86582009	5.28E-68
RPL35A	1.26E-70	-0.917532589	-0.972451358	2.73E-66
G3BP1	1.54E-70	0.673177257	0.618258489	3.36E-66
GOLGB1	3.41E-70	1.129853454	1.074934685	7.41E-66
HSPA4	7.70E-70	0.727332293	0.672413524	1.67E-65
PCM1	2.25E-69	0.980943556	0.926024787	4.90E-65
RPS27	2.92E-69	-0.988557517	-1.043476286	6.35E-65
G3BP2	4.57E-69	0.687988209	0.633069441	9.92E-65
RPS29	5.56E-69	-0.994013324	-1.048932093	1.21E-64
SEPTIN2	6.17E-69	0.576801531	0.521882762	1.34E-64
SMCHD1	6.51E-69	1.111868846	1.056950078	1.42E-64
GOLGA4	7.79E-69	0.911464031	0.856545263	1.69E-64
COX7C	2.47E-68	-0.931223334	-0.986142102	5.36E-64
ZMYM4	3.26E-68	1.033872329	0.97895356	7.08E-64
SETD2	5.44E-68	1.015541101	0.960622333	1.18E-63
DDX6	1.42E-67	0.99429925	0.939380482	3.10E-63
SYNE2	1.47E-67	1.303526024	1.248607256	3.18E-63
SNHG14	2.12E-67	1.26571605	1.210797282	4.60E-63
IPO7	1.69E-66	0.825892155	0.770973387	3.67E-62
RANBP2	2.32E-66	0.931618017	0.876699249	5.04E-62

Table A.2 DESeq2 Differential Expressions values from Acetaminophen vs Control treated PaDLOCs

B.3 DESeq2 Differential Expressions Fialuridine vs Control

hgnc_symbol	p_val	avg_log2FC	avg_log2FC_normed	p_val_adj
RPS10	0	-1.38638	-1.37488	0
KCNQ1OT1	3.33E-217	2.530913	2.54242	7.23E-213
TTC3	1.02E-215	1.17496	1.186467	2.21E-211
PHACTR2	1.87E-195	1.812474	1.823981	4.06E-191
RPS20	3.72E-176	0.659429	0.670935	8.09E-172
HIF1A	9.69E-137	1.250042	1.261549	2.10E-132
IL6ST	5.22E-136	1.464325	1.475832	1.13E-131
COL6A1	7.41E-132	1.438288	1.449795	1.61E-127
SFRP1	5.28E-131	1.87914	1.890646	1.15E-126
MALAT1	4.82E-128	2.368136	2.379642	1.05E-123
PDGFRA	1.02E-126	1.83246	1.843967	2.22E-122
RPL13A	4.06E-125	0.351067	0.362574	8.83E-121
WSB1	7.21E-121	1.219817	1.231324	1.57E-116
PXDN	2.00E-119	1.222404	1.233911	4.35E-115
SIPA1L2	5.31E-116	1.556814	1.568321	1.15E-111
PEG10	5.96E-116	1.413246	1.424752	1.29E-111
COL6A3	2.15E-115	1.960001	1.971508	4.66E-111
RHOU	4.13E-111	1.419824	1.43133	8.98E-107
NFIA	7.69E-111	1.648299	1.659806	1.67E-106
RPL23	1.38E-110	0.453238	0.464745	2.99E-106
MAF	4.52E-110	1.468022	1.479529	9.82E-106
PLAGL1	4.75E-108	1.520279	1.531786	1.03E-103
HDLBP	5.82E-108	0.752899	0.764405	1.26E-103
PDCD4	6.34E-108	1.313123	1.324629	1.38E-103
SEPTIN2	4.17E-107	0.724804	0.73631	9.06E-103
RUNX1T1	7.08E-107	1.604749	1.616256	1.54E-102
HSPE1	4.14E-103	-1.16918	-1.15768	9.00E-99
TNRC6B	4.39E-103	1.215321	1.226828	9.54E-99
STAT3	5.84E-102	1.147574	1.159081	1.27E-97
RPS11	9.07E-102	0.356607	0.368114	1.97E-97
DDX17	1.38E-101	0.836904	0.848411	2.99E-97
SYNE2	1.76E-101	1.274175	1.285682	3.83E-97
SNHG14	5.56E-101	1.215876	1.227383	1.21E-96
CHD9	4.09E-99	1.143233	1.15474	8.88E-95
METTL7A	7.93E-99	1.520305	1.531812	1.72E-94
GOLGB1	2.02E-98	1.14097	1.152476	4.39E-94
HAS2	1.06E-95	1.791485	1.802992	2.31E-91
TUT4	1.65E-94	1.14313	1.154636	3.58E-90
LBH	5.38E-94	1.47937	1.490877	1.17E-89
ANK3	3.62E-92	1.473108	1.484615	7.86E-88
RPL41	4.21E-90	-0.72084	-0.70933	9.14E-86

GUCY1A1	2.37E-89	1.411127	1.422634	5.14E-85
ADAMTS9	6.16E-89	1.470102	1.481608	1.34E-84
NAP1L1	3.51E-88	0.455358	0.466865	7.63E-84
ABCA1	1.07E-87	1.363231	1.374737	2.32E-83
BPTF	3.16E-86	0.804242	0.815749	6.88E-82
FBN1	2.47E-85	1.343085	1.354591	5.36E-81
PJA2	3.29E-85	1.047424	1.05893	7.14E-81
LRRC75A	5.60E-85	1.581551	1.593058	1.22E-80
HMGA1	2.97E-84	-1.56617	-1.55466	6.45E-80
FLRT2	5.95E-84	1.27064	1.282147	1.29E-79
RPL27A	9.74E-84	0.244023	0.25553	2.12E-79
GTF2I	1.66E-83	0.583207	0.594713	3.61E-79
SMARCA1	2.11E-83	0.894556	0.906062	4.58E-79
CYC1	3.69E-83	-1.21736	-1.20585	8.02E-79
RAN	7.89E-83	-0.93816	-0.92665	1.71E-78
SESN3	8.89E-83	1.250401	1.261908	1.93E-78
PBX1	1.17E-82	1.13118	1.142687	2.54E-78
TEAD1	6.20E-82	1.084571	1.096078	1.35E-77
COL5A1	7.40E-82	1.411464	1.422971	1.61E-77
CLIC1	1.75E-81	-1.26996	-1.25846	3.79E-77
CRISPLD2	3.21E-81	1.349894	1.361401	6.97E-77
MIR100HG	6.46E-81	1.465316	1.476823	1.40E-76
ATRX	7.66E-80	0.820623	0.832129	1.66E-75
ANKRD11	7.72E-79	0.8359	0.847407	1.68E-74
DDR2	7.74E-79	1.412279	1.423786	1.68E-74
ZEB2	1.01E-78	1.441989	1.453496	2.20E-74
S100A10	4.68E-77	-1.23299	-1.22148	1.02E-72
MRC2	7.29E-77	1.458527	1.470034	1.58E-72
APP	7.55E-77	0.699136	0.710643	1.64E-72
MAP4	1.31E-76	0.935302	0.946808	2.86E-72
GALNT1	1.63E-76	0.79572	0.807227	3.55E-72
ASH1L	2.00E-76	1.011283	1.022789	4.35E-72
ZKSCAN1	3.59E-76	0.995695	1.007202	7.80E-72
ITPR2	3.91E-76	1.260647	1.272153	8.49E-72
CHD4	4.25E-76	0.660385	0.671892	9.23E-72
NREP	5.96E-76	0.920027	0.931534	1.29E-71
SEPTIN7	1.10E-75	0.821683	0.83319	2.39E-71
COL4A5	2.82E-75	0.985933	0.99744	6.14E-71
PCM1	2.50E-74	0.895663	0.90717	5.44E-70
CAND1	2.86E-74	0.866714	0.878221	6.21E-70
CHD3	4.23E-73	0.985624	0.99713	9.18E-69
AKAP9	5.14E-73	0.819327	0.830834	1.12E-68
MAN1A1	7.29E-73	0.947383	0.95889	1.58E-68

LDHA	1.10E-72	-1.19928	-1.18778	2.40E-68
IGF2	1.47E-72	1.358034	1.369541	3.20E-68
ASCC3	1.90E-72	0.926158	0.937665	4.14E-68
BMPR2	2.19E-72	1.098084	1.109591	4.75E-68
FTX	3.59E-72	1.173193	1.184699	7.80E-68
USP34	5.04E-72	0.942524	0.954031	1.09E-67
GPC6	6.19E-72	1.105148	1.116654	1.34E-67
SUCO	7.14E-72	1.059496	1.071003	1.55E-67
PHF3	2.42E-71	0.905053	0.91656	5.27E-67
NORAD	3.65E-71	1.03546	1.046967	7.94E-67
SLC5A3	4.71E-71	1.101026	1.112533	1.02E-66
MDH2	6.73E-71	-1.04147	-1.02996	1.46E-66
PNRC1	7.21E-71	0.943964	0.955471	1.57E-66
GAPDH	1.03E-70	-0.93423	-0.92272	2.24E-66
EGR1	1.44E-70	0.932386	0.943893	3.14E-66
TCF4	2.95E-70	1.144523	1.15603	6.40E-66
PRDX1	3.36E-70	-1.0093	-0.99779	7.30E-66
ATP5MC3	1.96E-69	-0.89494	-0.88344	4.25E-65
PRRC2C	3.46E-69	0.550244	0.561751	7.52E-65
CCDC88A	4.21E-69	0.961897	0.973404	9.15E-65
RNF19A	5.42E-69	1.130918	1.142425	1.18E-64
TLE1	1.78E-68	0.904055	0.915561	3.87E-64
DDX6	2.15E-68	0.919433	0.930939	4.67E-64
ENAH	1.57E-67	0.78588	0.797387	3.41E-63
MACF1	4.37E-67	0.879079	0.890586	9.49E-63
MPST	7.13E-67	-1.04922	-1.03772	1.55E-62
TCAF1	1.07E-66	0.822627	0.834134	2.33E-62
SNHG32	4.99E-66	0.85465	0.866157	1.08E-61
ZMYM4	1.16E-65	0.985771	0.997278	2.52E-61
SEPTIN11	1.29E-65	0.624452	0.635959	2.81E-61
ZNF106	1.87E-65	0.787165	0.798672	4.06E-61
MMP1	2.08E-65	-2.56512	-2.55361	4.52E-61
ZFHX4	2.69E-65	1.162456	1.173963	5.85E-61
CDH11	3.30E-65	1.195822	1.207329	7.18E-61
EIF5A	4.21E-65	-1.02698	-1.01547	9.15E-61

Table A.3 DESeq2 Differential Expressions values from Fialuridine vs Control treated PaDLOCs

B.4 DESeq2 Differential Expressions Tenofovir vs Control

hgnc_symbol	p_val	avg_log2FC	avg_log2FC_normed	p_val_adj
KCNQ1OT1	4.06E-154	2.821319	2.77602	8.82E-150
RPS10	3.43E-153	-1.10948	-1.15478	7.46E-149
TTC3	2.57E-139	1.196365	1.151066	5.59E-135
SEPTIN2	2.44E-126	0.884399	0.8391	5.31E-122

DDX3X	8.11E-120	1.083022	1.037724	1.76E-115
GOLGB1	1.32E-112	1.384095	1.338796	2.86E-108
HNRNPU	2.04E-111	0.91237	0.867071	4.44E-107
MAP4	1.46E-104	1.242098	1.196799	3.17E-100
DDX17	6.93E-104	1.000485	0.955186	1.50E-99
HIF1A	9.43E-104	1.382792	1.337493	2.05E-99
SYNE2	1.95E-102	1.485952	1.440653	4.23E-98
GTF2I	6.66E-102	0.747636	0.702337	1.45E-97
RPL41	1.90E-100	-0.78512	-0.83042	4.14E-96
MALAT1	3.23E-100	2.371226	2.325927	7.02E-96
TUT4	4.77E-99	1.252395	1.207096	1.04E-94
STAT3	4.85E-97	1.208053	1.162754	1.05E-92
H1-4	1.27E-96	1.971494	1.926195	2.75E-92
PHACTR2	3.42E-95	1.544283	1.498984	7.42E-91
HDLBP	1.12E-93	0.832322	0.787024	2.44E-89
CAND1	1.03E-91	1.05412	1.008821	2.23E-87
BPTF	1.05E-91	0.940453	0.895154	2.28E-87
SMARCA5	4.12E-90	0.80087	0.755571	8.95E-86
PCM1	4.24E-90	1.05745	1.012151	9.21E-86
ATRX	3.21E-87	0.961968	0.916669	6.97E-83
DDX6	1.10E-86	1.11834	1.073041	2.38E-82
SMARCA1	1.50E-86	1.046629	1.00133	3.25E-82
PRPF4B	3.05E-86	1.011304	0.966005	6.62E-82
WSB1	3.93E-86	1.192247	1.146948	8.53E-82
MACF1	5.15E-86	1.219619	1.17432	1.12E-81
PHF3	1.16E-85	1.001984	0.956685	2.52E-81
EIF4G2	1.41E-85	0.606695	0.561396	3.06E-81
TPR	1.43E-83	0.807974	0.762675	3.10E-79
PJA2	3.33E-83	1.169891	1.124592	7.23E-79
ATXN7L3B	5.76E-83	0.914695	0.869396	1.25E-78
PRRC2C	6.72E-83	0.650385	0.605086	1.46E-78
USP34	3.14E-82	1.074497	1.029198	6.83E-78
FTX	1.51E-81	1.453691	1.408392	3.28E-77
ZMYM4	3.10E-81	1.153843	1.108544	6.74E-77
NFIA	2.78E-80	1.843602	1.798303	6.04E-76
CSDE1	4.72E-80	0.5336	0.488301	1.03E-75
TRIP12	6.18E-80	1.02054	0.975241	1.34E-75
IL6ST	9.38E-80	1.522908	1.477609	2.04E-75
ARHGAP5	2.48E-79	1.033863	0.988564	5.38E-75
DYNC1H1	7.06E-79	0.852497	0.807198	1.53E-74
ANKRD11	1.51E-78	0.92547	0.880171	3.27E-74
SNHG14	2.11E-78	1.235261	1.189962	4.59E-74
APP	2.15E-78	0.968725	0.923426	4.67E-74

ENAH	2.29E-78	0.931085	0.885786	4.98E-74
TM9SF3	2.98E-78	0.801257	0.755958	6.46E-74
TOP2B	6.63E-78	0.928827	0.883528	1.44E-73
CHD9	1.86E-77	1.153907	1.108609	4.05E-73
NKTR	3.83E-76	1.031456	0.986157	8.32E-72
DDX5	1.88E-75	0.571833	0.526534	4.08E-71
NORAD	3.25E-75	1.218746	1.173447	7.05E-71
HNRNPA3	3.41E-75	0.638264	0.592965	7.40E-71
SETD2	3.80E-75	1.072408	1.02711	8.25E-71
NECTIN3-AS1	6.64E-75	1.3363	1.291001	1.44E-70
CAPRIN1	7.65E-75	0.74109	0.695791	1.66E-70
HSP90B1	3.35E-74	0.707414	0.662115	7.27E-70
KMT2A	1.04E-73	0.954822	0.909523	2.26E-69
ASH1L	2.74E-73	1.082987	1.037688	5.96E-69
RPS20	6.63E-73	0.384903	0.339604	1.44E-68
ZFYVE16	7.90E-73	1.068111	1.022812	1.72E-68
CHD4	1.69E-72	0.729712	0.684413	3.67E-68
HUWE1	4.95E-71	0.801154	0.755855	1.08E-66
ZNF638	6.02E-71	0.921685	0.876386	1.31E-66
PDCD4	6.72E-71	1.262482	1.217183	1.46E-66
CYP51A1	3.76E-70	0.853258	0.807959	8.16E-66
SMCHD1	5.52E-70	1.016913	0.971614	1.20E-65
ITPR2	1.37E-69	1.365226	1.319927	2.97E-65
N4BP2L2	2.12E-69	0.989531	0.944232	4.60E-65
PDIA3	5.52E-69	0.548759	0.50346	1.20E-64
YWHAE	2.38E-68	0.363594	0.318295	5.17E-64
TRIP11	2.79E-68	0.97113	0.925831	6.05E-64
JPX	5.39E-68	0.792987	0.747688	1.17E-63
MIA3	1.33E-67	1.084559	1.039261	2.89E-63
CCNL1	1.76E-67	1.08817	1.042871	3.83E-63
CLTC	2.11E-67	0.648486	0.603187	4.57E-63
SF3B1	4.36E-67	0.653495	0.608196	9.48E-63
ARGLU1	4.50E-67	0.777246	0.731947	9.77E-63
TRIM44	4.52E-67	0.94572	0.900421	9.82E-63
TNRC6B	2.25E-66	1.083747	1.038448	4.89E-62
AKAP9	5.88E-66	0.86742	0.822121	1.28E-61
SENP6	1.48E-65	0.85365	0.808351	3.21E-61
NIPBL	2.03E-65	0.876463	0.831164	4.40E-61
SUCO	3.39E-65	1.073555	1.028256	7.36E-61
MAN1A1	3.49E-65	0.979111	0.933812	7.59E-61

Table A.4 DESeq2 Differential Expressions values from Tenofovir vs Control treated PaDLOCs

B.5 DESeq2 Differential Expressions Tenofovir/Inarigivir vs Control

hgnc_symbol	p_val	avg_log2FC	avg_log2FC_normed	p_val_adj
TM9SF3	1.73E-123	1.067298	0.996977	########
H1-4	3.79E-100	2.359144	2.288823	8.24E-96
DDX3X	3.40E-95	1.00767	0.937349	7.38E-91
CSDE1	3.50E-90	0.599635	0.529314	7.61E-86
SMARCA5	1.89E-89	0.821393	0.751072	4.11E-85
HNRNPU	1.12E-86	0.849287	0.778966	2.44E-82
PRRC2C	2.87E-83	0.679771	0.60945	6.23E-79
PHF3	1.16E-82	1.062323	0.992002	2.51E-78
CAPRIN1	5.80E-82	0.793006	0.722685	1.26E-77
PRPF4B	6.12E-80	0.968616	0.898295	1.33E-75
TTC3	1.84E-78	0.835943	0.765622	4.00E-74
PDIA3	2.70E-78	0.720704	0.650383	5.86E-74
PRKDC	6.72E-78	0.756482	0.68616	1.46E-73
HUWE1	1.04E-77	0.844909	0.774588	2.25E-73
GOLGB1	7.68E-77	1.207484	1.137163	1.67E-72
KDM1A	1.18E-76	0.765832	0.695511	2.57E-72
NCL	3.92E-75	0.868066	0.797744	8.52E-71
HSPA4	4.65E-74	0.791436	0.721114	1.01E-69
G3BP1	1.12E-72	0.714169	0.643848	2.44E-68
RANBP2	1.47E-72	0.922926	0.852604	3.20E-68
DYNC1H1	5.14E-72	0.832946	0.762625	1.12E-67
HNRNPA3	1.41E-70	0.630276	0.559955	3.07E-66
UBE3A	3.38E-70	0.833587	0.763265	7.33E-66
LRPPRC	3.26E-69	0.92085	0.850529	7.08E-65
SMARCC1	6.20E-69	0.683259	0.612938	1.35E-64
STAT3	6.80E-69	1.099701	1.02938	1.48E-64
PTPN11	2.05E-68	0.925423	0.855102	4.45E-64
SEPTIN2	7.42E-68	0.632209	0.561888	1.61E-63
TOP2B	2.16E-67	0.886751	0.81643	4.70E-63
CAND1	2.42E-67	0.848275	0.777954	5.25E-63
PAPOLA	3.76E-65	0.608517	0.538196	8.16E-61
SMCHD1	4.31E-65	1.013834	0.943512	9.35E-61

Table A.5 DESeq2 Differential Expressions values from Tenofovir/Inarigivir vs Control treated PaDLOCs

B.6 DESeq2 Differential Expressions Tenofovir/Inarigivir vs Fialuridine

hgnc_symbol	p_val	avg_log2FC	avg_log2FC_normed	p_val_adj
IGFBP3	1.93E-257	-3.23483	-3.3152	4.18E-253
RBP1	1.13E-237	-2.18031	-2.26069	2.45E-233
RPS10	1.73E-228	0.737816	0.657444	3.77E-224
DLK1	3.68E-210	-3.38697	-3.46734	7.99E-206

ATP5F1E	2.20E-204	-0.68418	-0.76456	4.79E-200
MFAP4	4.36E-204	-2.36925	-2.44962	9.48E-200
SERPINF1	1.75E-193	-1.8621	-1.94247	3.79E-189
GOLM1	3.67E-190	1.671297	1.590925	7.98E-186
LRRC75A	2.45E-177	-2.18884	-2.26921	5.33E-173
HSPD1	2.94E-173	1.083394	1.003022	6.38E-169
S100A10	4.10E-164	0.992202	0.91183	8.90E-160
HMGA1	1.10E-162	1.34066	1.260288	2.38E-158
CRISPLD2	2.16E-159	-1.87266	-1.95303	4.70E-155
PHACTR2	1.10E-157	-1.31507	-1.39544	2.40E-153
COL6A3	3.25E-157	-2.39173	-2.4721	7.07E-153
RPL37A	4.45E-157	-0.44163	-0.522	9.67E-153
ENO1	4.31E-153	0.979715	0.899343	9.37E-149
METTL7A	1.58E-148	-1.73551	-1.81588	3.44E-144
SERF2	5.21E-148	-0.61036	-0.69073	1.13E-143
OST4	3.82E-147	-0.86751	-0.94788	8.30E-143
HAS2	1.84E-146	-1.95454	-2.03491	3.99E-142
COL6A2	7.05E-143	-1.90846	-1.98883	1.53E-138
COL6A1	4.82E-142	-1.5605	-1.64087	1.05E-137
GABARAP	2.24E-141	-0.82831	-0.90868	4.87E-137
KLF5	1.94E-136	1.488826	1.408454	4.21E-132
PCOLCE	1.32E-131	-1.62322	-1.70359	2.87E-127
PDGFRA	5.30E-130	-1.80843	-1.8888	1.15E-125
MMP1	2.85E-127	2.549116	2.468745	6.19E-123
SPON2	1.76E-126	-1.86319	-1.94356	3.83E-122
MMP2	2.36E-123	-1.63172	-1.7121	5.12E-119
FBLN1	1.89E-122	-1.06498	-1.14535	4.11E-118
CKB	5.18E-122	1.787621	1.70725	1.13E-117
MDK	1.50E-120	-0.97935	-1.05973	3.27E-116
PLD3	3.42E-120	-1.3523	-1.43267	7.43E-116
NEBL	5.53E-120	-1.58023	-1.6606	1.20E-115
MIR100HG	2.07E-119	-1.52017	-1.60055	4.51E-115
C12orf57	3.92E-119	-0.95019	-1.03056	8.51E-115
GPX2	5.47E-119	1.999957	1.919586	1.19E-114
TIMP1	8.48E-119	-1.38054	-1.46091	1.84E-114
SNHG29	7.83E-118	-0.63984	-0.72021	1.70E-113
PLAGL1	1.95E-117	-1.46011	-1.54048	4.23E-113
LBH	2.32E-117	-1.48194	-1.56231	5.03E-113
SFRP1	7.71E-116	-1.89956	-1.97994	1.67E-111
BST2	5.65E-115	-1.76665	-1.84702	1.23E-110
EPCAM	1.06E-114	1.921594	1.841222	2.31E-110
NME4	2.79E-113	-0.96391	-1.04428	6.05E-109
CD24	4.29E-113	0.971866	0.891494	9.33E-109

MRC2	1.31E-112	-1.61505	-1.69543	2.85E-108
LGALS3	1.23E-110	1.648277	1.567905	2.67E-106
MGST1	1.48E-108	1.447807	1.367435	3.23E-104
ODC1	3.94E-108	1.02899	0.948618	8.56E-104
MAGED2	2.16E-107	-1.11058	-1.19096	4.68E-103
IGFBP7	2.88E-105	-1.68584	-1.76621	6.26E-101
MAL2	2.03E-104	1.309773	1.229401	4.40E-100
FGFR4	1.53E-103	1.241217	1.160845	3.33E-99
APRT	2.28E-103	0.729896	0.649524	4.94E-99
TJP2	5.09E-103	1.188828	1.108456	1.10E-98
FGB	1.33E-101	2.232989	2.152617	2.88E-97
TGFBI	1.70E-101	-2.0446	-2.12497	3.70E-97
CLDN7	2.70E-101	1.532783	1.452411	5.86E-97
RAB3B	5.45E-101	1.398395	1.318023	1.18E-96
PTGES3	7.40E-101	0.784832	0.70446	1.61E-96
RHOU	2.96E-100	-1.33179	-1.41217	6.44E-96
NPM1	1.52E-99	0.675504	0.595132	3.31E-95
C1QBP	3.28E-99	0.869249	0.788877	7.12E-95
ASPH	9.95E-99	0.992397	0.912025	2.16E-94
DMKN	4.91E-97	1.052726	0.972354	1.07E-92
FOS	8.90E-97	-1.09782	-1.1782	1.93E-92
PERP	1.49E-96	1.183531	1.103159	3.23E-92
BEX3	1.56E-96	-0.87624	-0.95661	3.40E-92
FBN1	6.18E-96	-1.45238	-1.53275	1.34E-91
FOXA1	6.88E-96	1.417144	1.336773	1.49E-91
GREM2	1.71E-95	-1.30242	-1.38279	3.70E-91
VIL1	1.70E-94	1.251603	1.171231	3.69E-90
QPRT	8.68E-94	-0.85032	-0.93069	1.89E-89
DDR2	9.50E-94	-1.41753	-1.49791	2.06E-89
TCF4	1.34E-93	-1.36341	-1.44379	2.92E-89
EIF5A	2.78E-93	0.739606	0.659235	6.05E-89
VDAC1	2.95E-93	0.724241	0.64387	6.41E-89
NREP	4.63E-93	-1.11578	-1.19615	1.01E-88
FREM1	5.21E-93	-1.38258	-1.46295	1.13E-88
BAMBI	1.25E-92	-1.23286	-1.31324	2.72E-88
CHCHD10	2.31E-92	1.353984	1.273612	5.01E-88
ITGA6	2.86E-92	1.367833	1.287461	6.22E-88
TSC22D1	5.21E-92	-1.04153	-1.1219	1.13E-87
S100A16	1.08E-91	1.294018	1.213647	2.35E-87
TXN	2.00E-91	0.636402	0.556031	4.34E-87
RTL8C	2.38E-91	-1.00008	-1.08045	5.17E-87
FXYD6	5.44E-91	-1.35996	-1.44034	1.18E-86
IGFBP2	1.38E-90	0.956217	0.875845	2.99E-86

COL5A1	1.73E-90	-1.79349	-1.87386	3.75E-86
MAF	2.67E-90	-1.25929	-1.33966	5.80E-86
H1-4	1.31E-89	1.413951	1.33358	2.85E-85
CDX2	3.67E-88	1.453743	1.373371	7.98E-84
AGR2	1.03E-87	2.190186	2.109814	2.25E-83
MMP23B	1.05E-87	-1.43201	-1.51239	2.28E-83
RPS20	1.11E-87	-0.47945	-0.55982	2.41E-83
CDH17	1.65E-87	1.326817	1.246445	3.60E-83
TGFBR3	2.37E-87	-1.29585	-1.37622	5.15E-83
RUNX1T1	2.72E-87	-1.52774	-1.60811	5.92E-83
EGR1	1.05E-86	-1.05256	-1.13293	2.29E-82
ELF3	1.28E-86	1.53445	1.454079	2.77E-82
CDKN1C	2.26E-86	-1.25419	-1.33456	4.91E-82
IGDCC3	2.85E-86	-1.18875	-1.26912	6.20E-82
TPD52	3.29E-86	1.060884	0.980512	7.14E-82
ZEB2	3.39E-86	-1.39951	-1.47989	7.36E-82
TKT	8.39E-86	0.722256	0.641884	1.82E-81
BRI3	9.81E-86	-0.67425	-0.75462	2.13E-81
TSPAN5	1.21E-85	-1.29596	-1.37633	2.62E-81
FLRT2	2.09E-85	-1.3212	-1.40157	4.55E-81
ANXA6	3.08E-85	-1.20853	-1.2889	6.70E-81
COL1A2	4.28E-85	-2.25679	-2.33716	9.31E-81
CDC42EP5	5.09E-85	-1.14246	-1.22284	1.11E-80
COL2A1	1.56E-84	1.484938	1.404566	3.40E-80
PCBD1	2.19E-84	0.769968	0.689597	4.75E-80
ZFP36L2	2.92E-84	0.961199	0.880827	6.34E-80
RAB13	1.81E-83	-0.80997	-0.89034	3.93E-79
PPP1R14B	3.00E-83	0.601747	0.521376	6.51E-79
LAD1	6.45E-83	1.1735	1.093128	1.40E-78
PTN	9.97E-83	-1.48821	-1.56858	2.17E-78
HSP90AB1	1.12E-82	0.620298	0.539926	2.43E-78
STX3	1.29E-82	1.089051	1.008679	2.79E-78
AGPAT2	1.32E-82	1.084807	1.004435	2.86E-78
CD2AP	1.61E-82	0.918748	0.838377	3.51E-78
EID1	3.19E-82	-0.71733	-0.7977	6.93E-78
AP1M2	4.06E-82	0.989762	0.909391	8.81E-78
EDNRA	5.53E-82	-1.14854	-1.22891	1.20E-77
SLIT3	8.02E-82	-1.30526	-1.38563	1.74E-77
LGALS3BP	2.82E-81	-1.06054	-1.14092	6.12E-77
CDH1	3.47E-81	1.348916	1.268544	7.54E-77
ISLR	4.32E-81	-1.11589	-1.19626	9.37E-77
GNAS	6.18E-81	-0.53892	-0.61929	1.34E-76
CDH11	6.63E-81	-1.52886	-1.60923	1.44E-76

ONECUT2	8.44E-81	1.686823	1.606451	1.83E-76
TRIM71	1.97E-80	1.164638	1.084266	4.28E-76
EMILIN1	3.38E-80	-1.32014	-1.40051	7.35E-76
ESRP1	1.08E-79	1.137237	1.056865	2.36E-75
PRDX1	1.38E-79	0.581374	0.501002	3.00E-75
LRPPRC	2.09E-79	0.832372	0.752	4.55E-75
HIF3A	3.17E-79	-1.09603	-1.1764	6.88E-75
MEST	9.25E-79	-1.50417	-1.58454	2.01E-74
ERBB3	1.48E-78	1.234225	1.153854	3.21E-74
IGFBP4	3.26E-78	-1.18206	-1.26243	7.08E-74
PFDN5	3.35E-78	-0.46599	-0.54636	7.27E-74
CCT6A	3.67E-78	0.667449	0.587077	7.98E-74
DANCR	4.71E-78	0.923549	0.843177	1.02E-73
KRT19	4.91E-78	1.128505	1.048133	1.07E-73
COL1A1	6.95E-78	-2.28054	-2.36092	1.51E-73
ADGRA2	9.12E-78	-1.2493	-1.32967	1.98E-73
UGT8	1.09E-77	1.080158	0.999786	2.38E-73
MET	1.19E-77	1.014793	0.934421	2.59E-73
DNM3OS	2.07E-77	-1.15224	-1.23261	4.50E-73
PKM	3.59E-77	0.642796	0.562424	7.79E-73
SHISA2	5.08E-77	-1.12018	-1.20055	1.10E-72
SOX9	9.74E-77	1.408498	1.328126	2.12E-72
RBM47	1.66E-76	0.980522	0.90015	3.61E-72
SCD	2.17E-76	0.736954	0.656582	4.72E-72
PCDH18	2.49E-76	-1.16938	-1.24975	5.41E-72
YBX1	3.13E-76	0.490331	0.40996	6.81E-72
NFIA	4.38E-76	-1.25906	-1.33943	9.52E-72
CEBPD	5.53E-76	-1.17671	-1.25708	1.20E-71
CAMK2N1	8.97E-76	1.074304	0.993932	1.95E-71
RAB25	2.99E-75	1.217101	1.136729	6.51E-71
MRPS6	6.49E-75	-0.73847	-0.81885	1.41E-70
GSPT1	6.97E-75	0.681232	0.60086	1.51E-70
CCT5	8.95E-75	0.733816	0.653444	1.94E-70
MYC	9.18E-75	1.187551	1.107179	1.99E-70
ST14	9.55E-75	1.174601	1.094229	2.08E-70
IFITM3	1.13E-74	-1.02765	-1.10802	2.46E-70
HSPA9	1.44E-74	0.707116	0.626745	3.13E-70
DIAPH1	1.46E-74	0.923038	0.842667	3.17E-70
COMT	4.82E-74	1.435934	1.355562	1.05E-69
HSPB1	6.55E-74	-1.14843	-1.2288	1.42E-69
ATP8B1	9.15E-74	1.044836	0.964464	1.99E-69
CHD3	1.44E-73	-0.99678	-1.07715	3.13E-69
PPA1	2.24E-73	0.658454	0.578082	4.87E-69

H1-5	7.23E-73	1.840642	1.76027	1.57E-68
CLIC1	8.01E-73	0.773472	0.6931	1.74E-68
MAGED1	1.74E-72	-0.82518	-0.90555	3.78E-68
AKAP1	1.82E-72	0.997463	0.917091	3.96E-68
SRPX	2.16E-72	-1.16563	-1.246	4.70E-68
CLDN6	3.68E-72	1.446501	1.366129	8.00E-68
CTNNB1	4.33E-72	-0.76252	-0.84289	9.40E-68
FRZB	6.51E-72	-1.85124	-1.93161	1.42E-67
MAP7	6.93E-72	0.963765	0.883393	1.51E-67
PDCD4	8.48E-72	-0.92274	-1.00311	1.84E-67
CYBA	1.98E-71	1.06819	0.987818	4.31E-67
SNHG32	2.68E-71	-0.87294	-0.95331	5.82E-67
RPS27	4.97E-71	-0.34849	-0.42886	1.08E-66
TOMM40	1.01E-70	0.810929	0.730557	2.19E-66
SERPINA1	1.19E-70	1.838954	1.758583	2.58E-66
TRNP1	2.09E-70	1.090594	1.010222	4.55E-66
GALNT3	2.57E-70	1.093259	1.012887	5.59E-66
HSPE1	5.29E-70	0.587981	0.50761	1.15E-65
REEP6	6.59E-70	1.148039	1.067668	1.43E-65
IGDCC4	1.20E-69	-0.9827	-1.06307	2.60E-65
MFAP2	1.26E-69	-0.90636	-0.98673	2.75E-65
SIPA1L2	2.18E-69	-1.11184	-1.19221	4.74E-65
FAM136A	2.34E-69	0.744631	0.664259	5.09E-65
HSD17B4	3.56E-69	0.815326	0.734955	7.74E-65
HNRNPF	4.20E-69	0.657713	0.577342	9.13E-65
EIF3B	5.47E-69	0.716312	0.63594	1.19E-64
RBMS3	1.03E-68	-1.0913	-1.17167	2.25E-64
SCGN	1.68E-68	1.258642	1.178271	3.65E-64
DACT3	2.07E-68	-1.03778	-1.11815	4.49E-64
ARHGAP18	2.85E-68	1.151966	1.071594	6.19E-64
NR2F1	3.67E-68	-1.17328	-1.25366	7.96E-64
TFRC	3.68E-68	0.851624	0.771252	8.00E-64
RHOBTB3	5.84E-68	-0.84467	-0.92504	1.27E-63
TSPAN13	1.60E-67	0.964825	0.884453	3.47E-63
COL3A1	3.46E-67	-2.19044	-2.27081	7.52E-63
PBX1	3.77E-67	-0.91137	-0.99174	8.19E-63
ZNF503	9.78E-67	-1.05523	-1.1356	2.12E-62
AP1S2	1.05E-66	-0.90716	-0.98754	2.28E-62
PRELID1	1.09E-66	0.557614	0.477243	2.38E-62
TLE1	1.14E-66	-0.89717	-0.97754	2.47E-62
GTF3A	1.94E-66	0.660495	0.580124	4.22E-62
TCEAL9	2.01E-66	-0.88544	-0.96581	4.37E-62
HNRNPH1	3.56E-66	-0.62592	-0.70629	7.73E-62

CFTR	4.29E-66	1.285071	1.2047	9.32E-62
SPINT1	5.79E-66	1.075522	0.99515	1.26E-61
HOOK1	8.43E-66	0.914904	0.834533	1.83E-61
C12orf75	8.51E-66	0.830296	0.749924	1.85E-61
NBEAL2	8.79E-66	0.981677	0.901305	1.91E-61
TSHZ1	1.79E-65	-1.09899	-1.17936	3.88E-61
APOB	2.64E-65	1.572206	1.491835	5.75E-61
XBP1	3.34E-65	0.866008	0.785636	7.26E-61
EZR	4.25E-65	0.962634	0.882262	9.22E-61

Table A.6 DESeq2 Differential Expressions values from Tenofovir/Inarigivir vs Fialuridine treated PaDLOCs

B.7 PaDLOC UMAP and Cluster Gene Expressions

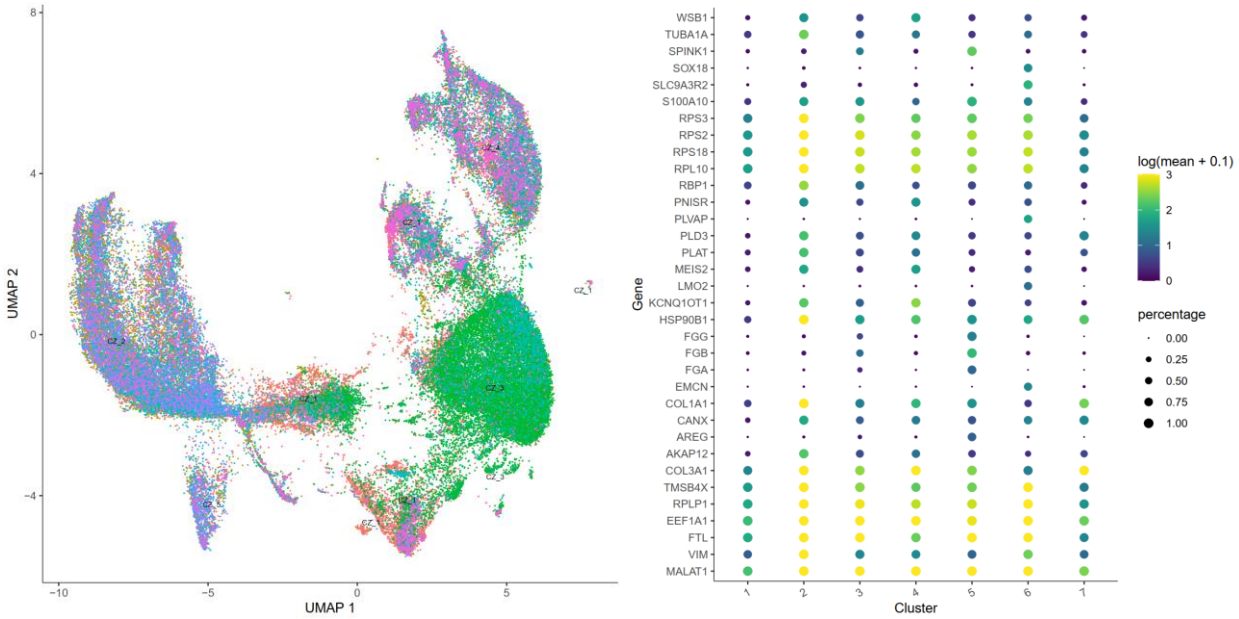

Figure A.1 UMAP embedding of single-cell transcriptomics from all PaDLOCs (left) and expression of genes of interest per cluster (right).

B.8 Screen of HDS Extracts in iPSC 7.23 Differentiated HLOs

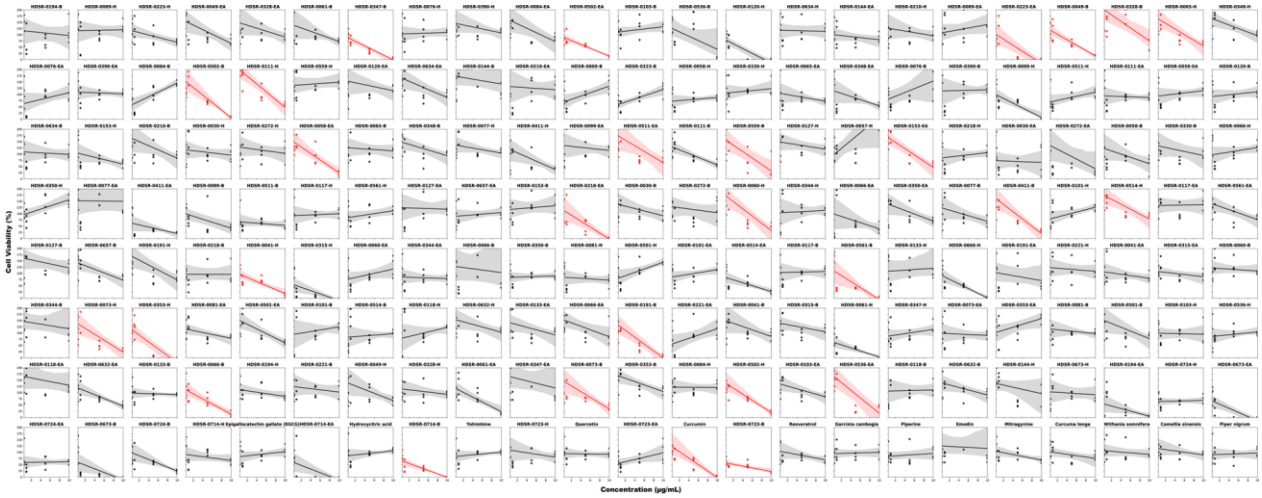

Figure A.2 qHTS results of HDS extract screen in iPSC 72.3 differentiated HLOs

B.9 List of HDS Hits Separated by Organic Solvent Extraction

Hexanes	**Ethyl Acetate**	**N-Butanol**
1. Nuwati Herbal Tea 2. Dual-Action Cleanse, Total Body Purifier 3. DHEA 4. Ortho Multi Greens 5. Nature Plus Ageloss Kidney Support 6. MIT 7. H-Drol 8. Relacore	1. Nuwati Herbal Tea 2. Symphora* 3. Tumeric Powder 4. 6-estro-PCT* 5. White Horn Kratom (Mitragyna Speciosa) 6. It Works Thermofight X* 7. Slimquick 6 ways	1. Nuwati Herbal Tea 2. Dual-Action Cleanse, Total Body Purifier 3. The Right Approach-Teagreen 97 4. Nature's Bounty Black Cohosh 5. Ketone Flawless Raspberry 6. Cellucor Super HD 7. Herbalife Herbal Tea 8. Bali Kratom* 9. HisSynergy 10. Mason Natural Ashwagandha* 11. Urban Ice Organics Red Vein Bali 12. PCT Advanced

Table A.7 HDS products that were identified to be hits in qHTS HLO assay. Asterisks denote extracts that were also hits in a Huh7 counter-screen.

B.10 UMAP Embedding of Morphological Features from HDS Hits

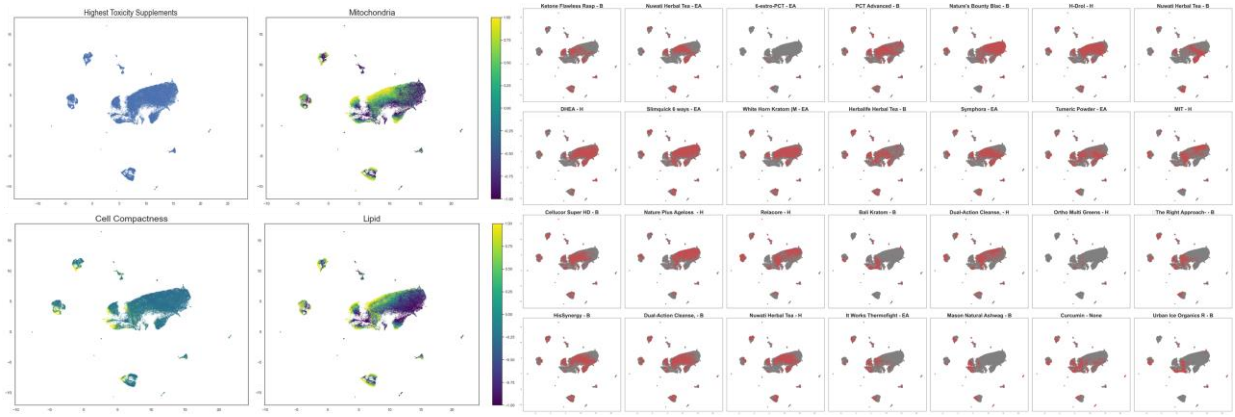

Figure A.3 UMAP embedding of morphological features from top HDS extracts with intensities of select morphological features (left) and with HDS extracts highlighted (right).

Bibliography

1. Sakalem, M. E., De Sibio, M. T., da Costa, F. A. da S. & de Oliveira, M. Historical evolution of spheroids and organoids, and possibilities of use in life sciences and medicine. *Biotechnol. J.* **16**, e2000463 (2021).
2. Syverton, J. T., Scherer, W. F. & Elwood, P. M. Studies on the propagation in vitro of poliomyelitis viruses. V. The application of strain HeLa human epithelial cells for isolation and typing. *J. Lab. Clin. Med.* **43**, 286–302 (1954).
3. Cell Products. *atcc.org* https://www.atcc.org/cell-products.
4. Kapałczyńska, M. *et al.* 2D and 3D cell cultures – a comparison of different types of cancer cell cultures. *Arch. Med. Sci.* (2016) doi:10.5114/aoms.2016.63743.
5. Jensen, C. & Teng, Y. Is it time to start transitioning from 2D to 3D cell culture? *Front. Mol. Biosci.* **7**, 33 (2020).
6. Duval, K. *et al.* Modeling physiological events in 2D vs. 3D cell culture. *Physiology (Bethesda)* **32**, 266–277 (2017).
7. Passaniti, A., Kleinman, H. K. & Martin, G. R. Matrigel: history/background, uses, and future applications. *J. Cell Commun. Signal.* **16**, 621–626 (2022).
8. Coluccio, M. L. *et al.* Microfluidic platforms for cell cultures and investigations. *Microelectron. Eng.* **208**, 14–28 (2019).
9. A guide to the organ-on-a-chip. *Nat. Rev. Methods Primers* **2**, (2022).

10. Huh, D. *et al.* Reconstituting organ-level lung functions on a chip. *Science* **328**, 1662–1668 (2010).
11. Jang, K.-J. *et al.* Reproducing human and cross-species drug toxicities using a Liver-Chip. *Sci. Transl. Med.* **11**, (2019).
12. Kasendra, M. *et al.* Development of a primary human Small Intestine-on-a-Chip using biopsy-derived organoids. *Sci. Rep.* **8**, (2018).
13. van der Flier, L. G. & Clevers, H. Stem cells, self-renewal, and differentiation in the intestinal epithelium. *Annu. Rev. Physiol.* **71**, 241–260 (2009).
14. Spence, J. R. *et al.* Directed differentiation of human pluripotent stem cells into intestinal tissue in vitro. *Nature* **470**, 105–109 (2011).
15. Koike, H. *et al.* Modelling human hepato-biliary-pancreatic organogenesis from the foregut-midgut boundary. *Nature* **574**, 112–116 (2019).
16. Park, S. E., Georgescu, A. & Huh, D. Organoids-on-a-chip. *Science* **364**, 960–965 (2019).
17. Ahmed, S. M., Shivnaraine, R. V. & Wu, J. C. FDA modernization act 2.0 paves the way to computational biology and clinical trials in a dish. *Circulation* **148**, 309–311 (2023).
18. Trefts, E., Gannon, M. & Wasserman, D. H. The liver. *Curr. Biol.* **27**, R1147–R1151 (2017).
19. Cui, J. Y. & Li, C. Y. Regulation of xenobiotic metabolism in the liver. in *Comprehensive Toxicology* 168–214 (Elsevier, 2018).
20. Schulze, R. J., Schott, M. B., Casey, C. A., Tuma, P. L. & McNiven, M. A. The cell biology of the hepatocyte: A membrane trafficking machine. *J. Cell Biol.* **218**, 2096–2112 (2019).
21. Carpentier, N., Urbani, L., Dubruel, P. & Van Vlierberghe, S. The native liver as inspiration to create superior in vitro hepatic models. *Biomater. Sci.* **11**, 1091–1115 (2023).

22. Barnhart, M. I. Prothrombin synthesis: an example of hepatic function. *J. Histochem. Cytochem.* **13**, 740–751 (1965).

23. Redman, C. M. & Xia, H. Fibrinogen biosynthesis. *Ann. N. Y. Acad. Sci.* **936**, 480–495 (2006).

24. Feldmann, G., Penaud-Laurencin, J., Crassous, J. & Benhamou, J. P. Albumin synthesis by human liver cells: its morphological demonstration. *Gastroenterology* **63**, 1036–1048 (1972).

25. Blondet, N. M., Messner, D. J., Kowdley, K. V. & Murray, K. F. Mechanisms of hepatocyte detoxification. in *Physiology of the Gastrointestinal Tract* 981–1001 (Elsevier, 2018).

26. Vaja, R. & Ghuman, N. Drugs and the liver. *Anaesth. Intensive Care Med.* **19**, 30–34 (2018).

27. Pfeifer, N. D., Hardwick, R. N. & Brouwer, K. L. R. Role of hepatic efflux transporters in regulating systemic and hepatocyte exposure to xenobiotics. *Annu. Rev. Pharmacol. Toxicol.* **54**, 509–535 (2014).

28. Tsuchida, T. & Friedman, S. L. Mechanisms of hepatic stellate cell activation. *Nat. Rev. Gastroenterol. Hepatol.* **14**, 397–411 (2017).

29. Ding, C. *et al.* A cell-type-resolved liver proteome. *Mol. Cell. Proteomics* **15**, 3190–3202 (2016).

30. Yin, C., Evason, K. J., Asahina, K. & Stainier, D. Y. R. Hepatic stellate cells in liver development, regeneration, and cancer. *J. Clin. Invest.* **123**, 1902–1910 (2013).

31. Carmona, R., Barrena, S. & Muñoz-Chápuli, R. Retinoids in stellate cells: Development, repair, and regeneration. *J. Dev. Biol.* **7**, 10 (2019).

32. Hellerbrand, C., Stefanovic, B., Giordano, F., Burchardt, E. R. & Brenner, D. A. The role of TGFbeta1 in initiating hepatic stellate cell activation in vivo. *J. Hepatol.* **30**, 77–87 (1999).
33. Pinzani, M. PDGF and signal transduction in hepatic stellate cells. *Front. Biosci.* **7**, d1720-6 (2002).
34. Huang, G. Regulation of hepatic stellate cells by connective tissue growth factor. *Front. Biosci.* **17**, 2495 (2012).
35. Weiskirchen, R. & Tacke, F. Cellular and molecular functions of hepatic stellate cells in inflammatory responses and liver immunology. *Hepatobiliary Surg. Nutr.* **3**, 344–363 (2014).
36. Carter, J. K. & Friedman, S. L. Hepatic stellate cell-immune interactions in NASH. *Front. Endocrinol. (Lausanne)* **13**, 867940 (2022).
37. Zhu, B. *et al.* Activated hepatic stellate cells promote angiogenesis via interleukin-8 in hepatocellular carcinoma. *J. Transl. Med.* **13**, 365 (2015).
38. Zhang, W. *et al.* Heterogeneity of hepatic stellate cells in fibrogenesis of the liver: Insights from single-cell transcriptomic analysis in liver injury. *Cells* **10**, (2021).
39. Wen, Y., Lambrecht, J., Ju, C. & Tacke, F. Hepatic macrophages in liver homeostasis and diseases-diversity, plasticity and therapeutic opportunities. *Cell. Mol. Immunol.* **18**, 45–56 (2021).
40. Dixon, L. J., Barnes, M., Tang, H., Pritchard, M. T. & Nagy, L. E. Kupffer cells in the liver. *Compr. Physiol.* **3**, 785–797 (2013).
41. Tu, Z. *et al.* TLR-dependent cross talk between human Kupffer cells and NK cells. *J. Exp. Med.* **205**, 233–244 (2008).

42. Nguyen-Lefebvre, A. T. & Horuzsko, A. Kupffer cell metabolism and function. *J. Enzymol. Metab.* **1**, (2015).

43. Crispe, I. N. Immune tolerance in liver disease. *Hepatology* **60**, 2109–2117 (2014).

44. Su, L. *et al.* Kupffer cell-derived TNF-α promotes hepatocytes to produce CXCL1 and mobilize neutrophils in response to necrotic cells. *Cell Death Dis.* **9**, (2018).

45. Fabregat, I. & Caballero-Díaz, D. Transforming Growth Factor-β-induced cell plasticity in liver fibrosis and hepatocarcinogenesis. *Front. Oncol.* **8**, 357 (2018).

46. Li, W., Chang, N. & Li, L. Heterogeneity and function of kupffer cells in liver injury. *Front. Immunol.* **13**, 940867 (2022).

47. Palatini, P. & De Martin, S. Pharmacokinetic drug interactions in liver disease: An update. *World J. Gastroenterol.* **22**, 1260–1278 (2016).

48. McDonnell, A. M. & Dang, C. H. Basic review of the cytochrome p450 system. *J. Adv. Pract. Oncol.* **4**, 263–268 (2013).

49. Zhao, M. *et al.* Cytochrome P450 enzymes and drug metabolism in humans. *Int. J. Mol. Sci.* **22**, 12808 (2021).

50. Preissner, S. C. *et al.* Polymorphic cytochrome P450 enzymes (CYPs) and their role in personalized therapy. *PLoS One* **8**, e82562 (2013).

51. Ortiz de Montellano, P. R. Cytochrome P450-activated prodrugs. *Future Med. Chem.* **5**, 213–228 (2013).

52. Jetter, A. & Kullak-Ublick, G. A. Drugs and hepatic transporters: A review. *Pharmacol. Res.* **154**, 104234 (2020).

53. Deodhar, M. *et al.* Mechanisms of CYP450 inhibition: Understanding drug-drug interactions due to mechanism-based inhibition in clinical practice. *Pharmaceutics* **12**, 846 (2020).

54. Izat, N. & Sahin, S. Hepatic transporter-mediated pharmacokinetic drug-drug interactions: Recent studies and regulatory recommendations. *Biopharm. Drug Dispos.* **42**, 45–77 (2021).

55. Loos, N. H. C., Beijnen, J. H. & Schinkel, A. H. The mechanism-based inactivation of CYP3A4 by ritonavir: What mechanism? *Int. J. Mol. Sci.* **23**, 9866 (2022).

56. Chaplin, S. Paxlovid: antiviral combination for the treatment of COVID‐19. *Prescriber* **33**, 31‐33 (2022).

57. Weaver, R. J. *et al.* Managing the challenge of drug-induced liver injury: a roadmap for the development and deployment of preclinical predictive models. *Nat. Rev. Drug Discov.* **19**, 131–148 (2020).

58. David, S. & Hamilton, J. P. Drug-induced liver injury. *US Gastroenterol. Hepatol. Rev.* **6**, 73–80 (2010).

59. Teschke, R. & Danan, G. Drug induced liver injury: Mechanisms, diagnosis, and clinical management. in *Liver Diseases* 95–105 (Springer International Publishing, 2020).

60. Fontana, R. J. *et al.* Idiosyncratic drug-induced liver injury is associated with substantial morbidity and mortality within 6 months from onset. *Gastroenterology* **147**, 96-108.e4 (2014).

61. Andrade, R. J. *et al.* Drug-induced liver injury. *Nat. Rev. Dis. Primers* **5**, 58 (2019).

62. Fontana, R. J. Pathogenesis of idiosyncratic drug-induced liver injury and clinical perspectives. *Gastroenterology* **146**, 914–928 (2014).

63. Gerussi, A. *et al.* Immune-mediated drug-induced liver injury: Immunogenetics and experimental models. *Int. J. Mol. Sci.* **22**, (2021).

64. Watkins, P. B. Drug safety sciences and the bottleneck in drug development. *Clin. Pharmacol. Ther.* **89**, 788–790 (2011).

65. Gindi, R. & National Center for Health Statistics (U.S.). *Health, United States, 2019*. http://dx.doi.org/10.15620/cdc:100685 (2021) doi:10.15620/cdc:100685.

66. Liu, A. *et al.* Prediction and mechanistic analysis of drug-induced liver injury (DILI) based on chemical structure. *Biol. Direct* **16**, 6 (2021).

67. Walker, P. A., Ryder, S., Lavado, A., Dilworth, C. & Riley, R. J. The evolution of strategies to minimise the risk of human drug-induced liver injury (DILI) in drug discovery and development. *Arch. Toxicol.* **94**, 2559–2585 (2020).

68. Tillmann, H. L., Suzuki, A., Barnhart, H. X., Serrano, J. & Rockey, D. C. Tools for causality assessment in drug-induced liver disease. *Curr. Opin. Gastroenterol.* **35**, 183–190 (2019).

69. Daly, A. K. Genetics of drug-induced liver injury: Current knowledge and future prospects. *Clin. Transl. Sci.* **16**, 37–42 (2023).

70. Di Zeo-Sánchez, D. E. *et al.* Modeling drug-induced liver injury: current status and future prospects. *Expert Opin. Drug Metab. Toxicol.* **18**, 555–573 (2022).

71. Kuna, L. *et al.* Models of drug induced Liver Injury (DILI) - current issues and future perspectives. *Curr. Drug Metab.* **19**, 830–838 (2018).

72. Fabre, G., Combalbert, J., Berger, Y. & Cano, J. P. Human hepatocytes as a key in vitro model to improve preclinical drug development. *Eur. J. Drug Metab. Pharmacokinet.* **15**, 165–171 (1990).

73. Stéphenne, X., Najimi, M. & Sokal, E. M. Hepatocyte cryopreservation: is it time to change the strategy? *World J. Gastroenterol.* **16**, 1–14 (2010).

74. Gomez-Lechon, M. J., Donato, M. T., Lahoz, A. & Castell, J. V. Cell Lines: A Tool for In Vitro Drug Metabolism Studies. *Curr. Drug Metab.* **9**, 1–11 (2008).

75. Lauschke, V. M., Shafagh, R. Z., Hendriks, D. F. G. & Ingelman-Sundberg, M. 3D primary hepatocyte culture systems for analyses of liver diseases, drug metabolism, and toxicity: Emerging culture paradigms and applications. *Biotechnol. J.* **14**, e1800347 (2019).

76. Sato, K. *et al.* Organoids and spheroids as models for studying cholestatic liver injury and cholangiocarcinoma. *Hepatology* **74**, 491–502 (2021).

77. Mallanna, S. K. & Duncan, S. A. Differentiation of hepatocytes from pluripotent stem cells. *Curr. Protoc. Stem Cell Biol.* **26**, 1G.4.1-1G.4.13 (2013).

78. Ouchi, R. *et al.* Modeling Steatohepatitis in Humans with Pluripotent Stem Cell-Derived Organoids. *Cell Metab.* **30**, 374-384.e6 (2019).

79. Thompson, W. L. & Takebe, T. Generation of multi-cellular human liver organoids from pluripotent stem cells. *Methods Cell Biol.* **159**, 47–68 (2020).

80. Shinozawa, T. *et al.* High-Fidelity Drug-Induced Liver Injury Screen Using Human Pluripotent Stem Cell–Derived Organoids. *Gastroenterology* **160**, 831-846.e10 (2021).

81. Ewart, L. *et al.* Performance assessment and economic analysis of a human Liver-Chip for predictive toxicology. *Commun. Med. (Lond.)* **2**, 154 (2022).

82. Dalsbecker, P., Beck Adiels, C. & Goksör, M. Liver-on-a-chip devices: the pros and cons of complexity. *Am. J. Physiol. Gastrointest. Liver Physiol.* **323**, G188–G204 (2022).

83. Ewart, L. *et al.* Qualifying a human Liver-Chip for predictive toxicology: Performance assessment and economic implications. *bioRxiv* 2021.12.14.472674 (2021) doi:10.1101/2021.12.14.472674.

84. Picollet-D'hahan, N., Zuchowska, A., Lemeunier, I. & Le Gac, S. Multiorgan-on-a-chip: A systemic approach to model and decipher inter-organ communication. *Trends Biotechnol.* **39**, 788–810 (2021).

85. Shroff, T. *et al.* Studying metabolism with multi-organ chips: new tools for disease modelling, pharmacokinetics and pharmacodynamics. *Open Biol.* **12**, 210333 (2022).

86. Haney, S. A. *High Content Screening: Science, Techniques and Applications*. (John Wiley & Sons, 2008).

87. Yuan, L. & Kaplowitz, N. Mechanisms of drug-induced liver injury. *Clin. Liver Dis.* **17**, 507–18, vii (2013).

88. Lin, S., Schorpp, K., Rothenaigner, I. & Hadian, K. Image-based high-content screening in drug discovery. *Drug Discov. Today* **25**, 1348–1361 (2020).

89. Boussaad, I. *et al.* Integrated, automated maintenance, expansion and differentiation of 2D and 3D patient-derived cellular models for high throughput drug screening. *Sci. Rep.* **11**, 1439 (2021).

90. *Microplate Selection and Recommended Practices in High-throughput Screening and Quantitative Biology*. (Assay Guidance Manual, 2023).

91. *Machine Learning and Assay Development for Image-based Phenotypic Profiling of Drug Treatments*. (Assay Guidance Manual, 2023).

92. Gasparri, F. An overview of cell phenotypes in HCS: limitations and advantages. *Expert Opin. Drug Discov.* **4**, 643–657 (2009).

93. Bray, M.-A. *et al.* Cell Painting, a high-content image-based assay for morphological profiling using multiplexed fluorescent dyes. *Nat. Protoc.* **11**, 1757–1774 (2016).

94. Chandrasekaran, S. N., Ceulemans, H., Boyd, J. D. & Carpenter, A. E. Image-based profiling for drug discovery: due for a machine-learning upgrade? *Nat. Rev. Drug Discov.* **20**, 145–159 (2021).

95. Stirling, D. R., Carpenter, A. E. & Cimini, B. A. CellProfiler Analyst 3.0: Accessible data exploration and machine learning for image analysis. *Bioinformatics* (2021) doi:10.1093/bioinformatics/btab634.

96. Stringer, C. & Pachitariu, M. Cellpose 2.0: how to train your own model. *bioRxiv* 2022.04.01.486764 (2022) doi:10.1101/2022.04.01.486764.

97. Tian, G., Harrison, P. J., Sreenivasan, A. P., Carreras-Puigvert, J. & Spjuth, O. Combining molecular and cell painting image data for mechanism of action prediction. *Artif. Intell. Life Sci.* 100060 (2023).

98. Al-Kofahi, Y., Zaltsman, A., Graves, R., Marshall, W. & Rusu, M. A deep learning-based algorithm for 2-D cell segmentation in microscopy images. *BMC Bioinformatics* **19**, 365 (2018).

99. Marzec, M., Piórkowski, A. & Gertych, A. Efficient automatic 3D segmentation of cell nuclei for high-content screening. *BMC Bioinformatics* **23**, 203 (2022).

100. Emami, N., Sedaei, Z. & Ferdousi, R. Computerized cell tracking: Current methods, tools and challenges. *Vis. Inform.* **5**, 1–13 (2021).

101. O'Brien, P. J. *et al.* High concordance of drug-induced human hepatotoxicity with in vitro cytotoxicity measured in a novel cell-based model using high content screening. *Arch. Toxicol.* **80**, 580–604 (2006).

102. Xu, J. J. *et al.* Cellular imaging predictions of clinical drug-induced liver injury. *Toxicol. Sci.* **105**, 97–105 (2008).

103. Persson, M., Løye, A. F., Mow, T. & Hornberg, J. J. A high content screening assay to predict human drug-induced liver injury during drug discovery. *J. Pharmacol. Toxicol. Methods* **68**, 302–313 (2013).

104. Müller, F. A. *et al.* In vitro to in vivo extrapolation and high-content imaging for simultaneous characterization of chemically induced liver steatosis and markers of hepatotoxicity. *Arch. Toxicol.* **97**, 1701–1721 (2023).

105. Dawson, S., Stahl, S., Paul, N., Barber, J. & Kenna, J. G. In vitro inhibition of the bile salt export pump correlates with risk of cholestatic drug-induced liver injury in humans. *Drug Metab. Dispos.* **40**, 130–138 (2012).

106. Donato, M. T., Tolosa, L., Jiménez, N., Castell, J. V. & Gómez-Lechón, M. J. High-content imaging technology for the evaluation of drug-induced steatosis using a multiparametric cell-based assay. *J. Biomol. Screen.* **17**, 394–400 (2012).

107. Liu, Q. *et al.* In vitro evaluation of the hepatic lipid accumulation of bisphenol analogs: A high-content screening assay. *Toxicol. In Vitro* **68**, 104959 (2020).

108. Zhang, C. J. *et al.* A human liver organoid screening platform for DILI risk prediction. *J. Hepatol.* **78**, 998–1006 (2023).

109. Petronilli, V. *et al.* Transient and long-lasting openings of the mitochondrial permeability transition pore can be monitored directly in intact cells by changes in mitochondrial calcein fluorescence. *Biophys. J.* **76**, 725–734 (1999).

110. Donato, M. & Tolosa, L. High-content screening for the detection of drug-induced oxidative stress in liver cells. *Antioxidants (Basel)* **10**, 106 (2021).

111. Pereira, C. V., Nadanaciva, S., Oliveira, P. J. & Will, Y. The contribution of oxidative stress to drug-induced organ toxicity and its detection in vitro and in vivo. *Expert Opin. Drug Metab. Toxicol.* **8**, 219–237 (2012).

112. Grattagliano, I. *et al.* Biochemical mechanisms in drug-induced liver injury: Certainties and doubts. *World J. Gastroenterol.* **15**, 4865 (2009).

113. Thompson, R. A., Isin, E. M., Ogese, M. O., Mettetal, J. T. & Williams, D. P. Reactive metabolites: Current and emerging risk and hazard assessments. *Chem. Res. Toxicol.* **29**, 505–533 (2016).

114. Giampieri, F. *et al.* Strawberry consumption alleviates doxorubicin-induced toxicity by suppressing oxidative stress. *Food Chem. Toxicol.* **94**, 128–137 (2016).

115. Kang, P. *et al.* Bioactivation of flutamide metabolites by human liver microsomes. *Drug Metab. Dispos.* **36**, 1425–1437 (2008).

116. Teppner, M., Boess, F., Ernst, B. & Pahler, A. Biomarkers of flutamide-bioactivation and oxidative stress in vitro and in vivo. *Drug Metab. Dispos.* **44**, 560–569 (2016).

117. Wink, S., Hiemstra, S. W., Huppelschoten, S., Klip, J. E. & van de Water, B. Dynamic imaging of adaptive stress response pathway activation for prediction of drug induced liver injury. *Arch. Toxicol.* **92**, 1797–1814 (2018).

118. Tolosa, L., Gómez-Lechón, M. J., Pérez-Cataldo, G., Castell, J. V. & Donato, M. T. HepG2 cells simultaneously expressing five P450 enzymes for the screening of hepatotoxicity: identification of bioactivable drugs and the potential mechanism of toxicity involved. *Arch. Toxicol.* **87**, 1115–1127 (2013).

119. Tolosa, L., Carmona, A., Castell, J. V., Gómez-Lechón, M. J. & Donato, M. T. High-content screening of drug-induced mitochondrial impairment in hepatic cells: effects of statins. *Arch. Toxicol.* **89**, 1847–1860 (2015).

120. Lai, Y.-C., Su, S.-Y. & Chang, C.-C. Special reactive oxygen species generation by a highly photostable BODIPY-based photosensitizer for selective photodynamic therapy. *ACS Appl. Mater. Interfaces* **5**, 12935–12943 (2013).

121. Tolosa, L. *et al.* Development of a multiparametric cell-based protocol to screen and classify the hepatotoxicity potential of drugs. *Toxicol. Sci.* **127**, 187–198 (2012).

122. Garside, H. *et al.* Evaluation of the use of imaging parameters for the detection of compound-induced hepatotoxicity in 384-well cultures of HepG2 cells and cryopreserved primary human hepatocytes. *Toxicol. In Vitro* **28**, 171–181 (2014).

123. Saito, J. *et al.* High content analysis assay for prediction of human hepatotoxicity in HepaRG and HepG2 cells. *Toxicol. In Vitro* **33**, 63–70 (2016).

124. Wilson, J. *et al.* Effects of defined mixtures of persistent organic pollutants (POPs) on multiple cellular responses in the human hepatocarcinoma cell line, HepG2, using high content analysis screening. *Toxicol. Appl. Pharmacol.* **294**, 21–31 (2016).

125. Wink, S., Hiemstra, S., Herpers, B. & van de Water, B. High-content imaging-based BAC-GFP toxicity pathway reporters to assess chemical adversity liabilities. *Arch. Toxicol.* **91**, 1367–1383 (2017).

126. Tolosa, L. *et al.* Long-term and mechanistic evaluation of drug-induced liver injury in Upcyte human hepatocytes. *Arch. Toxicol.* **93**, 519–532 (2019).

127. Mennecozzi, M., Landesmann, B., Palosaari, T., Harris, G. & Whelan, M. Sex differences in liver toxicity—do female and male human primary hepatocytes react differently to toxicants in vitro? *PLoS One* **10**, e0122786 (2015).

128. Pradip, A. *et al.* High content analysis of human pluripotent stem cell derived hepatocytes reveals drug induced steatosis and phospholipidosis. *Stem Cells Int.* **2016**, 1–14 (2016).

129. Donato, M. T. & Tolosa, L. Stem-cell derived hepatocyte-like cells for the assessment of drug-induced liver injury. *Differentiation* **106**, 15–22 (2019).

130. Yang, S., Ooka, M., Margolis, R. J. & Xia, M. Liver three-dimensional cellular models for high-throughput chemical testing. *Cell Rep. Methods* **3**, 100432 (2023).

131. Lee, W. M. & Senior, J. R. Recognizing drug-induced liver injury: Current problems, possible solutions. *Toxicol. Pathol.* **33**, 155–164 (2005).

132. Ezhilarasan, D. Hepatic stellate cells in the injured liver: Perspectives beyond hepatic fibrosis. *J. Cell. Physiol.* **237**, 436–449 (2022).

133. Krenkel, O. & Tacke, F. Liver macrophages in tissue homeostasis and disease. *Nat. Rev. Immunol.* **17**, 306–321 (2017).

134. Gracia-Sancho, J., Caparrós, E., Fernández-Iglesias, A. & Francés, R. Role of liver sinusoidal endothelial cells in liver diseases. *Nat. Rev. Gastroenterol. Hepatol.* **18**, 411–431 (2021).

135. Ramaiahgari, S. C. *et al.* A 3D in vitro model of differentiated HepG2 cell spheroids with improved liver-like properties for repeated dose high-throughput toxicity studies. *Arch. Toxicol.* **88**, 1083–1095 (2014).

136. Granitzny, A. *et al.* Evaluation of a human in vitro hepatocyte-NPC co-culture model for the prediction of idiosyncratic drug-induced liver injury: A pilot study. *Toxicol. Rep.* **4**, 89–103 (2017).

137. Padberg, F. *et al.* Novel indirect co-culture of immortalised hepatocytes with monocyte derived macrophages is characterised by pro-inflammatory cytokine networks. *Toxicol. In Vitro* **73**, 105134 (2021).

138. Abu-Absi, S. F., Hansen, L. K. & Hu, W.-S. Three-dimensional co-culture of hepatocytes and stellate cells. *Cytotechnology* **45**, 125–140 (2004).

139. Pingitore, P. *et al.* Human multilineage 3D spheroids as a model of liver steatosis and fibrosis. *Int. J. Mol. Sci.* **20**, 1629 (2019).

140. Liu, J. *et al.* High-content imaging of human hepatic spheroids for researching the mechanism of duloxetine-induced hepatotoxicity. *Cell Death Dis.* **13**, 669 (2022).

141. Hiemstra, S. *et al.* High-throughput confocal imaging of differentiated 3D liver-like spheroid cellular stress response reporters for identification of drug-induced liver injury liability. *Arch. Toxicol.* **93**, 2895–2911 (2019).

142. Fontana, R. J. *et al.* Drug-Induced Liver Injury Network (DILIN) prospective study: rationale, design and conduct. *Drug Saf.* **32**, 55–68 (2009).

143. Fontana, R. J. *et al.* Standardization of nomenclature and causality assessment in drug-induced liver injury: summary of a clinical research workshop. *Hepatology* **52**, 730–742 (2010).

144. Bakke, O. M., Manocchia, M., de Abajo, F., Kaitin, K. I. & Lasagna, L. Drug safety discontinuations in the United Kingdom, the United States, and Spain from 1974 through 1993: a regulatory perspective. *Clin. Pharmacol. Ther.* **58**, 108–117 (1995).

145. Yuen, M.-F. *et al.* Dose response and safety of the daily, oral RIG-I agonist Inarigivir (SB 9200) in treatment naïve patients with chronic hepatitis B: results from the 25mg and 50mg cohorts in the ACHIEVE trial. *Journal of Hepatology* vol. 68 S509–S510 Preprint at https://doi.org/10.1016/s0168-8278(18)31267-4 (2018).

146. Kosh Agarwal, Nezam Afdhal, Carla Coffin, Scott Fung, Geoffrey Dusheiko, Graham Foster, Magdy Elkhashab, Edward Tam, Alnoor Ramji, Radhakrishnan Iyer, Patrick Kennedy. Liver toxicity in the Phase 2 Catalyst 206 trial of inarigivir 400mg daily added to a nucleos(t)ide in HBeAg negative patients. (2020).

147. Yuen, M.-F. *et al.* A phase 2, open‐label, randomized, multiple‐dose study evaluating Inarigivir in treatment‐naïve patients with chronic hepatitis B. *Liver Int.* **43**, 77–89 (2023).

148. Jeffries, R. E. *et al.* Effect of oxygen concentration on viability and metabolism in a fluidized-bed bioartificial liver using ^{31}P and ^{13}C NMR spectroscopy. *Tissue Eng. Part C Methods* **19**, 93–100 (2013).

149. Sheyn, D. *et al.* Bone-chip system to monitor osteogenic differentiation using optical imaging. *Microfluid. Nanofluidics* **23**, (2019).

150. McCracken, K. W. *et al.* Modelling human development and disease in pluripotent stem-cell-derived gastric organoids. *Nature* **516**, 400–404 (2014).

151. Dang, L. T. *et al.* STRADA-mutant human cortical organoids model megalencephaly and exhibit delayed neuronal differentiation. *Dev. Neurobiol.* **81**, 696–709 (2021).

152. Tidball, A. M. *et al.* Genomic Instability Associated with p53 Knockdown in the Generation of Huntington's Disease Human Induced Pluripotent Stem Cells. *PLoS One* **11**, e0150372 (2016).

153. McCracken, K. W., Howell, J. C., Wells, J. M. & Spence, J. R. Generating human intestinal tissue from pluripotent stem cells in vitro. *Nat. Protoc.* **6**, 1920–1928 (2011).

154. Carpenter, A. E. *et al.* CellProfiler: image analysis software for identifying and quantifying cell phenotypes. *Genome Biol.* **7**, R100 (2006).

155. Becht, E. *et al.* Dimensionality reduction for visualizing single-cell data using UMAP. *Nat. Biotechnol.* **37**, 38–44 (2019).

156. McInnes, L., Healy, J. & Astels, S. hdbscan: Hierarchical density based clustering. *J. Open Source Softw.* **2**, 205 (2017).

157. Hoofnagle, J. H., Serrano, J., Knoben, J. E. & Navarro, V. J. LiverTox: a website on drug-induced liver injury. *Hepatology* **57**, 873–874 (2013).

158. Dickson, I. Multispecies liver-on-a-chip for improved drug toxicity testing. *Nature reviews. Gastroenterology & hepatology* vol. 17 4 (2020).

159. Rachfal, A. W. & Brigstock, D. R. Connective tissue growth factor (CTGF/CCN2) in hepatic fibrosis. *Hepatol. Res.* **26**, 1–9 (2003).

160. Goulart, E. *et al.* Adult and iPS-derived non-parenchymal cells regulate liver organoid development through differential modulation of Wnt and TGF-β. *Stem Cell Res. Ther.* **10**, 258 (2019).

161. Rodansky, E. S., Johnson, L. A., Huang, S., Spence, J. R. & Higgins, P. D. R. Intestinal organoids: a model of intestinal fibrosis for evaluating anti-fibrotic drugs. *Exp. Mol. Pathol.* **98**, 346–351 (2015).

162. Ding, Q., Ma, Y., Lai, S., Dou, X. & Li, S. NNMT aggravates hepatic steatosis, but alleviates liver injury in alcoholic liver disease. *J. Hepatol.* **74**, 1248–1250 (2021).

163. Allard, J. B. & Duan, C. IGF-Binding Proteins: Why Do They Exist and Why Are There So Many? Front. *Front. Endocrinol* **9**, (2018).

164. McGill, M. R. The past and present of serum aminotransferases and the future of liver injury biomarkers. *EXCLI journal* vol. 15 Preprint at https://doi.org/10.17179/EXCLI2016-800 (2016).

165. European Association for the Study of the Liver. Electronic address: easloffice@easloffice.eu, Clinical Practice Guideline Panel: Chair:, Panel members, EASL Governing Board representative: EASL Clinical Practice Guidelines: Drug-induced liver injury. *J. Hepatol* **70**, 1222–1261 (2019).

166. James, L. P. *et al.* Pharmacokinetics of acetaminophen-protein adducts in adults with acetaminophen overdose and acute liver failure. *Drug Metab. Dispos.* **37**, 1779–1784 (2009).

167. Dahlin, D. C., Miwa, G. T., Lu, A. Y. & Nelson, S. D. N-acetyl-p-benzoquinone imine: a cytochrome P-450-mediated oxidation product of acetaminophen. *Proc. Natl. Acad. Sci. U. S. A.* **81**, 1327–1331 (1984).

168. Honkoop, P., Scholte, H. R., de Man, R. A. & Schalm, S. W. Mitochondrial Injury Lessons from the Fialuridine Trial. *Drug Safety* vol. 17 1–7 Preprint at https://doi.org/10.2165/00002018-199717010-00001 (1997).

169. Krähenbühl, S. Mitochondria: important target for drug toxicity? *J. Hepatol.* **34**, 334–336 (2001).

170. Hinson, J. A., Roberts, D. W. & James, L. P. Mechanisms of acetaminophen-induced liver necrosis. *Handb. Exp. Pharmacol.* 369–405 (2010).

171. Kleiner, D. E. Drug-induced liver injury: The hepatic pathologist's approach. *Gastroenterol. Clin. North Am.* **46**, 273–296 (2017).

172. Hazra, R. *et al.* Single-dose and steady-state pharmacokinetics of tenofovir disoproxil fumarate in human immunodeficiency virus-infected children. *Antimicrob. Agents Chemother*. **48**, 124–129 (2004).

173. A Fixed-Sequence, Drug-Drug Interaction Study Between Multiple Oral Doses of Inarigivir Soproxil and a Single Oral Dose of Midazolam in Healthy Subjects. https://clinicaltrials.gov/ct2/show/NCT03493698.

174. Pei, J., Sun, X., Yang, G. & Zhang, S. LncRNA KCNQ1OT1 ameliorates the liver injury induced by acetaminophen through the regulation of miR-122-5p/CES2 axis. *Mol. Cell. Biochem.* **475**, 107–118 (2020).

175. Villanueva, C. J. *et al.* Specific role for acyl CoA:Diacylglycerol acyltransferase 1 (Dgat1) in hepatic steatosis due to exogenous fatty acids. *Hepatology* **50**, 434–442 (2009).

176. Griffin, J. D., Salter, D. M., Bowman, T. & Greenberg, A. Role of Hepatic PLIN2 and PLIN4 in The Development of Western Type Diet Induced Hepatosteatosis. *The FASEB Journal* **31**, 458.3-458.3 (2017).

177. Chiyonobu, N. *et al.* Fatty Acid Binding Protein 4 (FABP4) Overexpression in Intratumoral Hepatic Stellate Cells within Hepatocellular Carcinoma with Metabolic Risk Factors. *The American Journal of Pathology* vol. 188 1213–1224 Preprint at https://doi.org/10.1016/j.ajpath.2018.01.012 (2018).

178. Thompson, K. J. *et al.* Altered fatty acid-binding protein 4 (FABP4) expression and function in human and animal models of hepatocellular carcinoma. *Liver Int.* **38**, 1074–1083 (2018).

179. Laouirem, S. *et al.* Endothelial fatty liver binding protein 4: a new targetable mediator in hepatocellular carcinoma related to metabolic syndrome. *Oncogene* **38**, 3033–3046 (2019).

180. Yang, R. *et al.* RNAi-mediated germline knockdown of FABP4 increases body weight but does not improve the deranged nutrient metabolism of diet-induced obese mice. *Int. J. Obes.* **35**, 217–225 (2011).

181. Pessayre, D. *et al.* Central role of mitochondria in drug-induced liver injury. *Drug Metab. Rev.* **44**, 34–87 (2012).

182. Yamada, S. & Guo, X. Peroxiredoxin 4 (PRDX4): Its critical in vivo roles in animal models of metabolic syndrome ranging from atherosclerosis to nonalcoholic fatty liver disease. *Pathology International* vol. 68 91–101 Preprint at https://doi.org/10.1111/pin.12634 (2018).

183. Li, T. *et al.* Glutathione S-transferase P1 correlated with oxidative stress in hepatocellular carcinoma. *Int. J. Med. Sci.* **10**, 683–690 (2013).

184. Kappelhoff, B. S. *et al.* Pharmacokinetics of nevirapine: once-daily versus twice-daily dosing in the 2NN study. *HIV Clin. Trials* **6**, 254–261 (2005).

185. Lee, S. S. T., Buters, J. T. M., Pineau, T., Fernandez-Salguero, P. & Gonzalez, F. J. Role of CYP2E1 in the Hepatotoxicity of Acetaminophen. *Journal of Biological Chemistry* vol. 271 12063–12067 Preprint at https://doi.org/10.1074/jbc.271.20.12063 (1996).

186. Yu, J. *et al.* Induced pluripotent stem cell lines derived from human somatic cells. *Obstet. Gynecol. Surv.* **63**, 154–155 (2008).

187. Sugawara, S. *et al.* Production of an aminoterminally truncated, stable type of bioactive mouse fibroblast growth factor 4 in Escherichia coli. *J. Biosci. Bioeng.* **117**, 525–530 (2014).

188. *Liver-Chip Co-Culture Protocol*. https://emulatebio.com/wp-content/uploads/2021/06/EP008_v5.0_Liver-Chip_Co-Culture_Protocol.pdf (2019).

189. Ianevski, A., Giri, A. K. & Aittokallio, T. SynergyFinder 2.0: visual analytics of multi-drug combination synergies. *Nucleic Acids Res.* **48**, W488–W493 (2020).

190. Frankish, A. *et al.* GENCODE: reference annotation for the human and mouse genomes in 2023. *Nucleic Acids Res.* **51**, D942–D949 (2023).

191. Zheng, G. X. Y. *et al.* Massively parallel digital transcriptional profiling of single cells. *Nat. Commun.* **8**, 14049 (2017).

192. Duncan, A. W. *et al.* The ploidy conveyor of mature hepatocytes as a source of genetic variation. *Nature* **467**, 707–710 (2010).

193. Choudhary, S. & Satija, R. Comparison and evaluation of statistical error models for scRNA-seq. *Genome Biol.* **23**, 27 (2022).

194. Hao, Y. *et al.* Integrated analysis of multimodal single-cell data. *Cell* **184**, 3573-3587.e29 (2021).

195. Love, M. I., Huber, W. & Anders, S. Moderated estimation of fold change and dispersion for RNA-seq data with DESeq2. *bioRxiv* (2014) doi:10.1101/002832.

196. McInnes, L., Healy, J. & Melville, J. UMAP: Uniform Manifold Approximation and Projection for Dimension Reduction. *arXiv [stat.ML]* (2018).

197. Cao, J. *et al.* The single-cell transcriptional landscape of mammalian organogenesis. *Nature* **566**, 496–502 (2019).

198. Melville, J., Lun, A. & Djekidel, M. N. uwot: The uniform manifold approximation and projection (UMAP) method for dimensionality reduction. R Package Version. **15**, (2020).

199. Hey-Hadavi, J. *et al.* Overview of causality assessment for drug-induced liver injury (DILI) in clinical trials. *Drug Saf.* **44**, 619–634 (2021).

200. Zou, W. *et al.* Sulindac metabolism and synergy with tumor necrosis factor-alpha in a drug-inflammation interaction model of idiosyncratic liver injury. *J. Pharmacol. Exp. Ther.* **331**, 114–121 (2009).

201. Enjaymo (sutimlimab-jome) FDA approval history. *Drugs.com* https://www.drugs.com/history/enjaymo.html.

202. Marotta, D., Rao, C. & Fossati, V. Human induced pluripotent stem cell (iPSC) handling protocols: Maintenance, expansion, and cryopreservation. *Methods Mol. Biol.* **2454**, 1–15 (2022).

This dissertation was written or edited in part with the assistance of generative-AI.

Funding:

National Institute of Diabetes and Digestive and Kidney Diseases R01DK120623

University of Michigan Institute for Clinical and Health Research (MICHR) NCATS UL1TR002240

University of Michigan Rackham Graduate School Merit Fellowship (CJZ)

University of Michigan Center of Gastrointestinal Research (UMCGR) Single Cell Pilot Grant 5 P30 DK034933